Mag. rer. nat. Miran MULEC

Magnetohydrodynamic and Kinetic Modelling of Resistive Wall Modes

DOCTORAL THESIS

For obtaining the academic degree of
Doktor der Naturwissenschaften

Doctoral Programme of Natural Sciences
Technical Physics

Graz University of Technology

Supervisor:
Ao. Univ.-Prof. Dipl.-Ing. Dr. phil. Martin F. HEYN

Institute of Theoretical and Computational Physics

Graz, March 2012

Abstract

The ideal kink mode and the resistive wall modes are studied in cylindrical geometry within the magnetohydrodynamic (MHD) plasma model and the kinetic plasma model proposed by Heyn et al [Nucl. Fusion 46 (2006) S159, Phys. Plasmas 18, 022501 (2011)]. The kinetic model accounts for Landau damping, transittime magnetic pumping (TTMP), and Coulomb collisions. Results for the reversed field pinch plasma are compared to the magnetohydrodynamic results obtained by Guo, Freidberg and Nachtrieb [Phys. Plasmas 6 (1999) 3868]. Stabilisation of the external kink mode by an ideal wall as well as stabilisation of the resistive wall mode by toroidal plasma rotation are obtained. In contrast to MHD modelling which predicts a stability window for the resistive wall position, kinetic modelling predicts a one sided window only, i.e. the resistive wall must be sufficiently close to the plasma to achieve rotational stabilisation of the mode but there is no lower limit on the wall position. Stabilising rotation speeds are found somewhat smaller when compared to MHD results. In addition, for the present plasma configuration the kinetic model predicts resistive wall mode stabilisation only in one direction of toroidal rotation. In the opposite direction a destabilising effect is observed. This is in contrast to MHD where mode stabilisation is symmetric with respect to the direction of the toroidal plasma rotation.

Kurzfassung

Ideale Kink Moden und resistive Wand Moden werden mittels eines magnetohydrodynamischen (MHD) Plasma Models sowie eines kinetischen Plasma Models, welches in Heyn et al [Nucl. Fusion 46 (2006) S159, Phys. Plasmas 18, 022501 (2011)] aufgestellt wurde, unter Verwendung von Zylindersymmetrie studiert. Das kinetsche Model berücksichtigt Landau Dämpfung, transittime magnetic pumping (TTMP) sowie Coulomb Stösse. Resultate für die Anwendung in einem reversed field pinch Plasma werden mit magnetohydrodynamischen Ergebnissen von Guo, Freidberg and Nachtrieb [Phys. Plasmas 6 (1999) 3868] verglichen. Erzielt wird die Stabilisierung externer Kink Moden durch eine ideale Wand sowie die Stabilisierung der resistiven Wand Moden durch Plasma Rotation. Im Gegensatz zur MHD Modellierung, welche ein stabiles Fenster für resistive Wandpositionen prognostiziert, wird durch das kinetsche Model lediglich ein einseitiges Fenster vorherbestimmt, d.h. die resistive Wand muss sich genügend nah am Plasma befinden, um eine Stabilisierung durch Rotation zu bewirken; es existiert jedoch kein unteres Limit für die Wandposition. Rotationsgeschwindigkeiten welche zur Stabilisierung notwendig sind, erreichen nur einen Bruchteil im Vergleich zu den MHD Ergebnissen. Zusätzlich prognostiziert das kinetische Model für die vorliegende Plasmakonfugiration eine Stabilisierung der resistiven Wand Moden für nur eine Richtung der toroidalen Rotation. In entgegengesetzter Rotationsrichtung wird ein destabilisierender Effekt beobachtet. Dies steht im Gegensatz zum MHD Model, bei welchem die Rotationsstabilisierung symmetrisch bezüglich der Richtung der toroidalen Plasmarotation ist.

Acknowledgments

I want to thank my supervisor Martin Heyn most sincerely for a huge amount of patience and support during all stages of this work in the last four years and without whom this work would not be possible.
Special thanks also to our group leader Winfried Kernbichler for the large amount of organisation and helpful support at all topics.
Further I want to thank my colleague Ivan Ivanov for a very helpful collaboration and a strong encouragement during all the time.
Special thanks go to Sergei Kasilov for helping discussions and comments and to Helfried Biernat for the evaluation of this thesis.
My gratitude to colleagues Peter Leitner, Bernhard Seiwald, Klaus Allmaier and Georg Leitold for various discussions and support.
This work, supported in part by the European Commission under the contract of Associations between EURATOM and the Austrian Academy of Sciences was carried out within the framework of the European Fusion Development Agreement. The views and opinions expressed herein do not necessarily reflect those of the European Commission. Additional funding is provided by the Austrian Science Foundation, FWF, under contract number P19889-N16, and by the Kommission für die Koordination der Kernfusionsforschung in Österreich, KKKÖ.

Presentations, Posters and Publications in connection with the present work:

Peer reviewed journal articles

- *Kinetic versus ideal magnetohydrodynamic modelling of the resistive wall mode in a reversed field pinch plasma*
  Mulec, M., Ivanov, I.B., Heyn, M.F., Kernbichler, W., Phys. Plasmas **19**, 032502 (2012).

Conference proceedings

- *Quasi-linear modeling of the interaction of resonant magnetic field perturbations with a tokamak plasma*
  Heyn, M.F., Ivanov, I.B., Kasilov, S.V., Kernbichler, W., Mulec, M., 35th EPS Conference on Controlled Fusion and Plasma Physics, Hersonissos, 9 - 13 June 2008, ECA 32D, P-5.009 (2008).

- *Kinetic aspects of resistive wall modes*
  Mulec, M., Ivanov, I.B., Heyn, M.F., Kernbichler, W., 38th Conference on Controlled Fusion and Plasma Physics, Strasbourg, 27 June - 1 July 2011, P2.064 (2011)

Conference posters

- *Plasma response to resonant magnetic field perturbations when modelling Tokamak plasmas*
  Mulec, M., Heyn, M.F., Kasilov, S.V., Culham Plasma Physics Summer School 2008, Oxford, UK and Karlsruhe Summer School on Fusion Technologies 2008, Forschungszentrum Karlsruhe, Germany (2008).

- *MHD Stability Analysis for Tokamaks*
  Mulec, M., Heyn, M.F., Ivanov, I.B., Kasilov, S.V., Third ITER International Summer School 2009, Aix en Provence (2009).

Contents

1 Introduction

After several years of development, magnetically confined plasmas are the best investigated and best understood plasma configurations that are capable for handling fusion processes. The huge amount of technological progress on toroidally closed plasmas like the Tokamak makes this concept hopeful for reaching a commercially interesting test-reactor level.
Experiment Tokamaks like JET, DIII-D or ASDEX, represent magnetically confined plasma configurations which reach the most progressive fusion handling that is achievable at the moment. The next step on the way to reactor scale fusion experiments will be the ITER Tokamak where plasma phenomenons on reactor scale should be studied.
Instability research turned out to be one of the most important topics in modern fusion development. Various processes in fusion plasmas can lead to unstable configurations during fusion operation. Mostly the energy release of these instabilities is high enough to harm the vessel material of the reactor and lower the efficiency of the plasma confinement and lower the output or even stop the fusion process. Due to the different physical nature of the destabilising forces, it was yet not possible to describe an universal model which would be able to handle all instabilities at once and describe them at different plasma limits of temperature, density, magnetic fields and plasma volume. A lot of work has been done describing current and pressure driven instabilities by a fluid model. The *magnetohydrodynamic* (MHD) approach is able to model instabilities under changes of several plasma parameters like vessel dimension, density and temperature changes, plasma rotation (plasma flows) and even resistivity. A second approach is achieved by the *kinetic* descrition of particular particle motion, handling their macroscopic behaviour from the thermodynamical point of view. It is expected that the applicability of either the kinetic or the MHD model should depend on the range of plasma density and temperature and the related particle interactions in the plasma. In recent studies it was demonstrated that MHD theory has strong limitations in its applicability for modern Tokamak parameter range (Refs. [15, 16]). Namely, the radial scale of resonant layers in plasma is comparable to the ion Larmor radius. Therefore it is interesting to check the MHD results for various instabilities connected with resonant magnetic flux surfaces (kink modes, resistive wall modes) using the kinetic approach.
A comprehensive overview on existing modelling and experiments of the stabilisation of the external kink and the resistive wall mode is given in Ref. [6].
It turned out that the commonly used techniques for mode stabilisation are changes of the position of the vessel wall and toroidal plasma rotation. An ideal approximation considers an ideal conducting wall which is moved radially

inward until it reaches the position of mode resonance. If the wall is considered to be resistive, a low frequent mode (resistive wall mode RWM) remains after the resonance position is reached by the wall. These mode cannot be stabilised by wall positioning but by a toroidal plasma velocity.
The used models are based on a numerical solution of the full set of Maxwell equations in cylindrical geometry with the plasma current density taken from either the MHD or the kinetic model. The approximations and derivation steps of the method developed in Refs. [16, 20] are discussed. The application of action-angle variables done by Ref. [23], is used to solve the linearised Vlasov equation analytically and describe how perturbations enter the plasma model. Collisions are modelled by the use of a one-dimensional Fokker-Planck collision operator (Ornstein-Uhlenbeck approximation) with a background distribution function in the form of an inhomogeneous drifting Maxwellian.
In the general case, there are four different regions to be considered with increasing radius: the plasma region followed by a vacuum region followed by the ideal (or resistive) wall region followed by the outer vacuum region. The vacuum as well as the resistive wall region solutions are obtained analytically. Inside the plasma region, Maxwell's equations with the current density obtained from either the fluid model or the kinetic model are solved. The linear system of matching equations is assembled and solved to determine the superposition coefficients for the fundamental solutions in each region. Finite nonzero solutions that correspond to stable or unstable eigenmodes (depending on a sign of imaginary part of the eigenfrequency) are possible only when the determinant of the system is zero.
The results of the present study are to be compared to existing MHD results in particular to the results of the MHD calculations in Ref. [14]. The RFP configuration is based on the $\alpha - \theta_0$ model with a constant density profile. The stability of the resistive wall mode is studied in a (periodic) cylindrical MHD model in which the effects of plasma pressure, compressibility, plasma inertia, longitudinal rotation, and parallel viscosity have been taken into account. The resistive wall is modelled in the above mentioned paper as well as in the present study with finite thickness and constant conductivity.
The thesis is organised as follows. In Sec. 2 the main principles of magnetically confined fusion and experimental research are discussed. A general overview of the Tokamak is given. Sec. 3 shows MHD and kinetic modelling and mentions the numerical approach to solve the system of equations from which the eigenfrequencies of the instabilities result. In Sec. 4 the different regions of the cylinder and particular solutions of Maxwell equations with corresponding boundary conditions at zone interfaces are discussed. Sec. 5 mentions MHD instabilities like kinks and resistive wall modes, their driving mechanisms and

expected behaviour. The reversed field pinch RFP and its plasma equilibrium model are described in Sec. 6. A detailled analysis of instabilities in a RFP equilibrium by MHD and kinetic modelling is given in Sec. 7. A comparison of different eigenmodes for analytically computed Tokamak like profiles by the MHD and the kinetic model is given in Sec. 8.

plasma volume	1 - 100m^3
n_i	$10^{19} - 10^{20}\mathrm{m}^{-3}$
T	$1 - 40$ keV
p	0.1 - 5 bar
v_ion	$100 - 1000\frac{\mathrm{km}}{\mathrm{s}}$
v_e	$0.01 - 0.1c$
B	1 - 10 T
I_p	0.1 - 7 MA

Table 1: Typical Tokamak plasma values, taken from Ref. [38]

2 Confinement in a Tokamak

After several years of experiments on magnetically confined plasmas, the toroidal shape of the plasma column seems to be the best capable design for controlled magnetically confined fusion in outlook on creating a commercial fusion reactor. Beside other upcoming toroidal devices like Stellarators or Spheromaks, the Tokamak is at the moment the most auspicious design to satisfy most of the desired demands.

2.1 Tokamak Principle

In general the Tokamak principle can be expressed in few words: A magnetic field, closed to a torus, is for stability reasons overlapped by a weaker poloidal field; together they form a helically twisting magnetic field in toroidal symmetry. The plasma is confined by this fields and the charged particles are forced to gyrate around the field lines.
Poloidal field coils produce the toroidal field. The whole Tokamak acts as a transformer, where a central solenoid, positioned at vertical axis, acts as primary winding and the plasma itself as secondary winding (Ref. [38]). This effect drives a plasma current in toroidal direction and produces the poloidal magnetic field. See Figure 1. The central solenoid is mostly an iron core. The plasma itself is trapped inside a vacuum vessel on which the field coils are mounted externally. Typical Tokamak plasma values are mentioned in Table 1.

Toroidal symmetry leads to the destabilising effect of occuring drift forces due to the curvature of the magnetic field. A magnetic field gradient and the curvature itself try to establish MHD equilibrium, what means to straighten

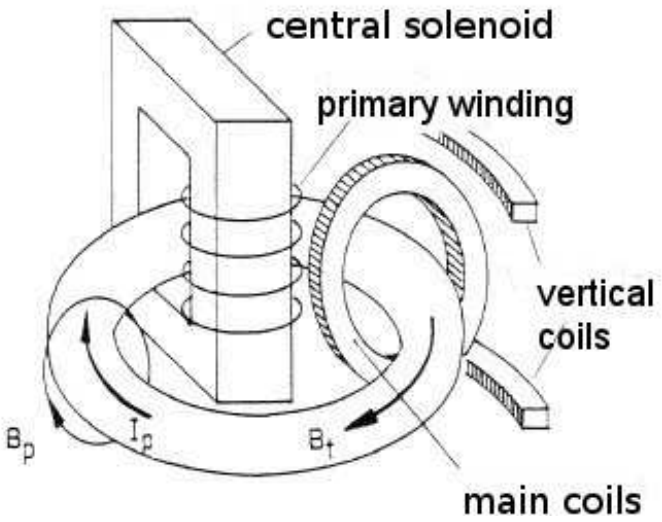

Figure 1: Structure of a Tokamak. Toroidal and poloidal field coils produce magnetic fields and confine the plasma. A toroidal plasma current is driven by the central solenoid and vertical field coils are needed to improve plasma shape and stability. Taken from Ref. [8]

the B-field lines again. For Tokamak equilibrium therefore a balance between plasma pressure and forces exerted by the B-field must be established. Here the so called pinch effect gets significance; a plasma column with a current flowing along the symmetry axis contracts radially until the inward directed Lorentz-force is balanced by the outward directed pressure gradient, (see Ref. [38])

$$\mathbf{j} \times \mathbf{B} = \nabla p. \tag{1}$$

It has been found, that better stability is reached if the plasma shape is modified (see Ref. [7]).
To satisfy the condition $\nabla \cdot \mathbf{B} = 0$, the toroidally spiralling B-field gets a radial dependence

$$B \propto \frac{1}{r}\ , \tag{2}$$

where r is the Tokamak minor radius. A physical magnetic model field then results in Equation (3),

$$\mathbf{B} = (0, B_\theta(r), B_z)(1 - \epsilon \cos\theta), \tag{3}$$

where θ is the poloidal angle, $\epsilon = \frac{r}{R}$ the ratio between both radii and B_θ, B_z are poloidal and toroidal magnetic field components (similar in Ref. [38]).

Coordinates in a Tokamak can be defined according to Ref. [38] like

$$x = (R_0 + r\cos\theta)\cos\phi, \tag{4}$$
$$y = (R_0 + r\cos\theta)\sin\phi, \tag{5}$$
$$z = r\sin\theta, \tag{6}$$
$$R = R_0 + r\cos\theta. \tag{7}$$

R_0 is the major radius, r the minor radius, (x, y, z) are cartesian coordinates expressed by toroidal coordinates, R is the effective radius, θ is the poloidal angle and ϕ is the toroidal angle. Toroidal effects like drift motion and mirror configurations for the helically twisting magnetic field can be calculated in these coordinates.
The Tokamak field from Equation (3) produces a magnetic field gradient which results in drift motion and magnetic mirror configurations inside the torus for particles with a low velocity parallel to the B-field. Because the plasma current I_p depends on r and has its maximum value at the toroidal symmetry axis $r = 0$, an externally applied vertical B-field (by additional coils) would couple to I_p and produce a radially inward directed force, which would stabilise the toroidal drift force.
As the established Tokamak equilibrium becomes independent of the azimuthal angle ϕ, in other words axis-symmetric, the force exerted on the plasma vanishes everywhere, like expressed by Equation (1). If now a B-field is added to Equation (1) by scalar product, one gets

$$\mathbf{B} \cdot \nabla p = 0, \tag{8}$$

what means that there do not exist pressure gradients along $\mathbf{B}$-field lines and $p = const.$ on radially nested surfaces, which are called *flux-surfaces*. Applying the same scalar method to the current density $\mathbf{j}$ with

$$\mathbf{j} \cdot \nabla p = 0, \tag{9}$$

one finds also the radially depending current lying on these flux-surfaces, see Figure 2.

While speaking about flux constant surfaces, it makes sense to define a poloidal flux function ψ. Also $\psi = const.$ on a flux surface what means

$$\mathbf{B} \cdot \nabla \psi = 0. \tag{10}$$

That is in analogy to Equation (8).

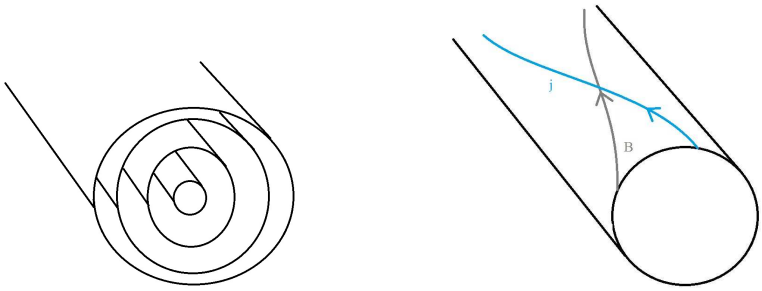

Figure 2: *left:* nested flux surfaces in toroidal symmetry. *right:* surfaces of current and magnetic field lines. Taken from Ref. [38]

2.2 Safety Factor q

Helically twisting magnetic field lines on flux surfaces perform both poloidal and toroidal transits over the torus. A ratio is defined as

$$q = \frac{m}{n} = \frac{\Delta\phi}{2\pi}. \tag{11}$$

Here m is the number of toroidal transits and n the number of poloidal transits and $\Delta\phi$ is the change in poloidal angle. Every flux surface has a different twist of magnetic field lines. A quantity called magnetic shear s describes the q-profile in dependence on minor radius r like

$$s\left(r\right) = \frac{q\left(r\right)}{r}. \tag{12}$$

It is possible to express q by poloidal and toroidal magnetic fields. Tracing a helically twisting field line, which takes a distance $\mathrm{d}s$ in poloidal direction while moving in toroidal direction for $\mathrm{d}\phi$ gives

$$\frac{R\mathrm{d}\phi}{\mathrm{d}s} = \frac{B_z}{B_\theta}, \tag{13}$$

what gives

$$q = \frac{1}{2\pi}\oint \frac{1}{R}\frac{B_z}{B_\theta}\,\mathrm{d}s, \tag{14}$$

where R is the major radius. From Amperes law, the q-profile may be derived to be inverse proportional to the plasma current I_p, see Ref. [38]. Typically, q reaches a minimum close to $r = 0$ and increases monotonically towards the

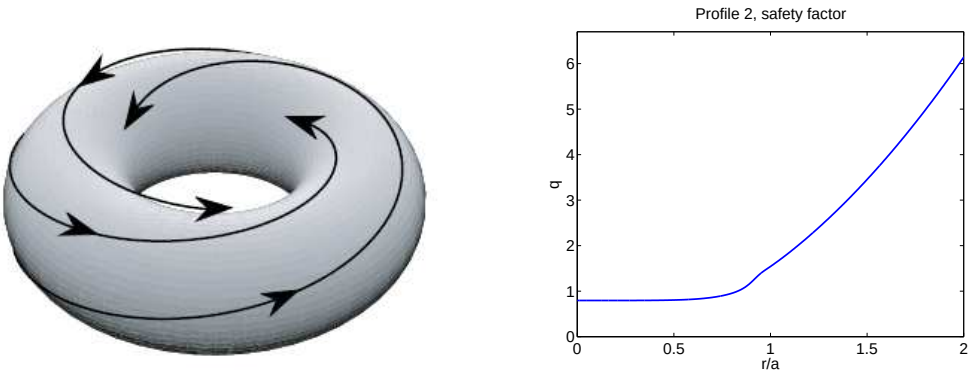

Figure 3: *left:* Magnetic field lines on a toroidally closed flux surface. A field line closes after m toroidal and n poloidal transits. Taken from Ref. [5]. *right:* General q-profile increasing with r.

plasma edge. This is essential to guarantee stability against MHD instabilities which result from plasma shape and B-field configuration. Better stability is achieved at higher values of q like mentioned in Refs. [11, 38]. If q takes an integer value, the magnetic field line closes one poloidal transit on the surface after q toroidal transits, see Figure 3. This defines the magnetic shear of each flux surface.

2.3 Fusion Process

The fusion process which gives the most hope for reaching a reactor regime, where the plasma is able to heat itself for operation, is the fusion of deuterium and tritium by reaction

$$ {}^{2}_{1}\mathrm{D} + {}^{3}_{1}\mathrm{T} \rightarrow {}^{4}_{2}\mathrm{He} + {}^{1}_{0}\mathrm{n} + \Delta\mathrm{E}. \tag{15} $$

For self heating the ion density should range at $n_\mathrm{i} = 5 \times 10^{20}\mathrm{m}^{-3}$, the ion temperature at $T_\mathrm{i} = 15\mathrm{keV}$ and the energy confinement time should be close to $\tau_\mathrm{E} = 4s$. Energies for resulting products of the fusion process in Equation (15) are $E\,(\mathrm{He}) = 3.5\mathrm{MeV}$ and $E\,(\mathrm{n}) = 14.1\mathrm{MeV}$, (see Refs. [7,38]). Such values give a favourable triple product $(n_\mathrm{i}\tau_\mathrm{E}T_\mathrm{i})$ which can already be reached in present day Tokamaks like JET, TFTR and JT-60. The high energetic α-particles can be used to heat the plasma. The key parameters are ion density n_i and confinement time τ_E, which can be expressed as ratio beween the total stored kinetic energy

and the required power to sustain the fusion in steady state,

$$\tau_{\mathrm{E}} = \frac{E_{\mathrm{kin}}}{P_{\mathrm{sus}}}. \tag{16}$$

Essential are cross section and mean free path, so particles in a fusion plasma have a long free path and collisions become possible although the cross sections are very small. Integrating over the distribution functions of both fusion partners, which are both assumed to be Maxwellian, a rate of reaction per unit volume can be derived, like it is done in Ref. [38]. After integration, the averaged product of cross section σ and relative velocity v gives a total reaction rate R per unit volume

$$R = n_{\mathrm{d}} n_{\mathrm{t}} \langle \sigma v \rangle, \tag{17}$$

depending on particle densities of deuterium n_{d} and tritium n_{t}.

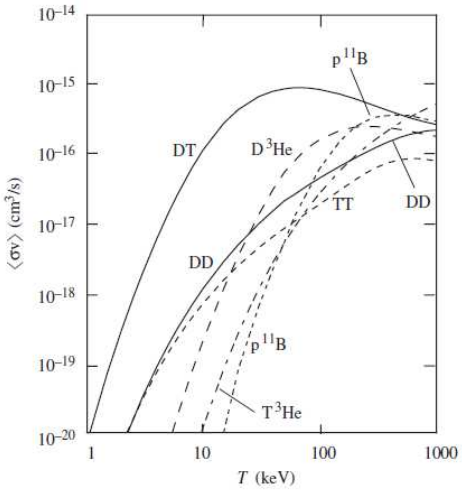

Figure 4: Cross section $\langle \sigma v \rangle$ for several fusion reactions depending on thermal energy. The DT-reaction has the highest cross section.

Multiplied by the energy release per reaction ε, Equation (17) gives the thermonuclear power per unit volume,

$$P_{TN} = n_d n_t \langle \sigma v \rangle \varepsilon. \tag{18}$$

The loss of energy is influenced by the energy confinement time. So the energy loss becomes

$$P_{\mathrm{L}} = \frac{P_{\mathrm{TN}}}{\tau_{\mathrm{E}}}. \tag{19}$$

For confinement we have to mention, that τ_e increases with plasma current I_p and decreases with increasing plasma pressure p.
Very important to avoid the confinement from deterioration is the handling of impurities, what means control of impurity transport and radiative losses. For that reason the plasma has to be isolated from the vessel material, to reduce sputtering and erosion of wall material. This is possible to be achieved either by limiters or by an additional magnetic field separatrix what is known as divertor configuration. High concentrations of impurity atoms and electrons resulting from ionistaion while atoms get inside the plasma core, deplete the efficiency of plasma heating as well as they harm the confinement. The handling of this problem leans on the idea to isolate the plasma from the wall material and leave the fusion core inside closed flux surfaces. This attends the existence of a last closed flux surface LCFS between fusion plasma and edge region.

Limiter

Limiters can be of various geometrical forms. The LCFS is tangent to the limiter what defines the plasma boundary. In other words, the plasma is in direct contact with the limiter material, see Figure 5. Limiters shape the plasma edge, define a boundary and protect the vessel wall before direct expose to plasma disruptions. Limiters are made of refractory material like carbon, molybdenum and tungsten. (see Refs. [7, 38])

Divertor

Towards limiters, the main difference is that divertors define the LCFS by a magnetic field separatrix. Immediately inside the separatrix follows the LCFS. The edge plasma is transported to the divertor target plates. Especially during H-regime, the radial transport through the separatrix is nearly vanishing. Impurities can be released fom the target plates by disruptions, they are ionised in the divertor plasma and the majority is transported again back to the target plates. The flow of impurities into the LCFS is strongly reduced but does not vanish completely.
The divertor concept offers some efficient methods of power handling on plasma facing components PFCs and divertor plates:

- adjusting the angle between field lines and target plates acts as flux expansion of the magnetic field, what reduces the power load,
- influencing transport properties and increasing power transfer to neutral

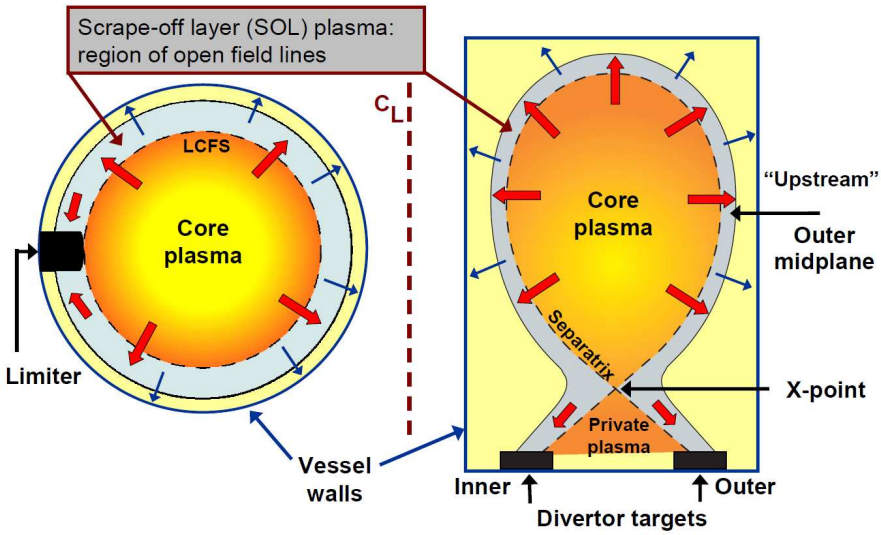

Figure 5: *left*: Limiter configuration. The limiter material is in contact with the plasma and defines the LCFS. *right:* Divertor configuration. Magnetic fields define the separatrix and the LCFS isolates the inner core. Taken from Ref. [24].

particles.

Yet there are no absolute satisfactory solutions, and improvements are desired in Ref. [38] like

- removal of α-particle power by heat transport,
- efficient use of α-particle power for plasma heating,
- operating at lower temperature of the divertor plasma to reduce sputtering,
- removal of helium ash,
- power loss by radiation.

Due to plasma wall interactions, a rise of neutrals density at the edge would lead to recombination and decelerations of ions, resulting in radiative losses. This radiation called MARFEs, releases power at X-point and on divertor targets and must be handeled with care.
For design diversity of divertors, several ideas exist. All of them base on the same concept of defining a LCFS by magnetic fields where the edge plasma is transported to divertor plates, like already explained. JET and ITER divertors

are operating at *single null* configuration with only one X-point. DIII-D uses a *double null* configuration with two X-points, see Figure 6.

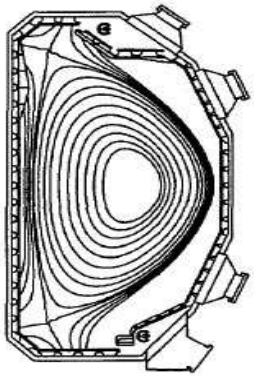

Figure 6: Double null divertor configuration at DIII-D, taken from Ref. [29]. Two x-points and an inner core with high triangularity is achieved.

The advantage is that interaction area of divertor targets is doubled and a higher triangularity of the plasma shape allows a higher pressure and β regime; a disadvantage for two X-points is that the connection length of particles doubles (see Ref. [38]). Other divertor types like DED at TEXTOR produce a rotating ergodic field.

3 Model Description

3.1 MHD Modelling

Starting from the set of ideal MHD-equations

$$\begin{aligned}
\mathbf{E} + \frac{1}{c}\mathbf{v} \times \mathbf{B} &= 0, && (20)\\
\nabla \times \mathbf{E} + \frac{1}{c}\frac{\partial \mathbf{B}}{\partial t} &= 0, && (21)\\
\nabla \times \mathbf{B} &= \frac{4\pi}{c}\mathbf{j}, && (22)\\
\nabla \cdot \mathbf{B} &= 0, && (23)\\
\rho \frac{\mathrm{d}\mathbf{v}}{\mathrm{d}t} &= \frac{1}{c}\mathbf{j} \times \mathbf{B} - \nabla p, && (24)\\
\frac{\mathrm{d}}{\mathrm{d}t}\left(\frac{p}{\rho^{\gamma}}\right) &= 0, && (25)\\
\frac{\partial \rho}{\partial t} + \nabla\left(\rho \mathbf{v}\right) &= 0, && (26)
\end{aligned}$$

as basis to describe the plasma configuration, the expansion of all quantities is done like

$$Q\left(\mathbf{x}, t\right) = Q_0\left(\mathbf{x}\right) + Q_1\left(\mathbf{x}, t\right). \quad (27)$$

The zero order is the equilibrium contribution and the first order is the perturbation contribution (see e.g. Refs. [11, 38]). There, $\frac{\mathrm{d}}{\mathrm{d}t} = \left(\frac{\partial}{\partial t} + \mathbf{v} \cdot \nabla\right)$, $\gamma = \frac{5}{3}$ is the adiabatic constant, ρ is the mass density, p the pressure, c the speed of light, $\mathbf{j}$ the current density, $\mathbf{v}$ the plasma velocity, $\mathbf{B}$ and $\mathbf{E}$ the magnetic and electric field. Vector $\mathbf{x}$ is the position vector in general symmetry, parameter t is the time variable. If perturbations are small, $\frac{|Q_1|}{|Q_0|} \ll 1$, terms containing products of first order terms can be neglected. The equilibrium is assumed not to be time dependent and satisfies

$$\begin{aligned}
\nabla \times \mathbf{E}_0 &= 0, && (28)\\
\nabla \times \mathbf{B}_0 &= \frac{4\pi}{c}\mathbf{j}_0, && (29)\\
\nabla \cdot \mathbf{B} &= 0, && (30)
\end{aligned}$$

$$\nabla \cdot \rho_0 \mathbf{v}_0 = 0, \tag{31}$$

$$\rho_0 \mathbf{v}_0 \cdot \nabla \mathbf{v}_0 = -\nabla p_0 + \frac{1}{c}\mathbf{j}_0 \times \mathbf{B}_0, \tag{32}$$

$$\mathbf{E}_0 + \frac{1}{c}\mathbf{v}_0 \times \mathbf{B}_0 = 0, \tag{33}$$

$$\mathbf{v}_0 \cdot \nabla \left(\frac{p_0}{\rho_0^\gamma}\right) = 0. \tag{34}$$

If there is no equilibrium electric field $\mathbf{E}_0 = 0$, and no plasma equilibrium flows $\mathbf{v}_0 = 0$, the equilibrium MHD equations simplify to

$$\nabla \cdot \mathbf{B} = 0, \tag{35}$$

$$\nabla p_0 = \frac{1}{4\pi}(\nabla \times \mathbf{B}_0) \times \mathbf{B}_0. \tag{36}$$

The perturbed MHD-equations are:

$$\frac{\partial \rho_1}{\partial t} + \nabla \cdot \rho_1 \mathbf{v}_0 + \nabla \cdot \rho_0 \mathbf{v}_1 = 0, \tag{37}$$

$$\rho_0 \frac{\partial \mathbf{v}_1}{\partial t} + \rho_1 \mathbf{v}_0 \cdot \nabla \mathbf{v}_0 + \rho_0 \mathbf{v}_1 \cdot \nabla \mathbf{v}_0 + \rho_0 \mathbf{v}_0 \cdot \nabla \mathbf{v}_1 =$$
$$= -\nabla p_1 + \frac{1}{4\pi}\left[(\nabla \times \mathbf{B}_0) \times \mathbf{B}_1 + (\nabla \times \mathbf{B}_1) \times \mathbf{B}_0\right], \tag{38}$$

$$\frac{\partial}{\partial t}\left(\frac{p_1}{\rho_0^\gamma}\right) - \frac{\partial}{\partial t}\left(\frac{\gamma p_0 \rho_1}{\rho_0^{\gamma+1}}\right) =$$
$$= -\mathbf{v}_1 \cdot \nabla \left(\frac{p_0}{\rho_0^\gamma}\right) - \mathbf{v}_0 \cdot \nabla \left(\frac{p_1}{\rho_0^\gamma}\right) + \mathbf{v}_0 \cdot \nabla \left(\frac{p_0 \gamma \rho_1}{\rho_0^{\gamma+1}}\right), \tag{39}$$

$$\frac{1}{c}\frac{\partial \mathbf{B}_1}{\partial t} + \nabla \times \mathbf{E}_1 = 0, \tag{40}$$

$$\nabla \times \mathbf{B}_1 = \frac{4\pi}{c}\mathbf{j}_1, \tag{41}$$

$$\mathbf{E}_1 + \frac{1}{c}\mathbf{v}_1 \times \mathbf{B}_0 + \frac{1}{c}\mathbf{v}_0 \times \mathbf{B}_1 = 0, \tag{42}$$

$$\nabla \cdot \mathbf{B}_1 = 0. \tag{43}$$

It is common to express the perturbations by means of the displacement vector $\boldsymbol{\xi}$ of a plasma element which is dislocated from it's equilibrium position $\mathbf{x}_0$.

$$\boldsymbol{\xi}(\mathbf{x}, t) = \mathbf{x} - \mathbf{x}_0. \tag{44}$$

The perturbed velocity in terms of the displacement vector and the equilibrium velocity are

$$\mathbf{v_1}(\mathbf{x}, t) = \frac{\partial \boldsymbol{\xi}(\mathbf{x}, t)}{\partial t} + \mathbf{v}_0 \cdot \nabla \boldsymbol{\xi} - \boldsymbol{\xi} \cdot \nabla \mathbf{v}_0. \tag{45}$$

With substitution to the perturbed and equilibrium MHD-equations, the perturbed first order quantities ρ_1, p_1, $\mathbf{B}_1$, $\mathbf{j}_1$ can be expressed in terms of the plasma displacement $\boldsymbol{\xi}(\mathbf{x}, t)$ as

$$\begin{aligned} \rho_1 &= -\nabla \cdot (\rho_0 \boldsymbol{\xi}), && (46) \\ p_1 &= -\boldsymbol{\xi} \cdot \nabla p_0 - \gamma p_0 (\nabla \cdot \boldsymbol{\xi}), && (47) \\ \mathbf{B}_1 &= \nabla \times (\boldsymbol{\xi} \times \mathbf{B}_0), && (48) \\ \mathbf{j}_1 &= \frac{1}{4\pi} (\nabla \times (\nabla \times (\boldsymbol{\xi} \times \mathbf{B}_0))). && (49) \end{aligned}$$

The equilibrium flow $\mathbf{v}_0$ does not enter explicitely to ρ_1, p_1, $\mathbf{B}_1$, $\mathbf{j}_1$ and the perturbed quantities have the same form like in the flowless case.
A substitution of Equation (45) into the linearised force balance Equation (38) yields

$$\rho_0 \frac{\partial^2 \boldsymbol{\xi}}{\partial t^2} + 2\rho_0 (\mathbf{v}_0 \cdot \nabla) \frac{\partial \boldsymbol{\xi}}{\partial t} = \mathbf{F}(\boldsymbol{\xi}) + \nabla \cdot [\rho_0 \boldsymbol{\xi} (\mathbf{v}_0 \cdot \nabla) \mathbf{v}_0 - \rho_0 \mathbf{v}_0 (\mathbf{v}_0 \cdot \nabla) \boldsymbol{\xi}]. \quad (50)$$

After Fourier transformation in time, the linearised compressible ideal MHD equations with finite equilibrium flows $\mathbf{v}_0$ can be written with the help of the Lagrangian displacement vector $\boldsymbol{\xi}$ from Equation (44) as (see, e.g. Ref. [11])

$$-\omega^2 \rho_0 \boldsymbol{\xi} = \mathbf{F}_f(\boldsymbol{\xi}), \quad (51)$$

where the force operator $\mathbf{F}_f(\boldsymbol{\xi})$ is a function of the plasma displacement. The force operator with flows $\mathbf{F}_f(\boldsymbol{\xi})$ can be expressed by the force operator without flows $\mathbf{F}(\boldsymbol{\xi})$ like

$$\mathbf{F}_f(\boldsymbol{\xi}) = \mathbf{F}(\boldsymbol{\xi}) + \nabla \cdot [\rho_0 \boldsymbol{\xi} (\mathbf{v}_0 \cdot \nabla) \mathbf{v}_0 - \rho_0 \mathbf{v}_0 (\mathbf{v}_0 \cdot \nabla) \boldsymbol{\xi}] + 2i\omega\rho_0 (\mathbf{v}_0 \cdot \nabla) \boldsymbol{\xi}, \quad (52)$$

with

$$\begin{aligned} \mathbf{F}(\boldsymbol{\xi}) = \nabla (\boldsymbol{\xi} \cdot \nabla p_0 + \gamma p_0 (\nabla \cdot \boldsymbol{\xi})) + \\ + \frac{1}{4\pi} [(\nabla \times \mathbf{B}_0) \times (\nabla \times (\boldsymbol{\xi} \times \mathbf{B}_0)) + (\nabla \times (\nabla \times (\boldsymbol{\xi} \times \mathbf{B}_0))) \times \mathbf{B}_0]. \quad (53) \end{aligned}$$

3.1.1 MHD Eigenequation in Cylindrical Symmetry

In cylindrical symmetry one can expand all perturbations in the form

$$Q_1(\mathbf{x}, t) = \tilde{Q}_1(r) \exp(im\theta + ikz - i\omega t), \quad (54)$$

where m is the toroidal mode number and $k = \frac{n}{R}$ is the z-component of the wave vector, n is the poloidal mode number and R the major toroidal radius.

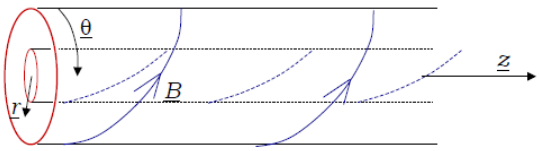

$$\begin{aligned}\boldsymbol{\xi} &= \xi_r \mathbf{e}_r + \xi_\theta \mathbf{e}_\theta + \xi_z \mathbf{e}_z, \\ \mathbf{B}_1 &= B_{1r}\mathbf{e}_r + B_{1\theta}\mathbf{e}_\theta + B_{1z}\mathbf{e}_z, \\ \mathbf{B}_0 &= B_{0\theta}\mathbf{e}_\theta + B_{0z}\mathbf{e}_z.\end{aligned}$$

Figure 7: Cylindric symmetry. The equilibrium magnetic field has no radial component, taken from Ref. [27].

All vector quantities are expressed in cylindrical coordinates by means of the cylindrical basis vectors $(\mathbf{e}_r, \mathbf{e}_\theta, \mathbf{e}_z)$,

Note that the equilibrium magnetic field is assumed to have no radial component, see Figure 7.
A substitution of Equation (54) into the first order equations allows to calculate the components of the perturbation magnetic field $\mathbf{B}_1$ in Equation (48). After a transformation to the Fourier-space of toroidal and poloidal harmonics (m, n), the Fourier amplitudes of $\tilde{\mathbf{B}}_1$ are

$$\tilde{B}_{1r} = i\left(\frac{m}{r}B_{0\theta} + kB_{0z}\right)\xi_r, \tag{55}$$

$$\tilde{B}_{1\theta} = -\left(\xi_r B_{0\theta}\right)' - ik\left(B_{0\theta}\xi_z - B_{0z}\xi_\theta\right), \tag{56}$$

$$\tilde{B}_{1z} = -\frac{1}{r}\left(rB_{0z}\xi_r\right)' + \frac{im}{r}\left(B_{0\theta}\xi_z - B_{0z}\xi_\theta\right). \tag{57}$$

The prime marks the radial derivative, the zero index the equilibrium quantity. The θ and z components of Equation (51) provide expressions for ξ_θ and ξ_z. The resulting equations for ξ_θ and ξ_z represent an algebraic system of two equations. This is true only if there are no radial equilibrium flows ($v_r = 0$) because v_r would contribute terms of radial derivatives ξ_θ' and ξ_z'.
The equations for ξ_θ and ξ_z can be written in the form

$$\xi_\theta H^{-1} = \xi_r\Gamma_\theta + \left(r\xi_r\right)'\frac{iGB_z}{4\pi r} + \xi_z\psi + \left(\nabla\cdot\boldsymbol{\xi}\right)\chi_\theta, \tag{58}$$

$$\xi_z N^{-1} = \xi_r\Gamma_z - \left(r\xi_r\right)'\frac{iGB_\theta}{4\pi r} + \xi_\theta\psi + \left(\nabla\cdot\boldsymbol{\xi}\right)\chi_z, \tag{59}$$

with

$$k_0^2 = \frac{m^2}{r^2} + k^2 \quad , \quad G = \frac{m}{r}B_z - kB_\theta, \tag{60}$$

$$H^{-1} = \rho_0 \left(-\omega^2 - 2i\omega f + \frac{k_0^2 B_z^2}{4\pi\rho_0} + \nabla \cdot (\rho_0 \mathbf{v}_0) \frac{f}{\rho_0} + f^2 \right), \quad (61)$$

$$N^{-1} = \rho_0 \left(-\omega^2 - 2i\omega f + \frac{k_0^2 B_\theta^2}{4\pi\rho_0} + \nabla \cdot (\rho_0 \mathbf{v}_0) \frac{f}{\rho_0} + f^2 \right), \quad (62)$$

$$f = \frac{im}{r} v_\theta + ikv_z. \quad (63)$$

and

$$\chi_\theta = \frac{im}{r} \gamma p_0, \qquad \chi_z = ik\gamma p_0, \quad (64)$$

with

$$\Gamma_\theta = \rho_0 \left(2i\omega \frac{v_\theta}{r} - \nabla \cdot (\rho_0 \mathbf{v}_0) \frac{v_\theta}{r\rho_0} + \frac{v_\theta}{r} f + 2ik \frac{B_\theta B_z}{4\pi r} \right), \quad (65)$$

$$\Gamma_z = -2ik \frac{B_\theta^2}{4\pi r}, \quad (66)$$

$$\psi_\theta = \psi_z = \psi = \frac{k_0^2 B_\theta B_z}{4\pi}. \quad (67)$$

After Fourier transformation to m and n harmonics, the divergence of the displacement vector

$$\nabla \cdot \boldsymbol{\xi} = \frac{1}{r} (r\xi_r)' + \frac{im}{r} \xi_\theta + ik\xi_z, \quad (68)$$

can be used in Equations (58) - (59) to obtain

$$\xi_\theta = X_\theta \left(Q_\theta \xi_r + W_\theta (r\xi_r)' \right), \quad (69)$$

$$\xi_z = X_z \left(Q_z \xi_r + W_z (r\xi_r)' \right), \quad (70)$$

with

$$Q_\theta = \Gamma_\theta + \frac{N\alpha}{1-ikN\chi_z}\Gamma_z, \tag{71}$$

$$Q_z = \Gamma_z + \frac{H\beta}{1-\frac{im}{r}H\chi_\theta}\Gamma_\theta, \tag{72}$$

$$X_\theta = \left(\frac{1-\frac{im}{r}H\chi_\theta}{H} - \frac{N\alpha\beta}{1-ikN\chi_z}\right)^{-1}, \tag{73}$$

$$X_z = \left(\frac{1-ikN\chi_z}{N} - \frac{H\alpha\beta}{1-\frac{im}{r}H\chi_\theta}\right)^{-1}, \tag{74}$$

$$W_\theta = \frac{iGB_z}{4\pi r} + \frac{\chi_\theta}{r} + \frac{NK\alpha}{1-ikN\chi_z}, \tag{75}$$

$$W_z = \frac{H\beta}{1-\frac{im}{r}H\chi_\theta}\left(\frac{iGB_z}{4\pi r} + \frac{\chi_\theta}{r}\right) + K, \tag{76}$$

where

$$K = \frac{\chi_z}{r} - \frac{iGB_\theta}{4\pi r}, \qquad \beta = \psi + \frac{im}{r}\chi_z, \tag{77}$$

$$\alpha = \psi + ik\chi_\theta. \tag{78}$$

Like already mentioned, the Θ and z component of the eigenequation (Equation (51)) represent an algebraic system of two equations for ξ_θ and ξ_z. After substitution of ξ_θ and ξ_z to Equation (51), the radial component ξ_r satisfies the following ordinary differential equation

$$\begin{aligned}
-\rho_0\omega^2\xi_r &= \frac{\mathrm{d}}{\mathrm{d}r}\left[\gamma p_0\left(\nabla\cdot\boldsymbol{\xi}\right) + \frac{B^2}{4\pi r}\left(r\xi_r\right)' + \frac{iG}{4\pi}\left(\xi_\theta B_z - \xi_z B_\theta\right)\right] \\
&- \xi_r\left[\nabla\cdot\left(\rho_0\mathbf{v}_0\right)f + \rho_0 f^2 - \rho_0\frac{v_\theta^2}{r^2} + \rho_0\left(\frac{v_\theta^2}{r}\right)' - 2i\omega\rho_0 f + \frac{F^2}{4\pi} + \frac{r}{4\pi}\left(\frac{B_\theta^2}{r^2}\right)'\right] \\
&+ \xi_\theta\left[-2i\omega\rho_0\frac{v_\theta}{r} - 2ik\frac{B_\theta B_z}{4\pi r} + \nabla\cdot\left(\rho_0\mathbf{v}_0\right)\frac{v_\theta}{r}\right] \\
&+ \xi_z\left[2ik\frac{B_\theta^2}{4\pi r}\right] - \nabla\cdot\left(\rho_0\boldsymbol{\xi}\right)\frac{v_\theta^2}{r},
\end{aligned} \tag{79}$$

with

$$\nabla\cdot\left(\rho_0\boldsymbol{\xi}\right) = \rho_0\left(\nabla\cdot\boldsymbol{\xi}\right) + \rho_0'\xi_r \quad , \quad F = \frac{m}{r}B_z + kB_\theta. \tag{80}$$

Defining two additional functions

$$\begin{aligned}
\lambda &= \rho_0 \left(\nabla \cdot (\rho_0 \mathbf{v}_0) \frac{f}{\rho_0} + f^2 - \frac{v_\theta^2}{r^2} + \left(\frac{v_\theta^2}{r} \right)' - 2i\omega f + \frac{F^2}{4\pi\rho_0} + \frac{r}{4\pi\rho_0} \left(\frac{B_\theta^2}{r^2} \right)' + \frac{\rho_0'}{\rho_0} \frac{v_\theta^2}{r} \right), \\
\epsilon &= -2i\omega \frac{v_\theta}{r} - 2ik \frac{B_\theta B_z}{4\pi r \rho_0} + \nabla \cdot (\rho_0 \mathbf{v}_0) \frac{v_\theta}{r\rho_0},
\end{aligned} \tag{81}$$

the radial force balance from Equation (79) becomes

$$\begin{aligned}
0 &= \frac{\mathrm{d}}{\mathrm{d}r} \left[\xi_r \left(X_\theta Q_\theta \left(\gamma p_0 \frac{im}{r} + \frac{iGB_z}{4\pi} \right) + X_z Q_z \left(\gamma p_0 ik - \frac{iGB_\theta}{4\pi} \right) \right) \right. \\
&\quad \left. + (r\xi_r)' \left(\gamma p_0 \frac{1}{r} + \frac{B^2}{4\pi r} + X_\theta W_\theta \left(\gamma p_0 \frac{im}{r} + \frac{iGB_z}{4\pi} \right) + X_z W_z \left(\gamma p_0 ik - \frac{iGB_\theta}{4\pi} \right) \right) \right] \\
&\quad + \xi_r \left[\rho_0 \omega^2 - \lambda + X_\theta Q_\theta \left(\epsilon - \rho_0 \frac{im}{r} \frac{v_\theta^2}{r} \right) + X_z Q_z \left(2ik \frac{B_\theta^2}{4\pi r} - ik\rho_0 \frac{v_\theta^2}{r} \right) \right] \\
&\quad + (r\xi_r)' \left[-\frac{\rho_0}{r} \frac{v_\theta^2}{r} + X_\theta W_\theta \left(\epsilon - \rho_0 \frac{im}{r} \frac{v_\theta^2}{r} \right) + X_z W_z \left(2ik \frac{B_\theta^2}{4\pi r} - ik\rho_0 \frac{v_\theta^2}{r} \right) \right].
\end{aligned} \tag{82}$$

This differential equation can be written as a system of two first order partial differential equations,

$$\frac{AS}{r} \frac{\mathrm{d}}{\mathrm{d}r} (r\xi_r) = C_{11} (r\xi_r) - C_{12} p^*, \tag{83}$$

$$AS \frac{\mathrm{d}}{\mathrm{d}r} p^* = C_{21} (r\xi_r) - C_{22} p^*, \tag{84}$$

like in Refs. [2,3]. If one defines a generalised pressure p^* as

$$p^* = -\gamma p_0 \nabla \cdot \boldsymbol{\xi} - \boldsymbol{\xi} \cdot \nabla p_0 + \frac{\mathbf{B}_0 \cdot \mathbf{B}_1}{4\pi}. \tag{85}$$

The remaining coefficients are

$$A = \rho_0 \tilde{\omega}^2 - \frac{F^2}{4\pi}, \tag{86}$$

$$S = \left(\frac{B_0^2}{4\pi} + \gamma p_0 \right) \rho_0 \tilde{\omega}^2 - \gamma p_0 \frac{F^2}{4\pi}, \tag{87}$$

$$T = \frac{FB_\theta}{4\pi} + \rho_0 \tilde{\omega} v_\theta, \tag{88}$$

$$Q = \rho_0 \tilde{\omega}^2 \left(\frac{B_{0\theta}^2}{4\pi} - \rho_0 v_{0\theta}^2 \right) + \frac{\rho_0}{4\pi} \left(B_{0\theta} \tilde{\omega} + F v_{0\theta} \right)^2, \tag{89}$$

with

$$
\begin{aligned}
C_{11} &= \rho_0\tilde{\omega}^2\frac{Q}{r^2} - 2m\frac{ST}{r^3}, && (90)\\
C_{12} &= \rho_0^2\tilde{\omega}^4 - \left(k^2 + \frac{m^2}{r^2}\right)S, && (91)\\
C_{21} &= \frac{AS}{r}C_4 - 4\frac{ST^2}{r^3} + \frac{Q^2}{r^3}, && (92)\\
C_{22} &= r\,C_{11}, && (93)\\
C_4 &= A + r\frac{\mathrm{d}}{\mathrm{d}r}\left(\frac{B_{0\theta}^2 - 4\pi\rho_0 v_{0\theta}^2}{4\pi r^2}\right). && (94)
\end{aligned}
$$

Here, $\tilde{\omega}$ is the Doppler shifted frequency

$$\tilde{\omega} = \omega - \frac{mv_{0\theta}}{r} - kv_{0z}. \qquad (95)$$

The solutions of the two first order differential equation system (Equation (83) and Equation (84)), are $(r\xi_r)$ and p^*. From p^* in Equation (85) it is then possible to compute $(r\xi_r)'$ as a function of p^*:

$$
\begin{aligned}
p^* &= -\kappa + \Lambda\,\xi_\theta + \Xi\,\xi_z && (96)\\
&= -\kappa + \Lambda X_\theta Q_\theta \xi_r + \Lambda X_\theta W_\theta\,(r\xi_r)' + \Xi X_z Q_z \xi_r + \Xi X_z W_z\,(r\xi_r)'\\
&= -\gamma p_0\frac{1}{r}\,(r\xi_r)' - \frac{B_\theta^2}{4\pi r}\xi_r' - \frac{B_\theta B_\theta'}{4\pi}\xi_r - \frac{B_z^2}{4\pi r}\,(r\xi_r)' - \frac{B_z B_z'}{4\pi}\xi_r - p_0'\xi_r + \Lambda X_\theta Q_\theta \xi_r +\\
&\quad + \Lambda X_\theta W_\theta\,(r\xi_r)' + \Xi X_z Q_z \xi_r + \Xi X_z W_z\,(r\xi_r)'\\
&= (r\xi_r)'\left[-\frac{B_\theta^2}{4\pi r} - \gamma p_0\frac{1}{r} - \frac{B_z^2}{4\pi r} + \Lambda X_\theta W_\theta + \Xi\,X_z W_z\right]\\
&\quad + \xi_r\left[\frac{B_\theta^2}{4\pi r} - \frac{B_\theta B_\theta'}{4\pi} - \frac{B_z B_z'}{4\pi} + \Lambda X_\theta Q_\theta + \Xi\,X_z Q_z - p_0'\right], && (97)
\end{aligned}
$$

what finally leads to

$$(r\xi_r)' = \frac{p^* - \xi_r\left(\frac{B_\theta^2}{4\pi r} - \frac{B_\theta B_\theta'}{4\pi} - \frac{B_z B_z'}{4\pi} + \Lambda X_\theta Q_\theta + \Xi\,X_z Q_z - p_0'\right)}{\left(-\frac{B_\theta^2}{4\pi r} - \gamma p_0\frac{1}{r} - \frac{B_z^2}{4\pi r} + \Lambda X_\theta W_\theta + \Xi\,X_z W_z\right)}, \qquad (98)$$

where

$$\kappa = \gamma\frac{p_0}{r}\left(r\xi_r\right)' + \frac{B_\theta}{4\pi}\left(\xi_r B_\theta\right)' + \frac{B_z}{4\pi r}\left(rB_z\xi_r\right)' + p_0'\xi_r, \tag{99}$$

$$\Lambda = -\chi_\theta + \frac{B_\theta B_z}{4\pi}ik - \frac{B_z^2 im}{4\pi r}, \tag{100}$$

$$\Xi = -\chi_z + \frac{B_\theta B_z im}{4\pi r} - \frac{B_\theta^2}{4\pi}ik. \tag{101}$$

3.1.2 Matching Conditions

Inside the plasma region, model equations obtained from the magnetohydrodynamic model (Sec. 3.1) are solved. A linear system of equations is assembled and solved to determine superposition coefficients for fundamental solutions of eigenfunctions in the plasma region, what is discussed in the following.
For an arbitrary complex mode frequency ω, the system determinant $\det \mathbf{G}\left(\omega\right)$ is nonzero and therefore the solution (all superposition coefficients) is zero since there are no sources (rhs equals zero) in the system. Finite nonzero solutions that correspond to stable or unstable eigenmodes (depending on the sign of the imaginary part of the eigenfrequency) are possible only when the determinant is zero. A complex root solver is used to find all roots of the dispersion equation $\det \mathbf{G}\left(\omega\right) = 0$, numerically.
The radial integration starts from two different boundaries and returns two fundamental solutions, which are superposed afterwards. In the plasma column the integration starting points are

$$r = 0 \quad , \; r = r_\mathrm{p}, \tag{102}$$

at the cylinder axis and at the plasma radius, like this is shown in Figure 8. Because of Equation (83) is getting singular at $r \to 0$, a very small value $r = 10^{-2}$cm is there used as radial starting point of the numerical integration. Both integrations match each other at an arbitrary matching position, (see Ref. [11]).

$$r = r_\mathrm{A} \quad , \quad r_\mathrm{A} \,\epsilon\, \left[0, r_\mathrm{p}\right],$$

with boundary conditions

$$\left(r\xi_\mathrm{r}\right)_{r=0} = 0, \qquad \left(r\xi_\mathrm{r}\right)_{r=r_\mathrm{p}} = 0, \tag{103}$$

$$\left(r\xi_\mathrm{r}\right)'_{r=0} = 1, \qquad \left(r\xi_\mathrm{r}\right)'_{r=r_\mathrm{p}} = 1. \tag{104}$$

The prime marks the radial derivative. As a result, the integration provides two fundamental solutions ξ_1 and ξ_2, which should be continuous at matching

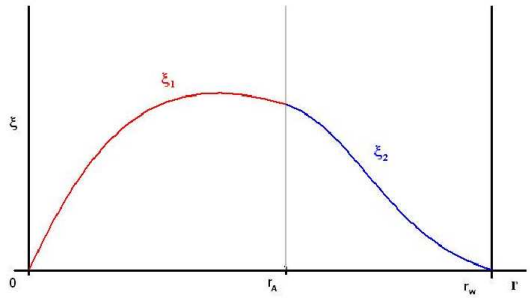

Figure 8: Two different intergations starting from z-axis and plasma radius r_{p}. Both solutions match at $r = r_{\mathrm{A}}$ where the fundamental solutions of integration ξ_1 and ξ_2 must be continuous.

point $r = r_{\mathrm{A}}$. The choice of boundary conditions is arbitrary for the derivative values in Equation (104), see Ref. [11], mostly they are set to unity. Attention has to be paid to the boundary conditions in Equation (103). These values are very sensitive on the different kinds of MHD modes. Concerning kink modes, the used boundary conditions in Equation (103) are set to zero, like this was suggested in Ref. [11].
A combined solution covering the whole radial range of the plasma column is constructed by superposition like

$$\xi_r = \begin{cases} C_1\xi_1 & , \; r \; \epsilon \; (0, r_{\mathrm{A}}) \, , \\ C_2\xi_2 & , \; r \; \epsilon \; (r_{\mathrm{A}}, r_{\mathrm{p}}) \, , \end{cases}$$

$$C_1 \; , \; C_2 \; = const. \tag{105}$$

At matching position r_{A}, the continuity of the fundamental solutions determines a homogeneous system, which equals the solutions from both sides:

$$\begin{aligned} C_1\xi_1 &= C_2\xi_2 \\ C_1\xi_1' &= C_2\xi_2' \end{aligned} \qquad \Rightarrow \qquad G\left(\omega\right) = \begin{bmatrix} \xi_1 & -\xi_2 \\ \\ \xi_1' & -\xi_2' \end{bmatrix} . \tag{106}$$

Matrix $\mathbf{G}$ remains to be a function of the frequency ω. The homogeneous system is solvable for such frequencies ω, that

$$\det \mathbf{G}\left(\omega\right) = 0. \tag{107}$$

3.2 Kinetic Modelling

Both the kinetic and the MHD model are based on a numerical solution of the full set of Maxwell equations in cylindrical geometry. The difference occurs in the application of the plasma current density. This section discusses the approximations and basic steps of the method developed in Refs. [16, 20]. Following Mahajan-Chen [23], action-angle variables are used to solve the linearised Vlasov equation (no gyroaveraging) analytically with a simplified one-dimensional Fokker-Planck collision operator (Ornstein-Uhlenbeck approximation). The background distribution function is taken in the form of an inhomogeneous drifting Maxwellian with parameters derived from the plasma and magnetic field profiles that satisfy the MHD equilibrium. Maxwell equations with displacement and plasma current densities together with the appropriate boundary conditions for an ideal or a resistive wall are solved numerically to find the eigenmodes existing in the system by a direct complex root search procedure.

The code KiLCA (Kinetic Linear Cylindrical Approximation) is a wave code based on the described kinetic model of the tokamak plasma in a periodic cylinder geometry (Refs. [16,20]). The code has been successfully used (Refs. [17,21]) to study kinetic effects of the interaction of resonant magnetic perturbations and the plasma in particular near resonant magnetic surfaces.

Following the linear kinetic model of a cylindrical inhomogeneous screw pinch plasma introduced in Ref. [16] and recently upgraded in Ref. [20], the wave fields $(\tilde{\mathbf{E}}, \tilde{\mathbf{B}})$ with frequency ω are obtained from Maxwell's equations,

$$\nabla \times \tilde{\mathbf{E}} = \frac{i\omega}{c}\tilde{\mathbf{B}}, \qquad \nabla \times \tilde{\mathbf{B}} = -\frac{i\omega}{c}\tilde{\mathbf{E}} + \frac{4\pi}{c}\tilde{\mathbf{j}}, \tag{108}$$

are solved numerically together with an appropriate set of boundary conditions, mentioned in Sec. 4. The plasma response current density in Equation (108) is evaluated as

$$\tilde{\mathbf{j}} = \sum_{\alpha=\{e,i\}} e_\alpha \int \mathrm{d}^3 p\, \mathbf{v} \tilde{f}_\alpha, \tag{109}$$

where e_α is a charge of specii α, $\mathbf{v}$ is the velocity variable and $\tilde{f}_\alpha$ the perturbed distribution function (in the following we omit index α for brevity). The particle distribution function $\mathbf{f}(\mathbf{r}, \mathbf{v}, t)$ enters the kinetic equation like

$$\frac{\mathrm{d}f}{\mathrm{d}t} = \frac{\partial f}{\partial t} + \mathbf{v} \cdot \frac{\partial f}{\partial \mathbf{r}} + \frac{\mathbf{F}}{m} \cdot \frac{\partial f}{\partial \mathbf{v}} = L_C f, \tag{110}$$

with particles at position $\mathbf{r}$ and velocity $\mathbf{v}$ exposed to the Lorentz force $\mathbf{F} = e\left(\mathbf{E} + \frac{1}{c}\mathbf{v} \times \mathbf{B}\right)$. The quantity L_C represents the collision operator and is specified later in this section.

The application of linearisation of the distribution function, the magnetic and the electric field like

$$f = f_0 + \tilde{f}, \quad \mathbf{B} = \mathbf{B}_0 + \tilde{\mathbf{B}}, \quad \mathbf{E} = \mathbf{E}_0 + \tilde{\mathbf{E}}, \tag{111}$$

and the use of derivations with respect to the momentum ($\frac{\partial}{\partial \mathbf{v}} \rightarrow m\frac{\partial}{\partial \mathbf{p}}$) yield the linearised form of Equation (110), as

$$\frac{\partial \tilde{f}}{\partial t} + \mathbf{v} \cdot \nabla \tilde{f} + e\left(-\nabla\Phi_0 + \frac{1}{c}\mathbf{v} \times \mathbf{B}_0\right) \cdot \frac{\partial \tilde{f}}{\partial \mathbf{p}} - \hat{L}_C \tilde{f} = -e\left(\tilde{\mathbf{E}} + \frac{1}{c}\mathbf{v} \times \tilde{\mathbf{B}}\right) \cdot \frac{\partial f_0}{\partial \mathbf{p}}. \tag{112}$$

Here, f_0 is the equilibrium distribution function consistent with plasma and magnetic field equilibrium profiles including the toroidal plasma rotation (the poloidal rotation is assumed to be zero), Φ_0 is the equilibrium electrostatic potential with $\mathbf{E}_0 = -\nabla\Phi_0$. For the description of particle collisions (Coulomb interaction) we use an one-dimensional Fokker-Planck collision operator (Ornstein-Uhlenbeck approximation, see Ref. [35])

$$\hat{L}_c \tilde{f} = \frac{\partial}{\partial u_\parallel} D \left[\frac{\partial}{\partial u_\parallel} + \frac{u_\parallel - V_\parallel}{v_T^2}\right] \tilde{f}, \tag{113}$$

where $u_\parallel$ is a particle parallel velocity, D is a constant diffusion coefficient in velocity space, $v_T = \sqrt{T_0/m_0}$ is the thermal velocity, and $V_\parallel$ is a bulk parallel velocity of the given specii. Following the procedure outlined in Mahajan-Chen [23], Equation (112) is solved analytically in action-angle variables (Refs. [16, 20]).
The Hamiltonian form of Equation (112) can be written like

$$\frac{\partial f}{\partial t} + \{f, H\} = L_C f, \tag{114}$$

using Poisson brackets

$$\begin{aligned} \{a, b\} &= \frac{\partial a}{\partial \mathbf{r}} \cdot \frac{\partial b}{\partial \mathbf{p}} - \frac{\partial b}{\partial \mathbf{r}} \cdot \frac{\partial a}{\partial \mathbf{p}} = \\ &= \frac{\partial a}{\partial \boldsymbol{\Theta}} \cdot \frac{\partial b}{\partial \mathbf{J}} - \frac{\partial b}{\partial \boldsymbol{\Theta}} \cdot \frac{\partial a}{\partial \mathbf{J}}, \end{aligned} \tag{115}$$

which are valid for canonical transformations of coordinates. The canonical *action-angle* variables are $\boldsymbol{\Theta} = (\Theta^1, \Theta^2, \Theta^3)$ and $\mathbf{J} = (J_1, J_2, J_3)$ for *actions* $\mathbf{J} = \oint \mathbf{p}\mathrm{d}\mathbf{r}$, which are invariants.
A linearisation in sense of Equation (111) can be applied to the vector potential

in $\nabla \times \mathbf{A} = \mathbf{B}$, by $\mathbf{A} = \mathbf{A}_0 + \tilde{\mathbf{A}}$. Consequently, the scalar potential describing the electric field must be linearised by $\Phi = \Phi_0 + \tilde{\Phi}$. Using the radiation gauge

$$\tilde{\Phi} = 0, \tag{116}$$

one can express the linearised Hamiltonian like

$$H = \frac{1}{2m}\left(\mathbf{p} - \frac{e}{c}\mathbf{A}_0 - \frac{e}{c}\tilde{\mathbf{A}}\right)^2 + e\Phi_0 = H_0 + \tilde{H}, \tag{117}$$

what gives the unperturbed Hamiltonian as

$$H_0 = \frac{mv_0^2}{2} + e\Phi_0, \qquad \mathbf{v}_0 = \frac{1}{m}\left(\mathbf{p} - \frac{e}{c}\mathbf{A}_0\right), \tag{118}$$

with particle mass m.
The unperturbed part of the Hamiltonian can be expressed as a function of the *action* variable $\mathbf{J}$ only as $H_0 = H_0(\mathbf{J})$.
With the introduced *action-angle* variables, equations of unperturbed motion for a particle of species α can be written like

$$\dot{\Theta}^\alpha = \Omega^\alpha = \frac{\partial H_0(\mathbf{J})}{\partial J_\alpha}, \qquad \dot{J}_\alpha = -\frac{\partial H_0(\mathbf{J})}{\partial \Theta^\alpha} = 0. \tag{119}$$

The perturbation component of the Hamiltonian can be defined by means of the time dependence of the complex form

$$\tilde{H} = \mathrm{Re}\left(\overline{\mathbf{H}}\mathrm{e}^{-\mathrm{i}\omega t}\right), \qquad \tilde{A} = \mathrm{Re}\left(\overline{\mathbf{A}}\mathrm{e}^{-\mathrm{i}\omega t}\right). \tag{120}$$

The perturbed Hamiltonian can now be expressed by the use of the perurbation amplitudes $\overline{\mathbf{H}}$ and $\overline{\mathbf{A}}$ in temporal Fourier space like

$$\overline{\mathbf{H}} = -\frac{e}{c}\mathbf{v}_0 \cdot \overline{\mathbf{A}} = \frac{\mathrm{i}e}{\omega}v_0^k\tilde{E}_k = \frac{\mathrm{i}e}{\omega}\Omega^\alpha\mathcal{E}_\alpha, \tag{121}$$

using curvilinear coordinates $x^k = x_c^k(\mathbf{\Theta}, \mathbf{J})$ and corresponding (equilibrium) velocities v_0^k, which are in correlation to canonical frequencies $\Omega^\alpha = \Omega^\alpha(\mathbf{J})$ by

$$v_0^k = \frac{\partial x_c^k}{\partial \Theta^\alpha}\Omega^\alpha, \qquad \Omega^\alpha = \frac{\partial H_0}{\partial J_\alpha}. \tag{122}$$

The electric field components enter in covariant form as $\tilde{E}_k = \frac{\mathrm{i}\omega}{c}\tilde{A}_k$ which are transformed to canonical components by

$$\mathcal{E}_\alpha = \frac{\partial x_c^k}{\partial \Theta^\alpha}\tilde{E}_k. \tag{123}$$

During linearisation all contributions containing squared factors of perturbation quantities are ignored. The linearised kinetic equation then results as

$$\frac{\partial \tilde{f}}{\partial t} + \Omega^{\alpha} \frac{\partial \tilde{f}}{\partial \Theta^{\alpha}} + \dot{J}_{\alpha} \frac{\partial f_0}{\partial J_{\alpha}} = L_c \tilde{f}, \tag{124}$$

where attention has to be paid on $\dot{J}_{\alpha}$ which now in contrary to the equilibrium expression from Equation (119) forms a perturbed expression

$$\dot{J}_{\alpha} \frac{\partial f_0}{\partial J_{\alpha}} = \frac{\partial \overline{H}}{\partial \Theta^{\alpha}} \frac{\partial f_0}{\partial J_{\alpha}}, \quad \Rightarrow \quad \dot{J}_{\alpha} = \tilde{\mathbf{F}} \cdot \frac{\partial \mathbf{r}}{\partial \Theta^{\alpha}}, \tag{125}$$

with a perturbed Lorentz-force $\tilde{\mathbf{F}} = e\left(\tilde{\mathbf{E}} + \frac{1}{c}\mathbf{v} \times \tilde{\mathbf{B}}\right)$.
It is convenient to use the *angle* variables $\mathbf{\Theta}$ for expansion of all perturbation terms into Fourier series like

$$\tilde{f}\left(\mathbf{\Theta}, \mathbf{J}, t\right) = \sum_{\mathbf{m}} \tilde{f}_{\mathbf{m}}\left(\mathbf{J}, t\right) \mathrm{e}^{i\mathbf{m}\cdot\mathbf{\Theta}}, \tag{126}$$

with the Fourier expansion indices written in vector form $\mathbf{m}$. The transformation rule to Fourier space of angle variables is

$$\frac{\partial \tilde{f}}{\partial \Theta^{\alpha}} \;\rightarrow\; i m_{\alpha} \tilde{f}_{\mathbf{m}}. \tag{127}$$

The expansion from Equation (126) enables to express the linearised kinetic equation (Equation (124)) by Fourier amplitudes of the perturbed distribution function $\tilde{f}\left(\mathbf{J}, t\right)$ as

$$\frac{\partial \tilde{f}_{\mathbf{m}}}{\partial t} + i\mathbf{m} \cdot \mathbf{\Omega} \tilde{f}_{\mathbf{m}} - L_c \tilde{f}_{\mathbf{m}} = \tilde{Q}_{\mathbf{m}}, \tag{128}$$

where all sources of perturbations are contained in the source term $\tilde{Q}_{\mathbf{m}}$.
If the Coulomb collision operator from Equation (113) is applied to Equation (128), then results

$$i\left(\mathbf{m} \cdot \mathbf{\Omega} - \omega\right) \tilde{f}_{\mathbf{m}} - \frac{\partial}{\partial u_{\parallel}} D \left[\frac{\partial}{\partial u_{\parallel}} + \frac{u_{\parallel} - V_{\parallel}}{v_T^2}\right] \tilde{f}_{\mathbf{m}} = \tilde{Q}_{\mathbf{m}}. \tag{129}$$

In cylindrical symmetry $\mathbf{x} = (r, \vartheta, z)$ the parallel and perpendicular projections of each vector can be expressed by using

$$\mathbf{h} = \frac{\mathbf{B}_0}{B_0} \quad , \quad \mathbf{e}_{\perp} = \mathbf{h} \times \mathbf{e}_r. \tag{130}$$

It is useful to declare the velocity substitution

$$u = u_{\parallel} - V_{\parallel}. \tag{131}$$

Further the expressions for electric particle drift ω_{E} and parallel and perpendicular wave numbers $k_{\parallel}$, $k_{\perp}$, which are

$$\omega_{\mathrm{E}} = k_{\perp} V_{\mathrm{E}}, \quad k_{\parallel} = k_{\vartheta} h^{\vartheta} + k_z h^z, \quad k_{\perp} = \left(h_z k_{\vartheta} - h_{\vartheta} k_z\right)/r_0, \tag{132}$$

define

$$\mathbf{m} \cdot \mathbf{\Omega} = \omega_0 = k_{\parallel} V_{\parallel} + \omega_{\mathrm{E}} + l\omega_c, \tag{133}$$

where $\omega_c = \frac{eB}{mc}$ is the cyclotron frequency. With these substitutions, Equation (129) becomes

$$ik_{\parallel} u \tilde{f}_{\mathbf{m}} + i\omega_0 \tilde{f}_{\mathbf{m}} + \frac{\partial \tilde{f}_{\mathbf{m}}}{\partial t} - \frac{\partial}{\partial u} D \left[\frac{\partial}{\partial u} + \frac{u}{v_T^2}\right] \tilde{f}_{\mathbf{m}} = \tilde{Q}_{\mathbf{m}}. \tag{134}$$

Note that the expression is re-transformed by temporal Fourier transformation. To be able to solve Equation (134) it is convenient to transform it to a partial differential equation of first order. This can be achieved by Fourier transformation to velocity space of u using transformation

$$F_{\mathbf{m}}(k,t) = \int_{-\infty}^{\infty} \mathrm{d}u \; e^{-iku} \; \tilde{f}_{\mathbf{m}}(u,t), \tag{135}$$

and k is the wave number in velocity space. The kinetic equation in velocity space of the introduced velocity variable u then results as a partial differential equation of first order

$$\frac{\partial F_{\mathbf{m}}(k,t)}{\partial t} + \left(i\omega_o + Dk^2\right) F_{\mathbf{m}}(k,t) + \frac{\partial}{\partial k}\left(k\nu - k_{\parallel}\right) F_{\mathbf{m}}(k,t) = Q_{\mathbf{m}}(k,t), \tag{136}$$

with collision frequency $\nu = \frac{D}{v_{\mathrm{T}}^2}$. It is possible to solve Equation (136) by the characteristics method to obtain the solution for the perturbed distribution function in Fourier space in *angle* variables as

$$\tilde{f}_{\mathbf{m}}(u,t) = \int_0^{t-t_0} \mathrm{d}\tau \int_{-\infty}^{\infty} \mathrm{d}u' G(u,u',\tau)\, \tilde{Q}_{\mathbf{m}}(u', t-\tau), \tag{137}$$

and Green's function

$$G(u,u',\tau) = \frac{1}{\sqrt{4\pi a}} \; \exp\left[\frac{ik}{\nu}(u-u') - c - \frac{1}{4a}\left(u - u'\mathrm{e}^{-\nu\tau} + ib\right)^2\right], \tag{138}$$

with characteristics

$$\begin{aligned} a(\tau) &= \frac{v_T^2}{2}\left(1-\mathrm{e}^{-2\nu\tau}\right), \\ b(\tau) &= \frac{2k_\parallel v_T^2}{\nu}\left(1-\mathrm{e}^{-2\nu\tau}\right), \\ c(\tau) &= \left(i\omega_0+\frac{k_\parallel^2 v_T^2}{\nu}\right)\tau. \end{aligned} \tag{139}$$

The solution of the perturbed distribution function from Equation (137) can then enter the components of the perturbation of the current density

$$\tilde{j}^k(\mathbf{x},t) = e\int \mathrm{d}^3p_0 v^k \tilde{f} = \frac{e}{\sqrt{g}}\int \mathrm{d}^3\theta \int \mathrm{d}^3J\delta\left[\mathbf{x}-\mathbf{x}_c(\mathbf{J},\mathbf{\Theta})\right]\times \\ \times v^k(\mathbf{J},\mathbf{\Theta})\,\tilde{f}(\mathbf{J},\mathbf{\Theta},t), \tag{140}$$

where $g = r^2$ is the determinant of the metric tensor for transformations to cylindrical coordinates. The δ function leads to the integral over the generalised coordinate u'. This is necessary, because the canonical transformation is only valid for the whole phase space.

4 Maxwell Equations in Vacuum and Resistive Wall Regions

To be able to model the cylindric plasma configuration with all its different regions namely the plasma zone, the vacuum region and the resistive wall region, the model equations for all regions must be available. This imposes that the plasma model must be solved for each region separately. This chapter describes the solutions of Maxwell equations and the plasma model from Sec. 3.1 in different zones of the cylinder, shows their derivations and gives a discussion of electric and magnetic fields in each region.

4.1 Solution for a Resistive Medium

Modelling the resistive wall region requires the inclusion of a characteristic medium property to the equilibrium Maxwell equations. This need can be fulfilled by the electric conductivity σ which is inverse proportional to the resistivity of the medium $\sigma \propto \eta^{-1}$. For this purpose the Maxwell equations from Equation (21) and Equation (20) are written like

$$\nabla \times \mathbf{E} = \frac{i\omega}{c}\mathbf{B}, \tag{141}$$

$$\nabla \times \mathbf{B} = \frac{4\pi}{c}\,\mathbf{j} - \frac{i\omega}{c}\mathbf{E}. \tag{142}$$

Both equations are already Fourier transformed in time, i.e.$\frac{\partial}{\partial t} \rightarrow -i\omega$. In Equation (20) the term containing the electric field $\frac{1}{c}\frac{\partial \mathbf{E}}{\partial t}$ must be added to the right hand side because the electric field is assumed to be time dependent.
Further the scalar form of Ohm's law

$$\mathbf{j} = \sigma \mathbf{E}\ , \tag{143}$$

enters the conductivity to Equation (142). Effects of resistivity represent a decay of field amplitudes and are usually expressed by imaginary parts of frequencies. In the case of conductivity this can be done like

$$\omega^* = \omega + i\nu, \tag{144}$$

$$\nu = 4\pi\sigma. \tag{145}$$

Then Equation (142) changes to

$$\nabla \times \mathbf{B} = \frac{4\pi}{c}\frac{\nu}{4\pi}\mathbf{E} - \frac{i\omega}{c}\mathbf{E} = -\frac{i\omega^*}{c}\mathbf{E}. \tag{146}$$

The curls in Equation (141) and Equation (146) must be expressed in cylindrical symmetry by Fourier components.

For $\nabla \times \mathbf{E}$:

$$\frac{im}{r}E_z - ikE_\theta = \frac{i\omega}{c}B_r, \tag{147}$$

$$ikE_r - E_z' = \frac{i\omega}{c}B_\theta, \tag{148}$$

$$\frac{1}{r}(rE_\theta)' - \frac{im}{c}E_r = \frac{i\omega}{c}B_z, \tag{149}$$

$\nabla \times \mathbf{B}$:

$$\frac{im}{r}B_z - ikB_\theta = -\frac{i\omega^*}{c}E_r, \tag{150}$$

$$ikB_r - B_z' = -\frac{i\omega^*}{c}E_\theta, \tag{151}$$

$$\frac{1}{r}(rB_\theta)' - \frac{im}{r}B_r = -\frac{i\omega^*}{c}E_z. \tag{152}$$

The prime marks the radial derivative, m is the toroidal mode numer and k is the z-component of the wave number.
The radial components can be substituted into the Θ- and z-components what leads to

$$E_z' = \left(\frac{ik^2c}{\omega^*} - \frac{i\omega}{c}\right)B_\theta - \frac{ikmc}{\omega^* r}B_z, \tag{153}$$

$$\frac{1}{r}(rE_\theta)' = \left(\frac{i\omega}{c} - \frac{im^2c}{\omega^* r^2}\right)B_z + \frac{imkc}{\omega^* r}B_\theta, \tag{154}$$

$$B_z' = \frac{ikmc}{\omega r}E_z + \left(\frac{i\omega^*}{c} - \frac{ik^2c}{\omega}\right)E_\theta, \tag{155}$$

$$\frac{1}{r}(rB_\theta)' = \left(\frac{im^2c}{\omega r^2} - \frac{i\omega^*}{c}\right)E_z + \frac{imkc}{\omega r}E_\theta. \tag{156}$$

In these system of partial differential equations of first order, it is possible to consider two different cases. The *transversal electric mode* **TE** and the *transversal magnetic mode* **TM**.

4.2 TM-Mode

For the *transverse magnetic* mode the z-component of the magnetic field is set to zero, $B_z = 0$, what results in the remaining field components of both fields

$$E_r = -\frac{ik}{(\alpha^*)^2} E_z', \qquad B_r = -\frac{m\omega^*}{(\alpha^*)^2 rc} E_z, \tag{157}$$

$$E_\theta = \frac{mk}{(\alpha^*)^2 r} E_z, \qquad B_\theta = -\frac{i\omega^*}{(\alpha^*)^2 c} E_z'. \tag{158}$$

Here α^* contains the frequency ω^* in the following way

$$(\alpha^*)^2 := k^2 - \frac{\omega\omega^*}{c^2}. \tag{159}$$

The field components of Equation (157) and Equation (158) are all determined by E_z. If E_z is known, then all other field components are known immediately. Equation (152) can be written in terms of E_z by use of Equation (157) and Equation (158). The result can be written in form of a Bessel equation:

$$r^2 E_z'' + r E_z' - \left(m^2 + (\alpha^*)^2 r^2\right) E_z = 0. \tag{160}$$

The solution of Equation (160) consists of a linear combination of modified Bessel functions I_m and K_m,

$$E_z = C_1 I_m(\alpha^* r) + C_2 K_m(\alpha^* r). \tag{161}$$

here C_1 and C_2 are constants.

4.3 TE-Mode

For the *transverse electric* mode the z-component of the electric field is set to zero, $E_z = 0$. Again this condition is put into Equations (153) to (156). The r- and θ-components of both fields then remain

$$E_r = \frac{\omega m}{(\alpha^*)^2 rc} B_z, \qquad B_r = -\frac{ik}{(\alpha^*)^2} B_z', \tag{162}$$

$$E_\theta = \frac{i\omega}{(\alpha^*)^2 c} B_z', \qquad B_\theta = \frac{km}{(\alpha^*)^2 r} B_z, \tag{163}$$

as expressions of only B_z. After a substitution of these components a similar procedure like for the TM-mode is applied what finally results in a Bessel differential equation for B_z:

$$r^2 B_z'' + r B_z' - \left(m^2 + (\alpha^*)^2 r^2\right) B_z = 0. \tag{164}$$

Like for the TM case, the solution of Equation (164) consists of a linear combination of the modified Bessel functions I_m and K_m:

$$B_z = D_1 I_m(\alpha^* r) + D_2 K_m(\alpha^* r), \tag{165}$$

with constants D_1 and D_2.

4.4 Vacuum Solution with Antenna and Resistive Wall

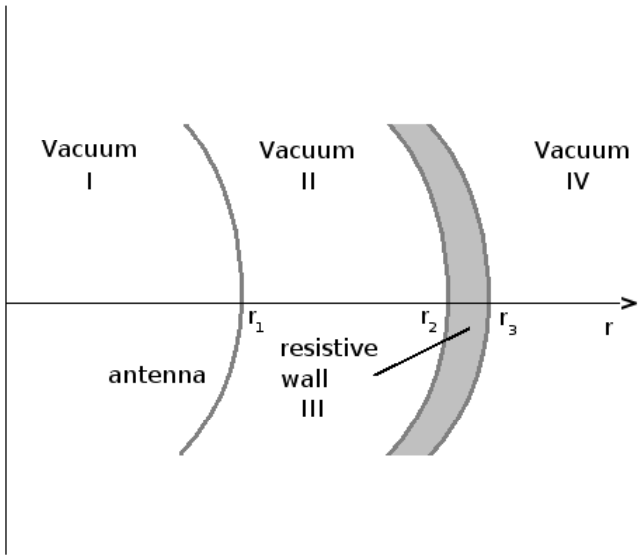

Figure 9: The antenna and the resistive wall in the cylinder are surrounded by vacuum regions. The cylinder is radially splitted into four different regions. The antenna is located at r_1, the inner surface of the resistive wall at r_2 and the outer surface at $r_3 = r_2 + d$, where d is the thickness of the resistive wall.

In each region, the general solution of magnetic and electric fields must be known. At presence of the TM- and the TE-mode, both contributions must be included to the total solution by superposition like

$$\mathbf{E} = \mathbf{E}^{TM} + \mathbf{E}^{TE}, \tag{166}$$

$$\mathbf{B} = \mathbf{B}^{TM} + \mathbf{B}^{TE}. \tag{167}$$

Let us first consider a cylinder with vacuum, antenna and a resistive wall like shown in Figure 9. This is a very simple configuration which shows the behaviour of fields in vacuum and resistive media very good. The antenna divides the inner vacuum in region I and region II at r_1. The resistive wall has a finite thickness and is placed between r_2 and r_3 (region III), outside r_3 a vacuum in region IV spreads to infinity. All field components of magnetic and electric fields are computed inside each region separately. By the superposition rule in Equation (166) and Equation (167), where the corresponding field components from Sec. 4.3 and Sec. 4.2 must be substituted, all regions can be modelled in the same way.

Region I:

$$E_r^I = -\frac{ik}{\alpha^2} C_1 I_m'(\alpha r) + \frac{\omega m}{\alpha^2 r c} D_1 I_m(\alpha r), \tag{168}$$

$$E_\theta^I = \frac{mk}{\alpha^2 r} C_1 I_m(\alpha r) + \frac{i\omega}{\alpha^2 c} D_1 I_m'(\alpha r), \tag{169}$$

$$E_z^I = C_1 I_m(\alpha r), \tag{170}$$

$$B_r^I = -\frac{m\omega}{\alpha^2 r c} C_1 I_m(\alpha r) - \frac{ik}{\alpha^2} D_1 I_m'(\alpha r), \tag{171}$$

$$B_\theta^I = -\frac{i\omega}{\alpha^2 c} C_1 I_m'(\alpha r) + \frac{km}{\alpha^2 r} D_1 I_m(\alpha r), \tag{172}$$

$$B_z^I = D_1 I_m(\alpha r). \tag{173}$$

One has to consider the cylindric geometry and the behaviour of Bessel functions at cylinder axis $r = 0$. Modified Bessel functions of second order K_m grow to infinity for $r \to 0$. To exclude these diverging contributions from solutions in Region I, the terms containing K_m are set to zero what guarantees a nonsingular solution of field components at the cylinder axis.
In regions II and III both modified Bessel functions are present, whereas ω^* and α^* occur only in the medium description of region III, elsewhere $\sigma = 0$ and $\omega^* = \omega$ and $\alpha^* = \alpha$. In region IV functions I_m are excluded due to their diverging behaviour for $r \to \infty$.
A set of 12 coefficients $(C_1, C_3, C_4, C_5, C_6, C_7)$ and $(D_1, D_3, D_4, D_5, D_6, D_7)$ arises from the field descriptions of the different regions in Equations (168) to (191).

Region II:

$$E_r^{II} = -\frac{ik}{\alpha^2}\left[C_3 I_m'(\alpha r) + C_4 K_m'(\alpha r)\right] + \frac{\omega m}{\alpha^2 rc}\left[D_3 I_m(\alpha r) + D_4 K_m(\alpha r)\right], \quad (174)$$

$$E_\theta^{II} = \frac{mk}{\alpha^2 r}\left[C_3 I_m(\alpha r) + C_4 K_m(\alpha r)\right] + \frac{i\omega}{\alpha^2 c}\left[D_3 I_m'(\alpha r) + D_4 K_m'(\alpha r)\right], \quad (175)$$

$$E_z^{II} = C_3 I_m(\alpha r) + C_4 K_m(\alpha r), \quad (176)$$

$$B_r^{II} = -\frac{m\omega}{\alpha^2 rc}\left[C_3 I_m(\alpha r) + C_4 K_m(\alpha r)\right] - \frac{ik}{\alpha^2}\left[D_3 I_m'(\alpha r) + D_4 K_m'(\alpha r)\right], \quad (177)$$

$$B_\theta^{II} = -\frac{i\omega}{\alpha^2 c}\left[C_3 I_m'(\alpha r) + C_4 K_m'(\alpha r)\right] + \frac{km}{\alpha^2 r}\left[D_3 I_m(\alpha r) + D_4 K_m(\alpha r)\right], \quad (178)$$

$$B_z^{II} = D_3 I_m(\alpha r) + D_4 K_m(\alpha r). \quad (179)$$

Region III:

$$E_r^{III} = -\frac{ik}{(\alpha^*)^2}\left[C_5 I_m'(\alpha^* r) + C_6 K_m'(\alpha^* r)\right] + \frac{\omega m}{(\alpha^*)^2 rc}\left[D_5 I_m(\alpha^* r) + D_6 K_m(\alpha^* r)\right], \quad (180)$$

$$E_\theta^{III} = \frac{mk}{(\alpha^*)^2 r}\left[C_5 I_m(\alpha^* r) + C_6 K_m(\alpha^* r)\right] + \frac{i\omega}{(\alpha^*)^2 c}\left[D_5 I_m'(\alpha^* r) + D_6 K_m'(\alpha^* r)\right], \quad (181)$$

$$E_z^{III} = C_5 I_m(\alpha^* r) + C_6 K_m(\alpha^* r), \quad (182)$$

$$B_r^{III} = -\frac{m\omega^*}{(\alpha^*)^2 rc}\left[C_5 I_m(\alpha^* r) + C_6 K_m(\alpha^* r)\right] - \frac{ik}{(\alpha^*)^2}\left[D_5 I_m'(\alpha^* r) + D_6 K_m'(\alpha^* r)\right], \quad (183)$$

$$B_\theta^{III} = -\frac{i\omega^*}{(\alpha^*)^2 c}\left[C_5 I_m'(\alpha^* r) + C_6 K_m'(\alpha^* r)\right] + \frac{km}{(\alpha^*)^2 r}\left[D_5 I_m(\alpha^* r) + D_6 K_m(\alpha^* r)\right], \quad (184)$$

$$B_z^{III} = D_5 I_m(\alpha^* r) + D_6 K_m(\alpha^* r). \quad (185)$$

Region IV:

$$E_r^{IV} = -\frac{ik}{\alpha^2} C_7 K'_m(\alpha r) + \frac{\omega m}{\alpha^2 rc} D_7 K_m(\alpha r), \tag{186}$$

$$E_\theta^{IV} = \frac{mk}{(\alpha^*)^2 r}\left[C_5 I_m(\alpha^* r) + C_6 K_m(\alpha^* r)\right] + \frac{i\omega}{(\alpha^*)^2 c}\left[D_5 I'_m(\alpha^* r) + D_6 K'_m(\alpha^* r)\right], \tag{187}$$

$$E_z^{IV} = C_7 K_m(\alpha r), \tag{188}$$

$$B_r^{IV} = -\frac{m\omega}{\alpha^2 rc} C_7 K_m(\alpha r) - \frac{ik}{\alpha^2} D_7 K'_m(\alpha r), \tag{189}$$

$$B_\theta^{IV} = -\frac{i\omega}{\alpha^2 c} C_7 K'_m(\alpha r) + \frac{km}{\alpha^2 r} D_7 K_m(\alpha r), \tag{190}$$

$$B_z^{IV} = D_7 K_m(\alpha r). \tag{191}$$

4.5 Application of Boundary Conditions

In the previous section it is described how the field components in the four cylinder regions yield a set of 12 coefficients. To determine these coefficients, a linear inhomogeneous system of equations must be solved,

$$\mathbf{A} \cdot \mathbf{c} = \mathbf{b}, \tag{192}$$

which results from 12 boundary conditions at zone interfaces. Vector $\mathbf{c}$ contains the ceofficients, $\mathbf{A}$ is a 12x12-matrix and $\mathbf{b}$ is a vector containing the boundary conditions. The boundary conditions result from continuity conditions of the electric and magnetic field at vacuum and medium interfaces and jumps of fields at the antenna.
At the antenna

$$[\mathbf{n} \times \mathbf{E}] = 0, \tag{193}$$

$$[\mathbf{n} \times \mathbf{B}] = \frac{4\pi}{c}\mathbf{j}, \tag{194}$$

a surface current density $\mathbf{j}$ produces a jump of the tangential $\mathbf{B}$-components

$$[B_\theta]_{r_a} = \frac{4\pi}{c} j_z, \tag{195}$$

$$[B_z]_{r_a} = -\frac{4\pi}{c} j_\theta, \tag{196}$$

while the tangential components are continuous

$$[E_\theta]_{r_a} = 0, \tag{197}$$
$$[E_z]_{r_a} = 0. \tag{198}$$

Here the bracket operator represents the difference of quantity values x across the boundary between region i and j at position $r = y$ like:

$$[x]_y = x^i - x^j. \tag{199}$$

At the resistive wall, the magnetic field has no jump and all tangential components are continuous

$$[B_{\theta,z}]_{r_w} = 0, \qquad [B_{\theta,z}]_{r_w+d} = 0, \tag{200}$$
$$[E_{\theta,z}]_{r_w} = 0, \qquad [E_{\theta,z}]_{r_w+d} = 0, \tag{201}$$

there r_a is the antenna position, r_w is the resistive wall position and d is the resistive wall thickness.
From these 12 boundary equations, matrix $\mathbf{A}$ of the linear inhomogeneous system results with

$$\begin{bmatrix}
tI_1' & -s_1I_1 & -tI_1' & -tK_1' & s_1I_1 & s_1K_1 & 0 & 0 & 0 & 0 & 0 & 0 \\
0 & -I_1 & 0 & 0 & I_1 & K_1 & 0 & 0 & 0 & 0 & 0 & 0 \\
-s_1I_1 & -tI_1' & s_1I_1 & s_1K_1 & tI_1' & tK_1' & 0 & 0 & 0 & 0 & 0 & 0 \\
-I_1 & 0 & I_1 & K_1 & 0 & 0 & 0 & 0 & 0 & 0 & 0 & 0 \\
0 & 0 & tI_2' & tK_2' & -s_2I_2 & -s_2K_2 & -p^*I_2^{*\prime} & -p^*K_2^{*\prime} & s_2^*I_2^* & s_2^*K_2^* & 0 & 0 \\
0 & 0 & 0 & 0 & -I_2 & -K_2 & 0 & 0 & I_2^* & K_2^* & 0 & 0 \\
0 & 0 & -s_2I_2 & -s_2K_2 & -tI_2' & -tK_2' & s_2^*I_2^* & s_2^*K_2^* & t^*I_2^{*\prime} & t^*K_2^{*\prime} & 0 & 0 \\
0 & 0 & -I_2 & -K_2 & 0 & 0 & I_2^* & K_2^* & 0 & 0 & 0 & 0 \\
0 & 0 & 0 & 0 & 0 & 0 & p^*I_3^{*\prime} & p^*K_3^{*\prime} & -s_3^*I_3^* & -s_3^*K_3^* & -tK_3' & s_3K_3 \\
0 & 0 & 0 & 0 & 0 & 0 & 0 & 0 & -I_3^* & -K_3^* & 0 & K_3 \\
0 & 0 & 0 & 0 & 0 & 0 & -s_3^*I_3^* & -s_3^*K_3^* & -t^*I_3^{*\prime} & -t^*K_3^{*\prime} & s_3K_3 & tK_3' \\
0 & 0 & 0 & 0 & 0 & 0 & -I_3^* & -K_3^* & 0 & 0 & K_3 & 0
\end{bmatrix}. \tag{202}$$

Vector **b** contains the continuity and jump conditions mentioned above,

$$b_1 = \frac{4\pi}{c} j_z \ , \ b_2 = -\frac{4\pi}{c} j_\theta, \tag{203}$$

$$b_3 = b_4 = b_5 = b_6 = b_7 = b_8 = b_9 = b_{10} = b_{11} = b_{12} = 0 \ . \tag{204}$$

Matrix **A** contains the abbreviations

$$t = \frac{i\omega}{\alpha^2 c}, \quad t^* = \frac{i\omega}{(\alpha^*)^2 c}, \quad p^* = \frac{i\omega^*}{(\alpha^*)^2 c}, \tag{205}$$

$$r_1 = r_a, \qquad r_2 = r_w, \qquad r_3 = r_w + d, \tag{206}$$

r_1 is the antenna position, r_2 the position of the inner resistive wall surface and r_3 the position of the outer resistive wall surface. Further

$$I_i = I_m(\alpha r_i), \qquad I_i^* = I_m(\alpha^* r_i), \tag{207}$$

$$K_i = K_m(\alpha r_i), \qquad K_i^* = K_m(\alpha^* r_i), \tag{208}$$

$$s_i = \frac{mk}{\alpha^2 r_i}, \qquad s_i^* = \frac{mk}{(\alpha^*)^2 r_i}, \tag{209}$$

all for $i = 1, 2, 3$.

4.6 Computation of the Vacuum Field Components

The computation of vacuum field components from Sec. 4.4 is done by MATLAB, where a linear inhomogeneous system from Equation (192) is solved.
The complex amplitudes of the magnetic and electric fields are evaluated over all four regions of the cylinder like shown in Figure 9. The computation is done for a resonant mode (m,n)=(12,4) with a frequency of $f = \frac{\omega}{2\pi} = 1\text{kHz}$. The antenna is placed at $r_1 = 53\text{cm}$ and the resistive wall at $r_2 = 60\text{cm}$ with a thickness of $d = 3\text{cm}$. The torus radius is $R = 175\text{cm}$ and the applied antenna current is $I_0 = 15\text{kA} = 4.5 \cdot 10^{13}\text{statamp}$. The tangential components of the current density in the antenna are chosen to be

$$j_\theta = -\frac{8I_0}{3\pi R} = -2.182 \cdot 10^{11} \ \frac{\text{statamp}}{\text{cm}^2}, \tag{210}$$

$$j_z = -j_\theta \frac{mR}{nr_1} = 2.162 \cdot 10^{12} \ \frac{\text{statamp}}{\text{cm}^2} \ . \tag{211}$$

The ratio between the skin depth and wall thickness $\frac{\delta}{d}$ with

$$\delta = \frac{c}{\sqrt{\omega 2\pi\sigma}} \tag{212}$$

is a function of the conductivity σ and can be expressed in terms of $\nu = 4\pi\sigma$

$$\delta = \frac{c}{\sqrt{\omega\frac{\nu}{2}}} \ . \tag{213}$$

$\Rightarrow$ high conductivity σ means a small skin depth δ.
Figure 10 and Figure 11 show all non-vanishing electric and magnetic field components in all regions I - IV. To test the influence of the resistive wall, two different conductivities are applied:

- $\frac{\delta}{d} << 1$ is achieved by a high conducting wall with $\frac{\nu}{\omega} = 10^{15}$ and a small skin depth $\delta = 0.214$cm. Such a wall has a visible effect on the field components, like shown in Figure 10.
- $\frac{\delta}{d} >> 1$, represents a high resistive wall, where the fields are not shielded inside it. At $\frac{\nu}{\omega} = 0.1$ the conductivity is very low. The corresponding skin depth is $\delta = 2.1 \cdot 10^7$cm. Figure 11 shows that such a wall behaves like a vacuum region.

The real part of the radial electric field is the component which is most sensitive on changes of the resistive wall properties.
Figure 12 compares the real part of the radial electric field on changes in conductivity (change of $\frac{\nu}{\omega}$) and changes of wall thickness d. The jump of $\mathrm{Re}(E_r)$ at the resistive wall is larger in case of a thinner wall.

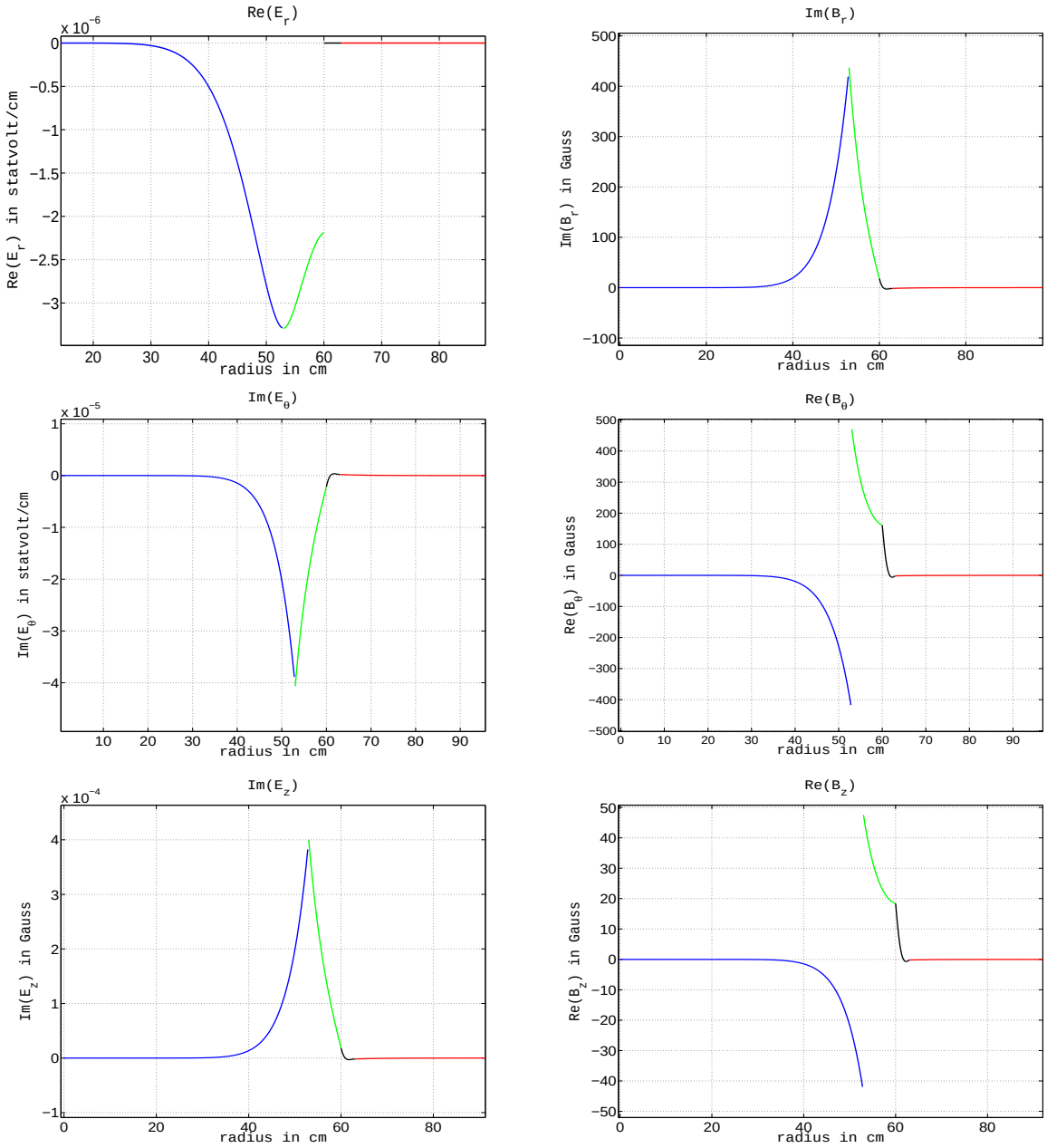

Figure 10: Components of the electric and magnetic field plotted over r: *blue*: vacuum region I, *green*: vacuum region II, *black*: resistive wall region III, *red*: vacuum region IV. $f = \frac{\omega}{2\pi} = 1\text{kHz}$, resonant mode $(m, n) = (12, 4)$ with wall thickness $d = 3\text{cm}$ and antenna current $I_0 = 15\text{kA}$. High conducting wall with $\frac{\nu}{\omega} = 10^{15}$ and a skin depth $\delta = 0.214\text{cm}$. The antenna position is $r_a = 53\text{cm}$ and the resistive wall at $r_w = 60\text{cm}$.

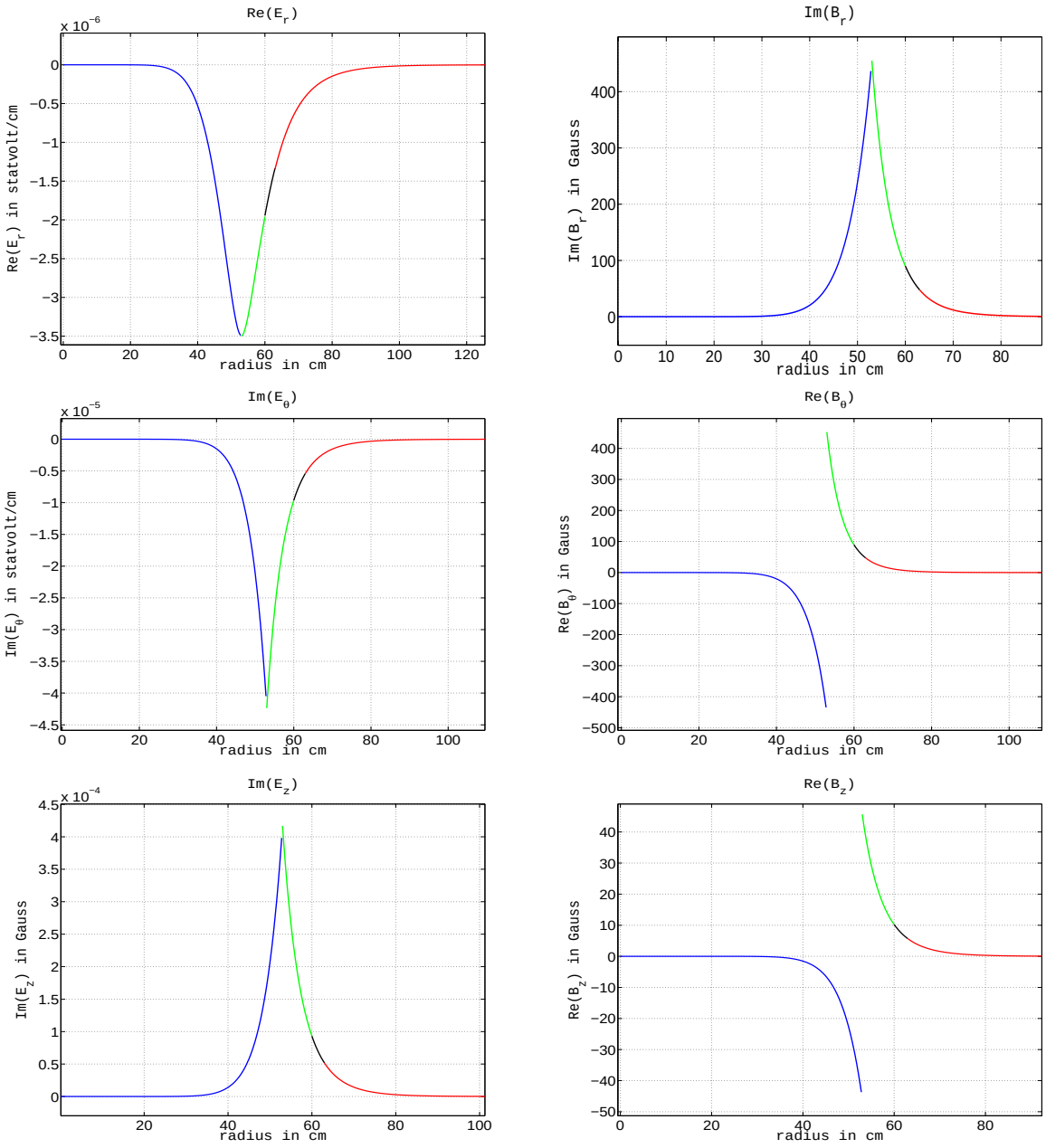

Figure 11: Components of the electric and magnetic field plotted over r: *blue*: vacuum region I, *green*: vacuum region II, *black*: resistive wall region III, *red*: vacuum region IV. $f = \frac{\omega}{2\pi} = 1\text{kHz}$, resonant mode $(m, n) = (12, 4)$ with wall thickness $d = 3\text{cm}$ and antenna current $I_0 = 15\text{kA}$. High resistive wall with $\frac{\nu}{\omega} = 0.1$ and a skin depth $\delta = 2.1 \cdot 10^7\text{cm}$, antenna position $r_a = 53\text{cm}$ and the resistive wall at $r_w = 60\text{cm}$.

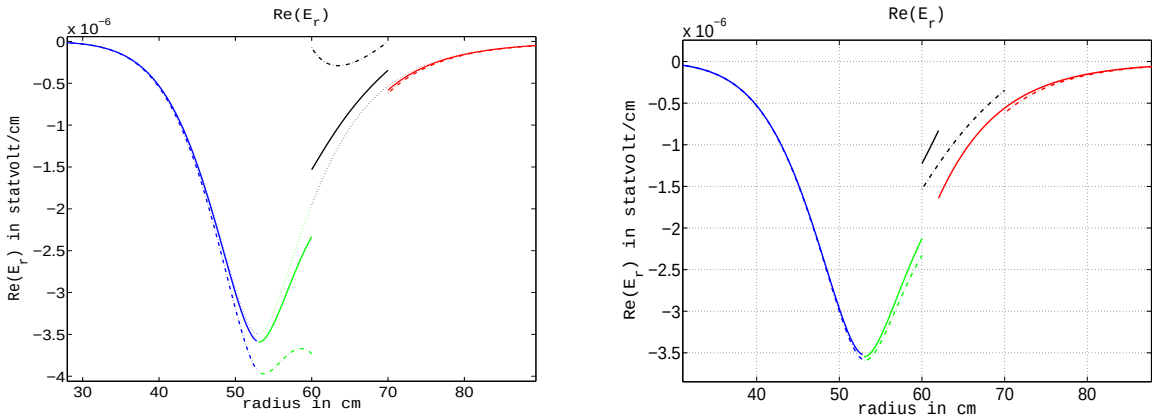

Figure 12: *left*: Real part of the radial electric field over r for three different wall conductivity cases $\frac{\nu}{\omega} = 0.1$ (dotted), $\frac{\nu}{\omega} = 1$ (solid) $\frac{\nu}{\omega} = 10$ (dash-dotted) with $d = 3$cm. *right*: Real part of the radial electric field over r for two different wall thicknesses $d = 2$cm (dash-dotted) and $d = 10$cm (solid) with $\frac{\nu}{\omega} = 1$. For all cases $f = \frac{\omega}{2\pi} = 1$kHz, mode numbers $m = 12$, $n = 4$, $I_0 = 15$kA, antenna position at $r_a = 53$cm and the resistive wall at $r_w = 60$cm are used.

5 MHD Instabilities

Magnetically confined plasmas face a big variety of conditions which can make the plasma configuration unstable, lead to strong disruptions of energy or to a shut down of the fusion process. Instabilities can arise from errors in MHD equilibrium profiles, particle transport barriers or simply by unfavourable energy distributions driven by current or pressure gradients (Ref. [15]).
From the technical point of view, the role of MHD instabilities is twofold. On one hand a turbulent plasma motion can be used for heating, external error fields can couple to internal fields to open transport barriers and avoid disruptions. On the other hand an uncontrolled disruption harms the material components of the fusion device and even the fusion process itself can be stopped (Refs. [15,18]). MHD instabilities set operational limits for fusion devices. The most important are plasma current, pressure, pressure gradient and density. Mitigation and control of instabilities are therefore very important topics in fusion research. The point of interest lies in the availability of a model which handles MHD instabilities. For this purpose it is useful to neglect the plasma resistivity and consider an ideal MHD description.
The following sections discuss the properties of the main ideal MHD instabilities and give a commonly used approach to handle them.

5.1 The Energy Principle

The energy principle is a concept which is used to determine whether a perturbation of a system is stable or unstable (if the system returns back to equilibrium or not). The energy principle is based on the change in potential energy of the system caused by the perturbation. It assumes that the MHD model conserves the total energy of the system (plasma configuration) completely,(see Ref. [11]). For a change in potential energy δW it holds that the perturbation for

$$\delta W > 0, \quad \text{is stable,} \tag{214}$$

$$\delta W < 0, \quad \text{is unstable.} \tag{215}$$

A perturbation force $\boldsymbol{\mathcal{F}}$ causes a displacement $\boldsymbol{\xi}$ and the change in potential energy can be defined like

$$\delta W = -\frac{1}{2}\int \boldsymbol{\xi}\cdot\boldsymbol{\mathcal{F}}\,\mathrm{d}V, \tag{216}$$

as integral over the volume V (Ref. [38]). The linearised MHD Equation (38) determines

$$\boldsymbol{\mathcal{F}} = \frac{1}{c}\mathbf{j}_1\times\mathbf{B}_0 + \frac{1}{c}\mathbf{j}_0\times\mathbf{B}_1 - \nabla p_1, \tag{217}$$

and by means of remaining perturbation quantities p_1, $\mathbf{B}_1$ and $\mathbf{j}_1$ from Equation (47), Equation (48) and Equation (49), the energy contribution results in

$$\delta W = -\frac{1}{2}\int \Big[\boldsymbol{\xi}\cdot\nabla\left(\gamma p_0\nabla\cdot\boldsymbol{\xi} + \boldsymbol{\xi}\cdot\nabla p_0\right) + \\ + \frac{1}{4\pi}\boldsymbol{\xi}\cdot\left(\left(\nabla\times\nabla\times\left(\boldsymbol{\xi}\times\mathbf{B}_0\right)\right)\times\mathbf{B}_0 + \left(\nabla\times\mathbf{B}_0\right)\times\nabla\times\left(\boldsymbol{\xi}\times\mathbf{B}_0\right)\right)\Big]\,\mathrm{d}V. \tag{218}$$

Using the Gauss integral relation

$$\int \nabla\cdot\mathbf{A}\,\mathrm{d}V = \int \mathbf{A}\cdot\mathrm{d}\mathbf{S}, \tag{219}$$

where the volume integral over a vector field $\mathbf{A}$ is replaced by a surface integral, the energy contribution can be written as

$$\delta W = \frac{1}{2}\int\left[\gamma p_0\left(\nabla\cdot\boldsymbol{\xi}\right)^2 + \left(\boldsymbol{\xi}\cdot\nabla p_0\right)\nabla\cdot\boldsymbol{\xi} + \frac{1}{4\pi}B_1^2 - \frac{1}{c}\mathbf{j}_0\cdot\left(\mathbf{B}_1\times\boldsymbol{\xi}\right)\right]\mathrm{d}V + \\ + \frac{1}{2}\int\left(p_1 + \frac{\mathbf{B}_0\cdot\mathbf{B}_1}{4\pi}\right)\boldsymbol{\xi}\cdot\mathrm{d}\mathbf{S}. \tag{220}$$

From these equations it is evident that δW is determined by $\boldsymbol{\xi}$.

5.2 Ideal MHD Instability

The gradients of the plasma current and pressure are the driving forces of MHD instabilities. Ideal modes assume that the plasma has no resistivity. Since this is not valid in reallity, it must be noted that ideal MHD is an useful tool to predict the occurence of instability, which will occur also for resistive cases, if ideal MHD predicts it, but due to the resistivity it will not be possible to model it exactly (Ref. [38]).
In general the modes can be separated (like e.g. in Ref. [11]) in:

- **Internal modes**:
  It is assumed that a plasma is surrounded by vacuum. It turned out that some instabilities do not change the position of the plasma-vacuum interface. Such modes have a resonant surface $m - qn = 0$ inside the plasma and are called *internal modes* with the boundary condition at plasma surface $\mathbf{n} \cdot \boldsymbol{\xi}|_S = 0$. Here $\mathbf{n}$ is the normal vector pointing outward of the plasma. (m, n) are toroidal and poloidal mode numbers.

- **External modes**:
  Modes which move the plasma-vacuum interface away from its equilibrium position have a resonant surface $m - qn = 0$ outside the plasma and are called *external modes* with the boundary condition at plasma surface $\mathbf{n} \cdot \boldsymbol{\xi}|_S \neq 0$.

Additionally to the separation in external and internal modes, instabilities can be classified as:

- **Pressure driven instability**:
  Modes driven by the pressure gradient are most unstable if they are internal (Ref. [11]). It is convenient to specify two classes:

  - **Interchange instabilities**:
    An unfavourable curvature of the magnetic field lines can lead to instability. Because of the plasma pressure exerting force radially outward, a force contribution from magnetic fields is stabilising for convex field lines and destabilising for concave field lines (relatively to the plasma interior). For the latter case, the field line curvature produces magnetic tension to shorten the field lines and pushes them to collapse inward. If two radially adjacent magnetic flux tubes are interchanged by perturbation in such way, the interchange is unstable. So systems with field lines concave to the plasma are unstable

to interchange perturbations. These instabilities can be influenced by the shear between two flux tubes.

- **Ballooning instabilities**:
  These modes represent a limit for the highest β which is possible in a fusion device. Inside the plasma both possibilities of field line curvatures do coexist. So if a perturbation changes along the field lines, it destabilises regions with unfavorable curvature and stabilises the other ones. The only possibility of stabilisation is to lower β.

- **Current driven instability**:
  Modes which are driven by the parallel current density $j_{\parallel}$ can be either internal or external and are often named *kink modes* because such perturbations kink the plasma surface into a helix, like shown in Figure 13. External kinks are significantly stronger than internal kinks. Kinks can

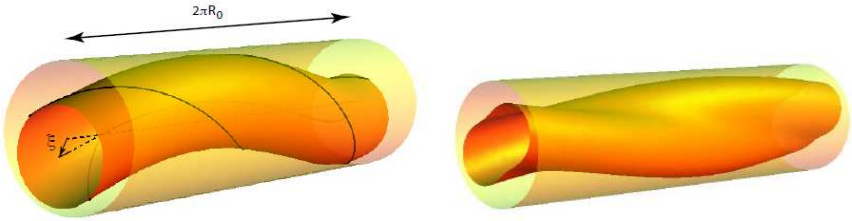

Figure 13: Kinking of a magnetic flux tube by a current driven kink instability in cylindrical symmetry. Shown are kink mechanisms for $m = 1$ (left plot) and $m = 2$ (right plot).

be stabilised by a perfectly conducting wall which is positioned close to the plasma surface.

5.3 Self-Adjointness of the Force Operator $\mathbf{F}(\boldsymbol{\xi})$

The force operator $\mathbf{F}(\boldsymbol{\xi})$ from Equation (51) turns out to be a very useful tool in MHD instability research due to its mathematical property of being a self-adjoint operator, what means

$$\mathbf{F} = \mathbf{F}^*, \tag{221}$$

where $\mathbf{F}^*$ is the complex conjugate of $\mathbf{F}$. Self-adjointness is valid for the flowless ideal MHD case of $\mathbf{F}$ in Equation (52) and for a plasma configuration with no resistive walls. The general case is thus not self-adjoint. For two arbitrary vectors $\boldsymbol{\xi}$ and $\boldsymbol{\eta}$, which satisfy boundary conditions like in Sec. 3.1.2, the following

integrals

$$\int \mathrm{d}\mathbf{r}\ \boldsymbol{\eta} \cdot \mathbf{F}(\boldsymbol{\xi}) = \int \mathrm{d}\mathbf{r}\ \boldsymbol{\xi} \cdot \mathbf{F}(\boldsymbol{\eta}), \tag{222}$$

are invariant on the interchange of both vectors $\boldsymbol{\xi}$ and $\boldsymbol{\eta}$, what means self-adjointness of $\mathbf{F}$.
The indication of stability leans on the sign of ω^2, what is called the *energy principle*. For unstable configurations the eigenvalues ω^2 are pure real. This is true for discrete modes, which satisfy the eigenequation Equation (51) for discrete eigenvalues ω^2. The force operator is dot multiplied with $\boldsymbol{\xi}^*$ and afterwards integrated over the volume, then the conjugate F^* is dot multiplied with $\boldsymbol{\xi}$ and integrated in the same way.

$$\mathbf{F}(\boldsymbol{\xi}) \mid \int \cdot \boldsymbol{\xi}^* \mathrm{d}\mathbf{r} \quad , \quad \mathbf{F}^*(\boldsymbol{\xi}^*) \mid \int \cdot \boldsymbol{\xi} \mathrm{d}\mathbf{r}. \tag{223}$$

With the use of the self-adjointness in Equation (222), one receives

$$\left(\omega^2 - (\omega^*)^2\right) \int \rho |\boldsymbol{\xi}|^2 \mathrm{d}\mathbf{r} = 0, \tag{224}$$

what means

$$\omega^2 = (\omega^*)^2. \tag{225}$$

This is only possible if ω^2 is real. From the frequency dependence of the modes, which is proportional to $e^{-i\omega t}$, it can further be pointed out that modes with frequencies $\omega^2 > 0$ represent a pure oscillation and can therefore be considered to be stable. Modes with $\omega^2 < 0$ have an exponentially growing contribution and are considered to be unstable.
The change from stable to unstable mode happens at $\omega^2 = 0$. For self-adjoint operators this is the case exactly at $\mathrm{Im}(\omega) = 0$ and $\mathrm{Re}(\omega) = 0$. In general cases (non self-adjoint), transition to instability happens at $\mathrm{Im}(\omega) = 0$, but at $\mathrm{Re}(\omega) \neq 0$, see Figure 14.
An another important property of eigenmodes of a self-adjoint operator is that the eigenmodes are orthogonal on each other. For two modes $(\boldsymbol{\xi}_m, \omega_m^2)$ and $(\boldsymbol{\xi}_n, \omega_n^2)$ where $n \neq m$ are indices of different modes, the eigenequation Equation (51) for the n-mode is dot multiplied by $\boldsymbol{\xi}_m$ and vice versa for the m-mode.

$$-\omega_m^2 \rho \boldsymbol{\xi}_m = \mathbf{F}(\boldsymbol{\xi}_m) \mid \cdot \boldsymbol{\xi}_n \quad , \quad -\omega_n^2 \rho \boldsymbol{\xi}_n = \mathbf{F}(\boldsymbol{\xi}_n) \mid \cdot \boldsymbol{\xi}_m, \tag{226}$$

what leads under consideration of self-adjointness from Equation (222) to

$$\left(\omega_n^2 - \omega_m^2\right) \int \rho\ \boldsymbol{\xi}_m \cdot \boldsymbol{\xi}_n \mathrm{d}\mathbf{r} = 0, \tag{227}$$

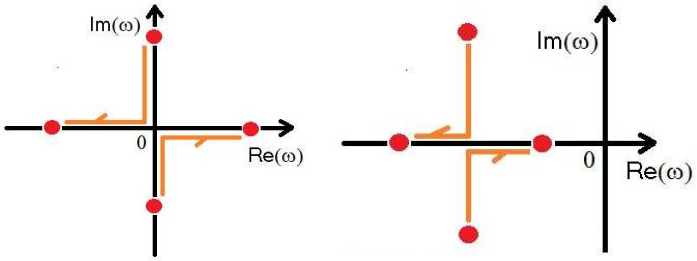

Figure 14: Evolution of two symmetric MHD mode frequencies (solutions of $\omega^2 = 0$) in the complex plane while a perfectly conducting wall is moved radially inward. The stabilising wall position is reached at Im(ω)=0. *left*: For the self-adjoint case stabilisation happens also at Re(ω)=0. *right*: Non-self-adjoint cases have nonvanishing real parts of the mode frequency. Stabilisation happens at Im(ω)=0 but in general at Re(ω) $\neq 0$.

and for two distinct modes with $\omega_n^2 \neq \omega_m^2$ immediately to

$$\int \rho \, \boldsymbol{\xi}_m \cdot \boldsymbol{\xi}_n \mathrm{d}\mathbf{r} = 0. \tag{228}$$

This means that the modes are orthogonal on each other with weight function ρ, which is the mass density.

5.4 The Resistive Wall Mode RWM

In reality, the ideal wall has to be treated as a medium with finite conductivity σ, thus resistive. An analytic approach for modelling such a wall, is given in Sec. 4. In fact, the Vessel wall is desired to be resistive, because this allows external magnetic fields a better penetration into the plasma to control it by external coils (Ref. [11]). It turns out that the resistivity of the wall has a significant effect on wall stabilisation of plasma modes. A plasma configuration which is stable for a perfectly conducting wall is unstable for a resistive wall. Modes get never fully wall stabilised by a resistive wall. For wall positions above the stabilisation of the ideal wall mode, the resistive wall case corresponds in mode growth rates nearly to the ideal wall case. This is not true below the ideal wall stabilising position, there the resitive wall case remains unstable with growth rates which range at Im(ω) $\approx \frac{1}{\tau_w}$ (this behaviour was discussed in Refs. [4, 11, 39]), here τ_w is the characteristic resistive wall diffusion time,

$$\tau_w = \frac{4\pi\sigma b d}{c^2}, \tag{229}$$

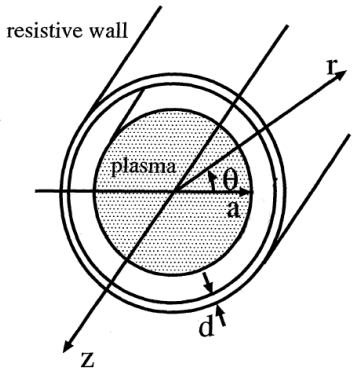

Figure 15: Resistive wall in cylindrical symmetry (r, Θ, z). Plasma radius a, wall thickness d and poloidal angle Θ. Between plasma and resistive wall a vacuum region is assumed. (source:Ref. [39]).

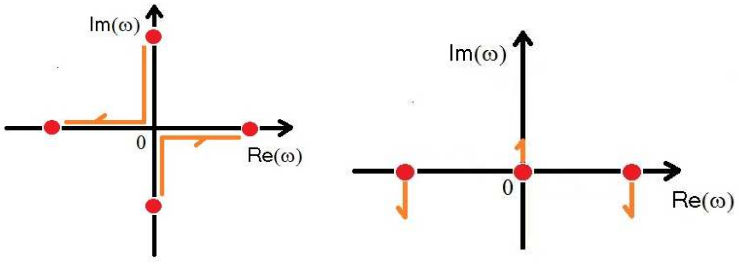

Figure 16: Change of growth rates $\omega = \omega_r + \mathrm{i}\omega_i$ predicted by the MHD model. *left*: Unstable mode (and symmetric stable mode) move on imaginary axis while the ideal wall is moved radially inwards. At stabilisation the pure imaginary frequency ω becomes pure real. *right*: Increase of resistivity. Mode frequencies grow into the imaginary plane. The RWM develops with Re(ω)=0. (Ref. [11])

with conductivity σ, speed of light c, wall position b and wall thickness d.
In other words, the use of a resistive wall results in the occurence of an additional mode with slow gowth rate, the RWM. Figure 16 describes the change of a mode's eigenfrequency in the complex plane during stabilisation by an ideal wall and a following increase of the wall's resistivity (the wall is moved radially inwards and after stabilisation σ is increased) resulting from the MHD model. The ideal wall case demands, that ω^2 is real, what means that ω can lie only on the imaginary or on the real axis. With the ideal wall at stabilisation position, it holds that $\omega^2 = 0$, in other words the mode changes at stabilisation from a pure imaginary ω to a pure real. For a self-adjoint case exactly at Re(ω)=0. After stabilisation, the mode (due to the ω^2 term, always two symmetric solutions $\pm\omega$ are expected to exist, see Figure 16) moves on the real axis and ω gets pure

real. If the resistivity of the wall is continuously enlarged for such a stabilised case with $\mathrm{Im}(\omega) = 0$ and $\mathrm{Re}(\omega) \neq 0$, see right plot of Figure 16, then the mode frequency ω moves into the imaginary plane and becomes complex, $\omega = \omega_r + \mathrm{i}\omega_i$. It can be observed, that the additional mode grows out of $\omega^2 = 0$ at $\mathrm{Re}(\omega)$=0 after wall resistivity is applied. This mode is the resistive wall mode RWM.
The physical picture of the RWM is the following (discussed in Ref. [11]). An unstable instability (perturbation) produces a plasma displacement which induces currents inside the wall. According to Lenz's law, these currents flow in such a direction, that a reinduced motion acts against the perturbation plasma flow to stabilise it. In the case of a resistive wall, these currents decrease due to dissipation on the scale of the wall diffusion time τ_w. A consequence is that the currents which counteract to the perturbation are not able to exist permanently, what means that the perturbation can grow further on. Because this is true only for instabilities with $\tau \approx \tau_w$, the RWM growth rates are much smaller than ideal MHD growth rates, which have $\tau_{\mathrm{MHD}} << \tau_w$ and are nearly unaffected by dissipative effects inside the resistive wall.
RWM growth rates increase with $\beta = \frac{4\pi < p >}{B^2}$ ($< p >$ is an average value of p throughout the plasma) and set a limit in β for fusion operation. Control of RWMs can be achieved by plasma rotation or by a feedback with error fields which couple to the internal fields and are produced by external coils. Possible is also a combination of both feedback and rotation. Effects of plasma rotation have been modelled in Ref. [4] and experimentally underlined at DIII-D in Refs. [33, 34]. It was discovered that with use of rotation a small percentage (about 20%) of the Alfven velocity is needed to stabilise RWMs fully (Ref. [15]). Error fields are discovered to slow down the plasma rotation what is a matter of RWM control by external fields (Refs. [12, 28]).
The modelling by kinetic models is a very new approach and in stage of progress. From first results it is expected that the MHD models overestimate the range of plasma flow which is needed for stabilisation by up to 50%, (Ref. [15]). This tendency is supported also by results from DIII-D, (Refs. [33, 34]). Kinetic effects like collisions, temperature and viscosity effects are a purpose of actual modellings.

6 The Reversed Field Pinch RFP

Reversed field pinches RFPs are toroidal fusion experiments which are characterised by short pulses and high currents and are thus unstable to a broad spectrum of kink modes (Ref. [10]). Due to this properties, RFPs are very useful for RWM investigation.

6.1 Description

The main property of the reversed field pinch is that the toroidal magnetic field has a reversal point inside the plasma, what means that it changes its direction there. The poloidal magnetic field has no reversal point. A schematic plot of magnetic fields and the pressure profile is shown in Figure 17. In Ref. [11] it

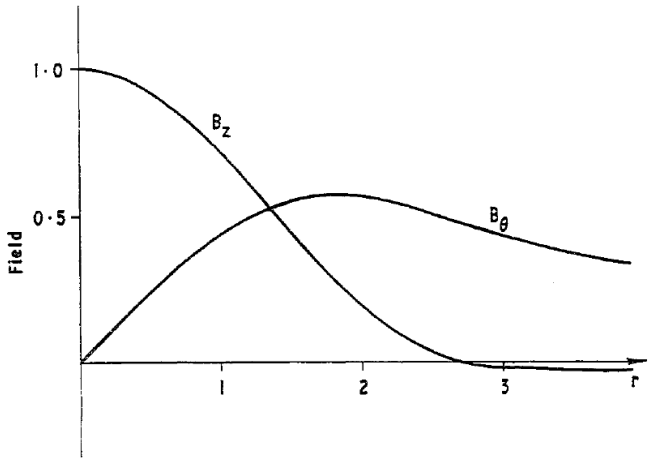

Figure 17: Schematic plot of typical poloidal and toroidal magnetic field components in a reversed field pinch. The toroidal field B_z has a reversal point where it changes its direction. (source: Ref. [30])

is mentioned that cylindrical descriptions are appropriate for RFP modelling because toroidal corrections are very small. Early studies of MHD stability in Refs. [13, 30] confirmed that the RFP profile is a good configuration for keeping the plasma stable even at high β values (it is also possible to stabilise ideal kinks by the presence of a perfectly conducting wall). The reversal of the toroidal magnetic field acts stabilising on internal pressure driven instabilities (in Ref. [11] this is shown by the application of the energy principle).
Various investigations on RWM in RFPs have been done using MHD models to

describe stabilisation by wall and plasma rotation (e.g. Refs. [14, 36]). These aspects are further discussed in Sec. 7.4. The approach by kinetic modelling is a matter of actual research.
In general, the stability of the RFP is strongly influenced by the shape of plasma profiles. In Ref. [11] it is mentioned that a minimum in B_z is required to establish a MHD equilibrium. Compared to Tokamaks, the poloidal magnetic field is very large and can be even larger than the toroidal field. This property gives a large aspect ratio what leads to the important technological advantage, that it is possible to heat the plasma up to ignition only by Joule heating. Toroidal effects do not matter significantly in MHD stability because of the strong poloidal field. This causes only a small toroidal plasma shift. It is mentioned in Ref. [11] that toroidicity is needed only for closing of field lines. Practically it is very challenging to generate RFP profiles with a B_z-reversal and a flat p-profile. Therefore a permanently present amount of turbulence is needed for reversal maintenance (see Ref. [11]). The confinement properties do not benefit from the presence of such turbulence. Although these processes are not well understood so far, the RFP is an attractive fusion device due to its operation at high β, favorable properties concerning MHD stability at high aspect ratio and the possibility of Joule heating up to ignition. A technological disadvantage is the need of a perfectly conducting wall relatively close to the plasma to achieve MHD stability.

6.2 RFP Equilibrium

The RFP equilibrium is described by the α-Θ_0 equilibrium model used in Ref. [14] and can be derived in cylindrical symmetry from the ideal MHD-equilibrium

$$\nabla p_0 = \frac{1}{c}\,\mathbf{j}_0 \times \mathbf{B}_0, \tag{230}$$

$$\nabla \times \mathbf{B}_0 = \frac{4\pi}{c}\mathbf{j}_0, \tag{231}$$

with $\mathbf{B_0} = (0, B_{0\theta}(r), B_{0z}(r))$ the equilibrium magnetic field, $p_0(r)$ the equilibrium pressure, $\mathbf{j}_0(r)$ the equilibrium current density, and c the speed of light. For brevity, subscript zero is dropped in the following.
Equation (230) and Equation (231) lead to the force balance in cylindrical symmetry

$$\frac{\partial}{\partial r}\left(p + \frac{B_\Theta^2 + B_z^2}{8\pi}\right) + \frac{B_\Theta^2}{4\pi r} = 0. \tag{232}$$

The current density in Equation (231) is expressed by it's components parallel and prependicular to the magnetic field,

$$\nabla \times \mathbf{B} = \frac{4\pi}{c} \left(\mathbf{j}_{\perp} + \mathbf{j}_{\parallel} \right). \tag{233}$$

It is now possible to write the Θ- and z-components of Equation (233) by means of perpendicular and parallel current components

$$\frac{\mathrm{d}B_z}{\mathrm{d}r} = -\frac{4\pi}{c} j_{\Theta} = -\frac{4\pi}{c} \left(j_{\Theta\perp} + j_{\Theta\parallel} \right), \tag{234}$$

$$\frac{1}{r}\frac{\mathrm{d}}{\mathrm{d}r}\left(rB_{\Theta} \right) = \frac{4\pi}{c} j_z = \frac{4\pi}{c} \left(j_{z\perp} + j_{z\parallel} \right). \tag{235}$$

For further steps, the current components are expressed as projections on the magnetic field like

$$\mathbf{j}_{\parallel} = \frac{\mathbf{j} \cdot \mathbf{B}}{B^2} \mathbf{B}, \tag{236}$$

$$\mathbf{j}_{\perp} = -\frac{\mathbf{j} \times \mathbf{B}}{B^2} \times \mathbf{B}. \tag{237}$$

To derive Equation (237), the relations

$$\mathbf{j}_{\perp} = \mathbf{j} - \mathbf{j}_{\parallel}, \tag{238}$$

$$(\mathbf{j} \times \mathbf{B}) \times \mathbf{B} = (\mathbf{B} \cdot \mathbf{j})\, \mathbf{B} - (\mathbf{B} \cdot \mathbf{B})\, \mathbf{j}, \tag{239}$$

have been used. From Equation (230) and Equation (237) the perpendicular current density is

$$\mathbf{j}_{\perp} = \frac{c}{B^2} \left(\mathbf{B} \times \nabla p \right). \tag{240}$$

Effects of the parallel current are important for RFP stability. To be able to estimate the influence of $\mathbf{j}_{\parallel}$ better, Equation (236) is expressed by the *parallel current distribution* μ as

$$\mathbf{j}_{\parallel} = \frac{\mathbf{j} \cdot \mathbf{B}}{B^2} \mathbf{B} = \frac{c\mu}{4\pi} \mathbf{B}, \tag{241}$$

like in Refs. [1, 25]. Here, c is the speed of light and

$$\mu = \frac{2}{a} \Theta_0 \left[1 - \left(\frac{r}{a} \right)^{\alpha} \right], \tag{242}$$

with shape parameters α and Θ_0 and plasma radius a. The parameter Θ_0 is related to the safety factor at the axis and the major radius by $q\left(0\right) = \frac{a}{\Theta_0 R}$.

From Equation (234) and Equation (235) the α-Θ_0 *equilibrium model* is now given by the following equations,

$$\frac{\mathrm{d}B_z}{\mathrm{d}r} = -\mu B_\theta - \frac{4\pi B_z}{B^2}\frac{\mathrm{d}p}{\mathrm{d}r}, \tag{243}$$

$$\frac{1}{r}\frac{\mathrm{d}}{\mathrm{d}r}\left(rB_\theta\right) = \mu B_z - \frac{4\pi B_\theta}{B^2}\frac{\mathrm{d}p}{\mathrm{d}r}, \tag{244}$$

$$\frac{\mathrm{d}p}{\mathrm{d}r} = -\chi\frac{r}{8\pi}\left(\frac{\mu B^2}{2B_\Theta} - \frac{B_z}{r}\right)^2. \tag{245}$$

$$\tag{246}$$

Here, χ is a constant which determines the effect of pressure gradients. Equation (245) gives Suydam's necessary condition for stability when $\chi < 1$. Derived parameters describing this model are the poloidal beta β_p, the reversal parameter F, and the pinch parameter Θ,

$$\beta_p = \frac{8\pi}{B_\theta^2(a)}\langle p\rangle = \frac{8\pi}{B_\theta^2(a)}\frac{1}{\pi a^2}\int_0^a \mathrm{d}r\, 2\pi r p(r), \tag{247}$$

$$F = \frac{B_z(a)}{\langle B_z\rangle}, \qquad \Theta = \frac{B_\theta(a)}{\langle B_z\rangle}. \tag{248}$$

So each set of equilibrium parameters (α, χ, Θ_0) defines a RFP equilibrium with resulting parameters (F, Θ, β_p) and vice versa.

6.3 Computation of the RFP Equilibrium

Equation (243), Equation (244) and Equation (245) represent a coupled system of differential equations of first order which can be solved numerically by a Runge-Kutta boundary value solver. The equations are normalised and after integration multiplied by realistic RFP values. The magnetic fields are normalised by the value of the poloidal magnetic field at the plasma surface $B_{\Theta a}$, the radius is normalised by the plasma radius a, the normalised pressure is $\overline{p} = \frac{8\pi p}{B_{\Theta a}^2}$. The resulting normalised RFP equilibrium equations are

$$\frac{\mathrm{d}\overline{B}_z}{\mathrm{d}\overline{r}} = -\overline{\mu}\overline{B}_\theta - \frac{\overline{B}_z}{2\overline{B}^2}\frac{\mathrm{d}\overline{p}}{\mathrm{d}\overline{r}}, \tag{249}$$

$$\frac{1}{\overline{r}}\frac{\mathrm{d}}{\mathrm{d}\overline{r}}\left(\overline{r}\overline{B}_\theta\right) = \overline{\mu}\overline{B}_z - \frac{\overline{B}_\theta}{2\overline{B}^2}\frac{\mathrm{d}\overline{p}}{\mathrm{d}\overline{r}}, \tag{250}$$

$$\frac{\mathrm{d}\overline{p}}{\mathrm{d}\overline{r}} = -\chi\overline{r}\left(\frac{\overline{\mu}\overline{B}^2}{2\overline{B}_\Theta} - \frac{\overline{B}_z}{\overline{r}}\right)^2, \tag{251}$$

$$\overline{\mu} = 2\Theta_0\left[1-(\overline{r})^\alpha\right]. \tag{252}$$

The normalised quantities are overlined. For integration, the following boundary conditions

$$\overline{B}_\Theta|_0 = 0 \quad , \quad \overline{B}_z|_0 = B_{z0} = 1, \tag{253}$$

$$\frac{\mathrm{d}\overline{B}_\Theta}{\mathrm{d}\overline{r}}|_0 = \Theta_0 B_{z0} \quad , \quad \frac{\mathrm{d}\overline{B}_z}{\mathrm{d}\overline{r}}|_0 = 0, \tag{254}$$

$$\frac{\mathrm{d}\overline{p}}{\mathrm{d}\overline{r}}|_0 = 0. \tag{255}$$

are needed. The index $|_0$ represents the value at $\overline{r}=0$. The integration is carried out from the cylinder axis $\overline{r}=0$ to the plasma radius $\overline{r}=1$.
RFP equilibria given in this section were computed by `ode45` from *MATLAB*. The influence of the parameters (α, Θ_0, χ) on the RFP equilibrium quantities can be discussed like in Refs. [14,36]. Table 2 shows the influence on (F, Θ, β_p).

Nr.	α	Θ_0	χ	F	Θ	β
1	5.5	1.5	0.0	-0.18	1.48	0.0
2	8.0	1.5	0.0	-0.47	1.58	0.0
3	3.63	1.7	0.0	-0.47	1.74	0.0
4	8.16	1.5	1.0	-0.59	1.93	0.081
5	7.74	1.5	1.5	-0.59	2.08	0.126

Table 2: RFP equilibrium parameters (F, Θ, β_p) which result from parameters (α, χ, Θ_0).

Case 1 corresponds to the zero pressure Equilibrium (1) in Figure 6 of Ref. [14]. The effect on F and Θ can be estimated for the case that α (Case 2) or Θ_0 (Case 3) are varied. Case 4 corresponds to Equilibrium 5 in Figure 6 of Ref. [14]. Case 5 shows the change in α and Θ_0 if $F = const$ for a change in β. Figure 18 shows the RFP equilibrium magnetic fields and the q-profile for Cases 1, 2 and 3 from Table 2. These three equilibria have zero pressure. Changes in the pressure can be seen in Figure 19. There χ is varied under constant F and Θ_0. Pressure and pressure gradient profiles for Cases 4 and 5 are shown in Figure 20. Figure 21 shows temperatures and the particle density for Case 4 in Table 2. The particle density is equal for ions and electrons and is chosen to be constant like suggested in Ref. [14]. To scale the profiles to realistic RFP

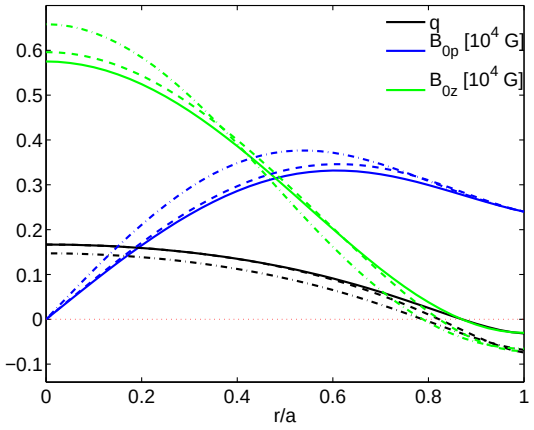

Figure 18: RFP equilibrium profiles: Safety factor q, poloidal magetic field B_{0p} and toroidal magnetic field B_{0z}. The solid line is for Case 1 in Table 2, the dashed line corresponds to Case 2 and dash-dot to Case 3. All three cases have zero pressure.

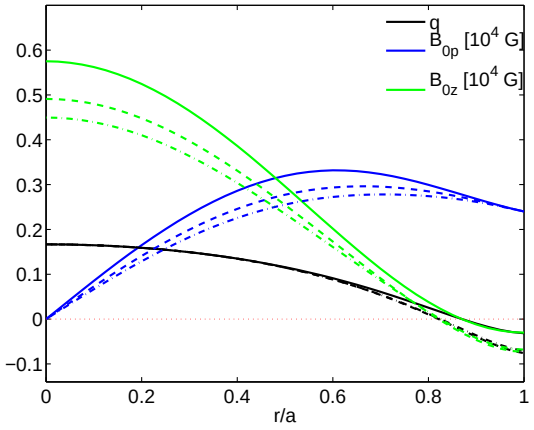

Figure 19: RFP equilibrium profiles: Safety factor q, poloidal magetic field B_{0p} and toroidal magnetic field B_{0z}. The solid line corresponds to Case 1 in Table 2, the dashed line corresponds to Case 4 and dash-dot to Case 5.

values, it is enough to set $B_{\Theta a}$ at plasma radius and all other quantities can be unnormalised with correspondence to $B_{\Theta a}$. All described RFP equilibria have $B_{\Theta a} = 2400\text{G}$ what can also be seen in Figure 18 and Figure 19. The temperatures are computed by $T = \frac{p}{k_B n}$ in $[\texttt{eV}]$ with $T = T_\text{e} + T_\text{i}$ and $T_\text{e} = 0.6T$ and $T_\text{i} = 0.4T$. While using MHD, a splitting of temperatures into electron and ion part does not enter the model. This step becomes important while using the kinetic model, where particle interactions depend on the differing profiles

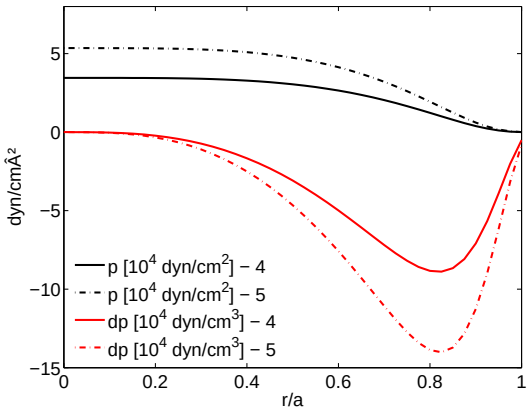

Figure 20: Pressure (black) and pressure gradient (red) for Case 4 (solid) and Case 5 (dash-dot) from Table 2.

of electron and ion temperatures, see Sec. 7.8

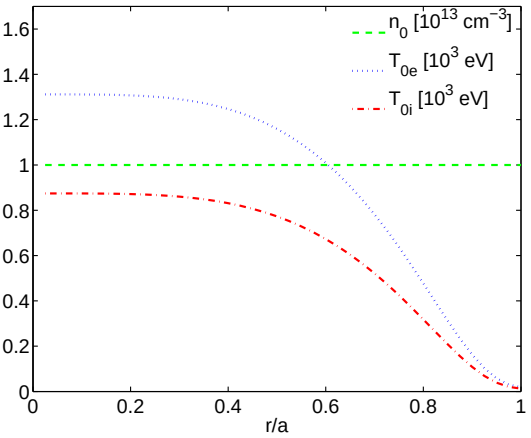

Figure 21: Background profiles for density n_0, electron temperature T_e, and ion temperature T_i for Equilibrium 4 in Table 2.

7 Results of RFP Investigations

7.1 Zone Configurations for RFP Modelling

While modelling growth rates of ideal and resistive wall modes in RFP symmetry by the KiLCA code, Maxwell equations have to be solved in different media like discussed in Sec. 4. Figure 22 shows the zone configurations for MHD and kinetic (flre) modelling of the ideal wall mode. Outside the plasma region a vacuum region is assumed which is closed by an ideal wall at the outer edge. The corresponding boundary conditions are discussed in Sec. 4. The KiLCA

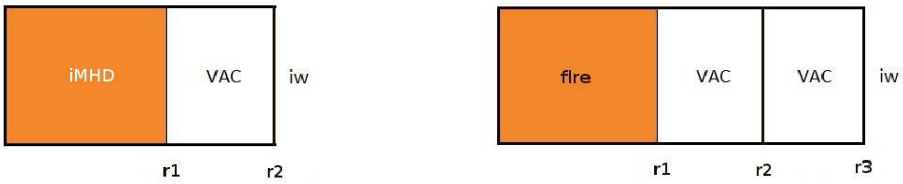

Figure 22: *left*: Two zones for modelling the ideal wall mode by the MHD code. Between plasma radius $r1$ and ideal wall (iw) at $r2$ a vacuum zone is applied. The antenna can be placed exactly at plasma radius. *right*: Three zones for modelling the ideal wall mode by the kinetic code. The vacuum zone from the MHD case is split into two zones by the antenna at $r2$. Here $r3$ marks the ideal wall position.

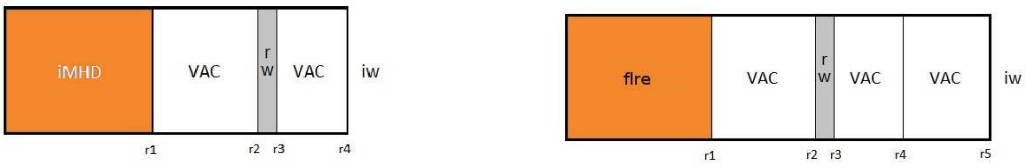

Figure 23: *left*: Four zones for modelling the resistive wall mode by the MHD code with antenna at plasma surface $r1$. *right*: Five zones for modelling the resistive wall mode by the kinetic code, where the antenna is placed in the outer vacuum zone at $r4$. Both configurations are closed by an ideal wall at the outer edge.

code is programmed in such a way that an antenna must always be added to the zone configuration. During the calculation of ideal and resistive wall modes the antenna currents are set to zero. When using the MHD code, the antenna is placed exactly at plasma surface, because of numerical stability reasons this is not possible for the kinetic code, where the antenna must be placed at the

boundary of two media of the same type (e.g. *vacuum* - *vacuum*). Figure 23 shows the zone configuration of MHD and kinetic modelling for the resistive wall mode. A resistive wall is placed outside the plasma surrounded by vacuum regions. In case of kinetic modelling, the outer vacuum region is split into two vacuum regions by the antenna at $r4$. Both configurations are closed by an ideal wall at the outer edge what represents the vessel wall.

7.2 MHD Model Benchmarking

Investigations in Refs. [14, 36] provide a detailled discussion concerning RWM stabilisation by plasma rotation in a RFP. This section discusses a reproduction of the main results given in Ref. [14] using the KiLCA-MHD code. Equilibrium 4 from Table 2 in Sec. 6.3 is suitable for this purpose because it is equal to Equilibrium 5 in Figure 6 of Ref. [14].
For investigations of the influence of the wall position on the growth rates, the plasma rotation velocity is set to zero. Changes of growth rates by variation

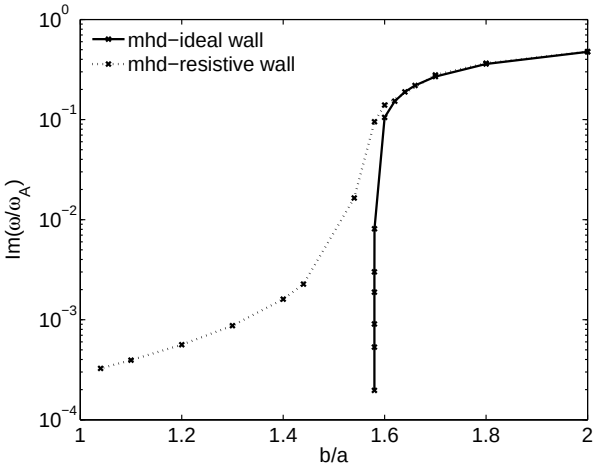

Figure 24: MHD mode growth rates for ideal wall (solid) and resistive wall (dotted) positions $\frac{b}{a}$, normalised by $\omega_{\mathrm{A}} = 2.34e6\mathrm{s}^{-1}$ for Equilibrium 4 from Table 2 and mode $(m, n) = (1, 3)$.

of the wall position for an ideal wall and a resistive wall with conductivity $\sigma = 4.5e14\mathrm{s}$ and wall thickness $d = 5\mathrm{cm}$ are shown in Figure 24. The ideal wall mode is stabilised at $\frac{b}{a} = 1.58$ (solid). For a resistive wall a small growth rate of $\omega = 0 + i \cdot 7.8246953e2\mathrm{s}^{-1}$ at $\frac{b}{a} = 1.05$ remains (dotted) and is never fully stabilised if a rotation is absent. The used MHD modes have $(m, n) = (1, 3)$ what results in a normalised z-component of the wave number $k_z = \frac{na}{R} =$

$\frac{3 \cdot 50\text{cm}}{200\text{cm}} = 0.75$. This corresponds to the case discussed in Ref. [14] and matches their results.
The curves are normalised by ω_A in the same way like this is done in Ref. [14]. For a plasma radius $a = 50\text{cm}$, one gets

$$\omega_\text{A} \;=\; \frac{V_\text{A}}{a} \;=\; \frac{B_{0\theta}(a)/\sqrt{4\pi\rho}}{a} \;=\; \frac{1.17 \times 10^8\,\text{cm/s}}{50\,\text{cm}} \;=\; 2.34 \times 10^6\,\text{s}^{-1}. \quad (256)$$

The application of a plasma rotation opens an interval for $\frac{b}{a}$ where the RWM can be fully stabilised. The width of this interval is a function of the plasma rotation speed. Figure 25 shows two cases of poloidal plasma rotation ($V_z = 0.5V_\text{A}$ and $V_z = 0.7V_\text{A}$) which are constant over radius. The width of the window increases

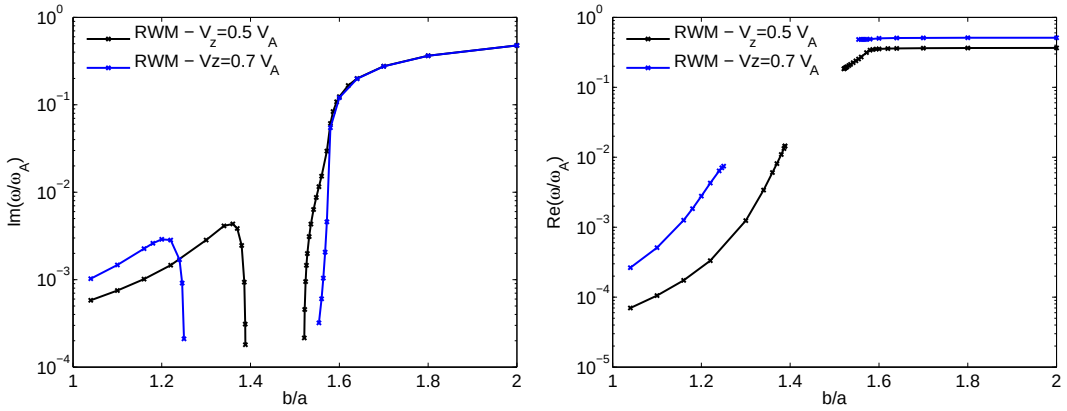

Figure 25: Windows of stable wall positions for a plasma rotation with $V_z = 0.5V_\text{A}$ and $V_z = 0.7V_\text{A}$ for Equilibrium 4 from Table 2. Growth rates are shown by the left plot and the real parts are shown by the right plot. Inside the window there is no data. The normalisation is done by $\omega_\text{A} = 2.34e6\text{s}^{-1}$.

with V_z. The wall positions where the windows open differ little from the result given by Figure 10 in Ref. [14] (in Ref. [14] the windows open: for $V_z = 0.5V_\text{A}$ at $\frac{b}{a} = 1.46$ and for $V_z = 0.7V_\text{A}$ at $\frac{b}{a} = 1.38$), but the growth rates of Figure 25 match the given results at $\frac{b}{a} = 1.05$ and $\frac{b}{a} = 2.0$. The difference in window position results from the range of the Alfven velocity which is not exactly known from Ref. [14], because of the unknown range of magnetic fields. But the general behaviour of RWM from Ref. [14] is successfully recomputed.

7.3 Estimate of the Influence of the Galileian Moving Frame Velocity on Kinetic Modelling

All computations using the kinetic model are computed in a frame which moves in toroidal direction. Consequently all results have to be transformed back to the laboratory frame using Galileian transformation. One of the common needs to receive trustable results, is the invariance of results on the choice of the moving frame velocity, like described in Ref. [19]. The Galileian frame velocity v_{gal} transforms the plasma motion to a moving frame with velocity V_z^{frame} and enters to the kinetic code by

$$V_z^{frame} = sV_z - v_{\text{gal}}, \tag{257}$$

where V_z is the toroidal plasma background rotation and s is a constant which is used to scale V_z. Figure 26 shows the dependence of the normalised growth

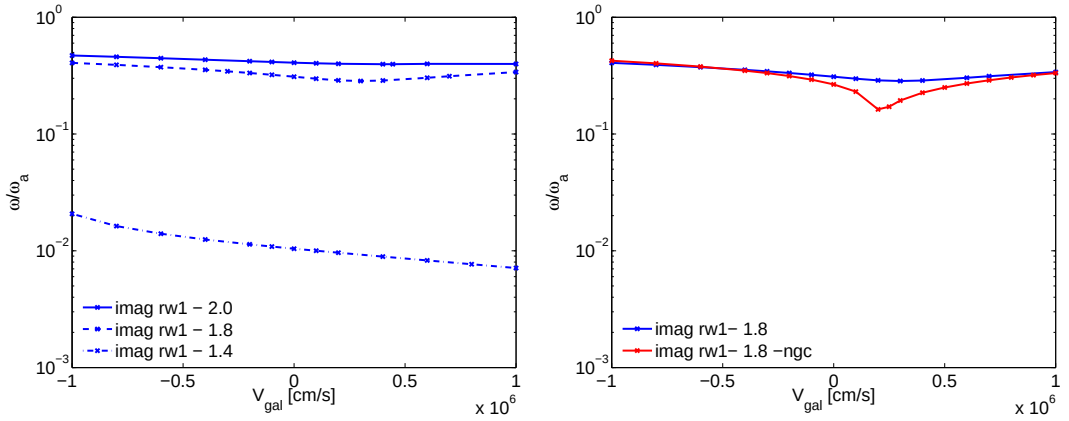

Figure 26: Dependence of the kinetic ideal wall mode frequency on the v_{gal} velocity of the moving frame. *left*: Plotted are growth rates of the *rw1*-mode for resistive wall positions $rw/a = 2.0$, $rw/a = 1.8$ and $rw/a = 1.4$. *right*: Growth rates of the *rw1*-mode for resistive wall position $rw/a = 1.8$ for an applied Galileian correction term and without it.

rates on the Galileian frame velocity v_{gal}. The growth rates shown are computed by the kinetic model including the collision term from Sec. 3.2 and an applied resistive wall like discussed in Sec. 7.1. They correspond to the *rw1*-mode discussed in Sec. 7.4. The left plot compares the v_{gal}-dependence for the three different wall positions $rw/a = 2.0$, $rw/a = 1.8$ and $rw/a = 1.4$. The right plot compares the v_{gal}-dependence for the *rw1*-mode growth rates at $rw/a = 1.8$ while a Galileian correction term is used and without it.
The invariance is fullfilled up to values of $\pm 1e6$ $\frac{\text{cm}}{\text{s}}$, here the change of the

growth rates vary less than 10%. Outside this the Galileian invariance is significantly violated. Modes propagating with the velocity of the moving frame might become superalfenic. In this sense the wall might lose its effect on the mode (current induction), within what the mode can change its frequency.

7.4 Sensitivity of Ideal Kink and RWM on the Wall Position

This section discusses results of computations done on RFP equilibria mentioned in Sec. 6.3 and published in Ref. [26].
It is desired to investigate instabilities of RFP equilibria both by the MHD and the kinetic model and compare predictions of both models for a RFP plasma getting stabilised by changes in ideal and resistive wall positions and by application of toroidal plasma rotation.
For investigations of this purpose, the equilibrium plasma background Case 4 from Table 2 in Sec. 6.3 is suitable (it is equal to Equilibrium 5 in Figure 6 of Ref. [14]). The profiles are shown in Figure 19, Figure 20 and Figure 21.
The Alfven rotation frequency ω_{A} remains for the applied equilibrium as $\omega_{\mathrm{A}} = 2.34 \times 10^6 \mathrm{s}^{-1}$ (the same like in Equation (256)). The ideal time scale

$$\tau_{\mathrm{A}} = \frac{1}{\omega_{\mathrm{A}}} \;=\; 4.27 \cdot 10^{-7}\mathrm{s}, \tag{258}$$

is used to express the resistive wall time scale. The resistive wall time scale τ_{w} for wall position $b = 50\,\mathrm{cm}$, wall thickness $d = 5\,\mathrm{cm}$, and wall conductivity $\sigma = 4.5 \cdot 10^{14}\ \mathrm{s}^{-1}$ is then

$$\tau_{\mathrm{w}} = \frac{4\pi b d \sigma}{c^2} \;=\; 0.0016\mathrm{s} \;=\; 3.7 \cdot 10^3\ \tau_{\mathrm{A}}. \tag{259}$$

For a big radius $R = 200$ cm, toroidal and poloidal mode numbers $n = 3$ and $m = 1$, the value for $k = n/R$ agrees with the value in Ref. [14], namely $ka = 0.75$. For the ideal wall positioned at $b/a = 2$ the normalised radial magnetic field $|B_r|$ for the kink instability is shown in the left plot of Figure 27. The right plot shows the normalised $|B_r|$ profile for modes with the resistive wall positioned at $b/a = 1.4$. In this case, two kinetic roots *rw1* and *rw2* have been found whose growth rates are shown in Figure 28. The $|B_r|$ profiles for the MHD and the kinetic model are seen in good qualitative agreement. Figure 28 shows the normalised growth rates of the ideal wall mode (iw) and the resistive wall mode (rw) as a function of the wall position. The MHD result is the same as shown in Figures 5 and 6 of Ref. [14]. The kinetic description of the kink type mode (ideal wall) shows a slightly smaller growth rate for $1.6 < b/a < 2$. More

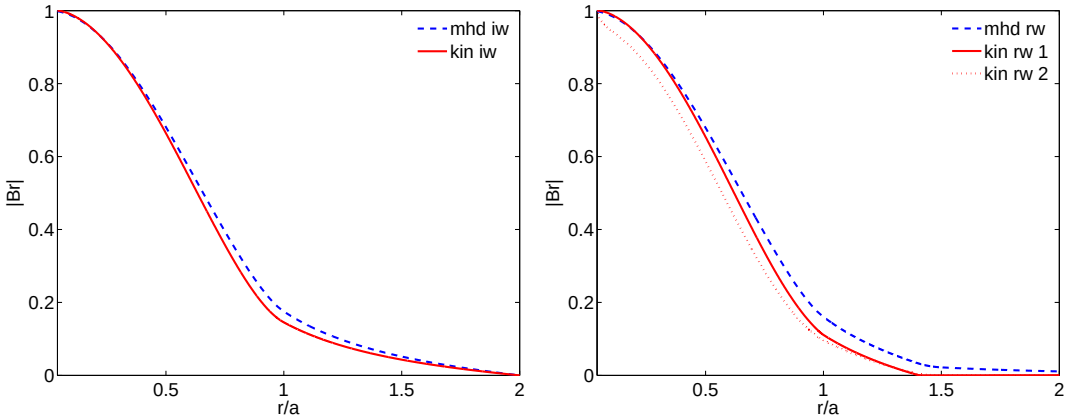

Figure 27: Profiles of the modulus of the radial magnetic field $|B_r|$ for the ideal wall (left) at $b/a = 2$ (ideal kink mode) and the resistive wall (right) at $b/a = 1.4$ (resistive wall mode) without toroidal plasma rotation. Toroidal and poloidal mode numbers are $n = 3$ and $m = 1$ such that the toroidal wave number normalised to the small radius a is $ka = 0.75$. *left*: Blue (dashed) – MHD model, red (solid) – kinetic model. *right*: The ratio of resistive to Alfvénic (ideal) time scale is $\tau_w/\tau_A = 3.7 \times 10^3$. Blue (dashed) – MHD model, red (solid for mode *rw1* and dotted for mode *rw2*) – kinetic model.

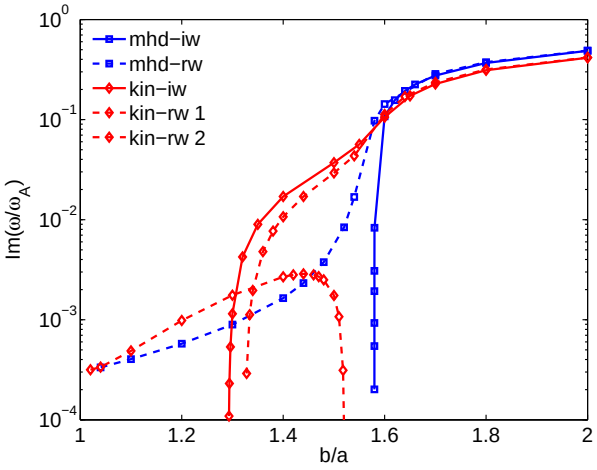

Figure 28: Normalised growth rates of the 'kink' and the 'resistive' mode plotted over the ideal (iw) and resistive wall (rw) position. Mode numbers are $m = 1$ and $n = 3$. The resistive time scale is $\tau_w/\tau_A = 3.7 \cdot 10^3$. Solid lines (square – MHD, diamond – kinetic) for the ideal wall, dashed and dot-dashed lines for the resistive wall. There exist two RWM kinetic solutions *rw1* and *rw2* for $1.35 < b/a < 1.52$.

remarkably one can observe a significant smaller value for mode stabilisation about $b/a \approx 1.3$ compared to $b/a \approx 1.6$ for MHD. Nevertheless, the ideal mode can be still stabilised by an ideal wall close enough to the plasma.
If the wall is resistive, the resistive wall mode appears. In the MHD case, there exists now a mode even for values of $b/a < 1.6$ with growth rates three orders of magnitude smaller, i.e. on the resistive time scale. In the kinetic case, the situation is somewhat different. For values above the ideal stabilisation values of $b/a = 1.3$ it holds for mode *rw1* that there is, similar to MHD, not much difference to the ideal wall case. For small values of the wall position, $1 < b/a < 1.52$, there appears a new mode *rw2*, the kinetic resistive wall mode. Between $1.3 < b/a < 1.52$ both modes *rw1* and *rw2* do coexist. Again, the growth rates found by the kinetic model are in good qualitative agreement with the MHD results.

7.5 Stabilisation by Plasma Rotation

The next point to be adressed is the role of mode stabilisation by toroidal rotation of the plasma. For this purpose an uniform velocity profile (constant over r) for V_z is applied to the RFP equilibrium used in the previous sections. Figure 29 shows the growth rates over toroidal rotation for different positions of the resistive wall. On the left, the results for negative V_z are shown, on the right, the results for positive V_z (plasma current is positive) are shown.
The first thing one can realise is that for MHD the mode stabilisation is symmetric with respect to the sign of V_z. This can be also seen from the formulae in the MHD modelling section if the poloidal velocity is zero. In contrast, kinetic modelling shows stabilisation only for $V_z < 0$ values, whereas for $V_z > 0$ the growth rates slightly increase instead. In the kinetic model the toroidal plasma rotation velocity influences the background electric field and the parallel bulk velocity parameter of the ion and electron background distribution functions. In the expressions that define those quantities there is no symmetry that may lead to such a symmetric behavior of the instability growth rates with respect to direction of toroidal plasma rotation. Another difference can be found for wall position $b/a = 1.1$. MHD predicts instability whereas kinetic theory does not. That means instead of the stability window shown in Figure 25, in the kinetic model there is an upper threshold, $b/a \approx 1.68$ for the wall position only: if the wall is too far away the RWM is not stabilised even for large toroidal rotation velocities. In MHD there is also a lower threshold, $b/a \approx 1.4$, and the RWM is not stabilised for the resistive wall too close to the plasma.
For the case $b/a = 1.4$ one concludes from Figure 29 that in the kinetic model toroidal velocities of about 3% of the Alfvén velocity stabilise the RWM whereas

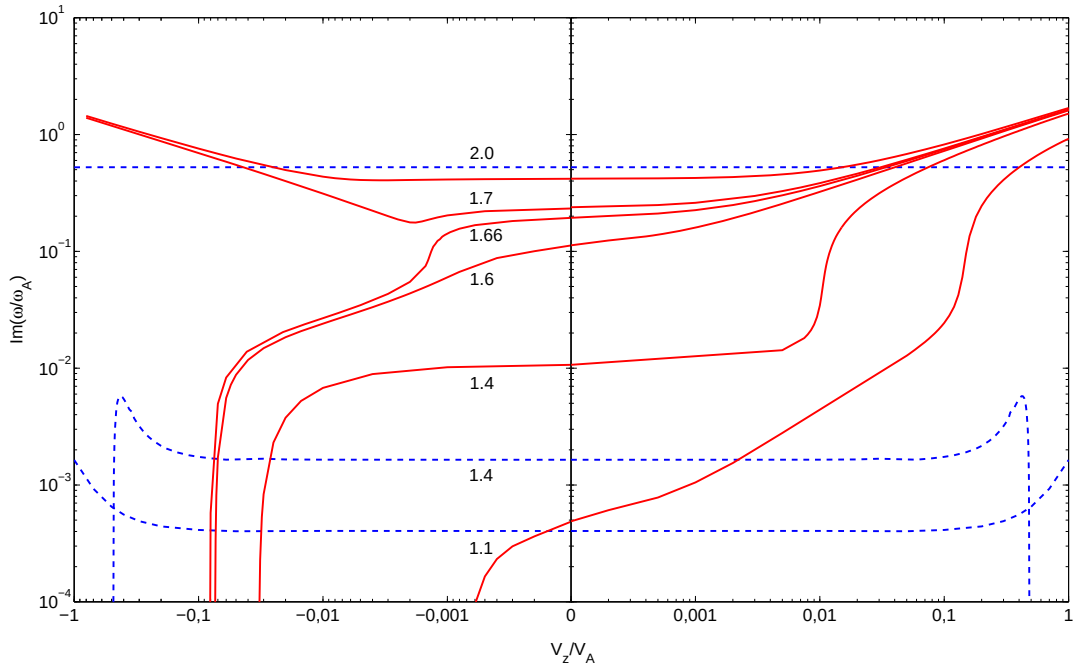

Figure 29: Normalised growth rates for the RWM (*rw1*) at different locations $1.1 < b/a < 2$ as a function of the normalised toroidal plasma velocity V_z/V_A. Mode numbers are $m = 1$ and $n = 3$. The resistive time scale is $\tau_\mathrm{w}/\tau_\mathrm{A} = 3.7 \cdot 10^3$. Dashed lines – MHD model, solid lines – kinetic model. *left:* – toroidal plasma rotation against, *right:* – toroidal plasma rotation with the toroidal plasma current.

in the MHD model this value is about 30%. Small rotation speeds of a few percent of the Alfvén velocity have also been found in Ref. [22] to be sufficient for stabilisation of resistive wall modes in ITER by toroidal rotation.
To investigate the influence of the edge value of the toroidal plasma rotation on the growth rates, three different rotation velocity profiles shown in Figure 30 have been tested.
Note that always the parameter s from Equation (257) sets the fraction of the Alfven velocity (e.g. $s \cdot V_\mathrm{A}$ like done in Figure 29).
The results in Figure 31 show that for smaller rotations speeds at the plasma edge, the stabilisation value for the case $b/a = 1.4$ increases up to 10% of the Alfvén speed. It is concluded that a high enough plasma rotation at the edge is important for stabilisation, whereas differential rotation seems to have no significant impact.

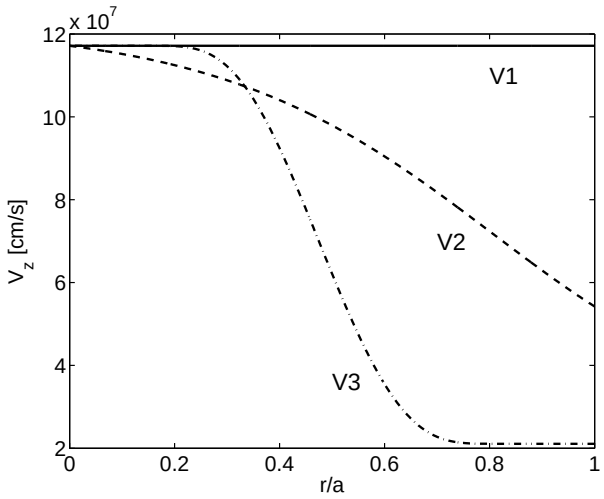

Figure 30: Three different profiles for the toroidal plasma rotation velocity. The constant value of V1 is equal to the Alfven velocity of the RFP equilibrium Case 4 from Table 2 in Sec. 6.3

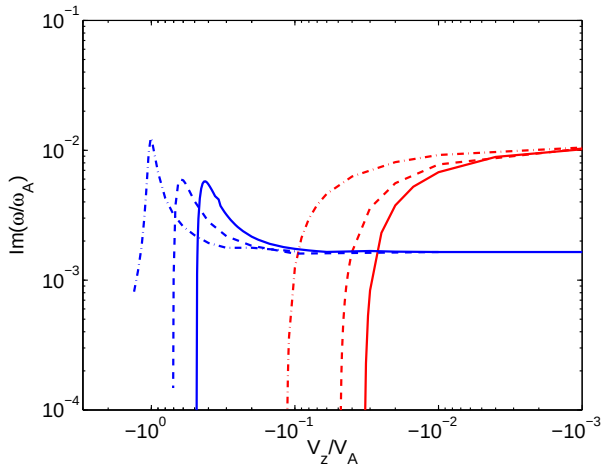

Figure 31: Normalised growth rates for the RWM at $b/a = 1.4$ as a function of the normalised toroidal plasma velocity V_z/V_A for different profiles of the toroidal background plasma velocity shown in Figure 30: V1 solid, V2 dashed, V3 dashed-dotted. *blue* curves – MHD model, *red* curves – kinetic model.

7.6 Influence of Density Profiles

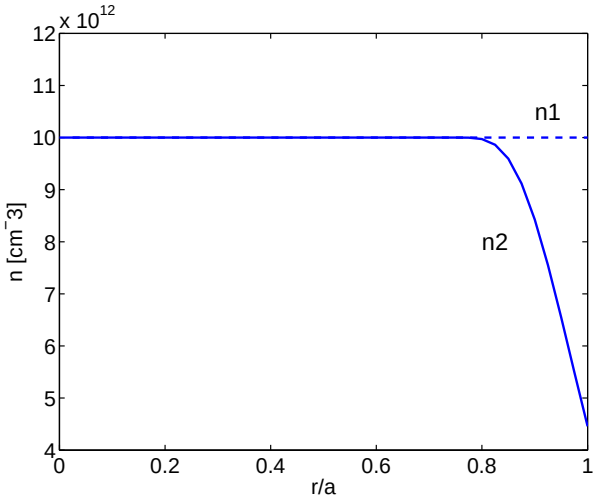

Figure 32: Different density profiles used in the calculations.

To ensure that the jump in density at *plasma - vacuum* interface does not lead to unphysical results, the density profile shown in Figure 32 has been applied. The plots in Figure 33 show no significant difference of growth rates if two different density profiles n1 and n2 are applied to kinetic modelling of RWMs. So only small values of growth rates show a deviation from the n1 profile results of resistive wall modes *rw1* and *rw2* from Sec.7.4. The effect of smooth density n2 on the RWM stabilisation by rotation is shown in Figure 34. It can be seen that the smooth density profile has no significant effect on the MHD model, but the kinetic model reacts somehow more sensitive for higher rotation speeds.
Figure 25 discusses a stable window for a resistive wall position between $1.4 < b/a < 1.6$ predicted by the MHD model. To estimate the influence of the density profile, the same computations have been done for the density profile n2. Both results are compared in Figure 35. For each particular position of the resistive wall the threshold value of the toroidal plasma velocity to stabilise the mode is different. At a velocity of profile V1 with $V_z/V_\mathrm{A} = 0.5$ and density profile n2 only wall positions $1.4 < b/a < 1.6$ can be stabilised. This is shown in Figure 36 for three different positions of the resistive wall $b/a = 1.1$, $b/a = 1.4$ and $b/a = 2.0$.
It is not possible to observe a stable window by the kinetic modelling, see Figure 29. In general, it can be said that the results with a smooth density profile n2 confirm the behaviour of the uniform density profile n1.

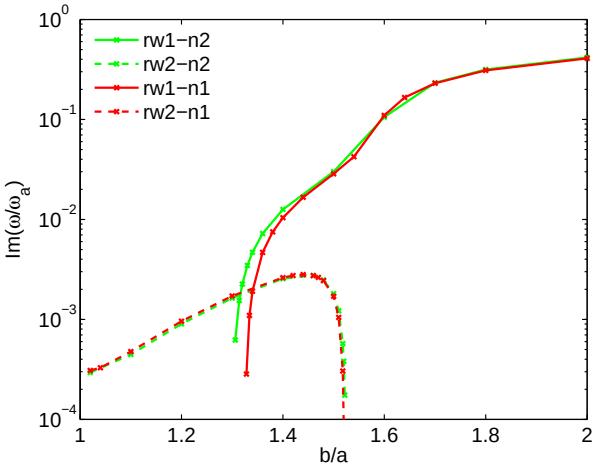

Figure 33: Normalised growth rates for the resistive wall modes *rw1* and *rw2* from Sec.7.4 for density profiles n1 and n2 computed by the kinetic model. A visible difference can be recognised at small growth rates, but these differences are rather small.

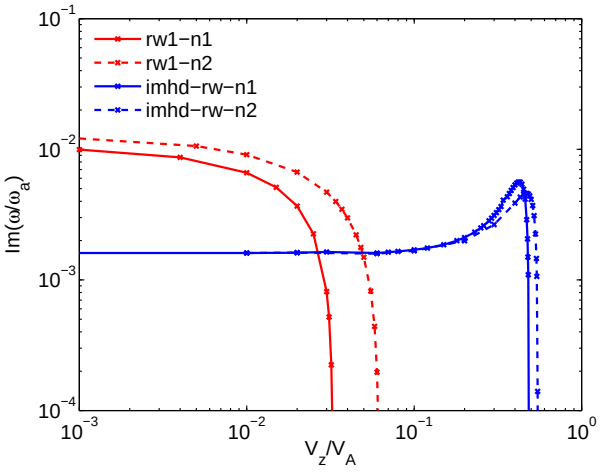

Figure 34: Normalised growth rates for resistive wall modes calculated by the kinetic model (*rw1*) and by the MHD model for both density profiles n1 and n2 in dependence on absolute values of the toroidal rotation velocity (used profile V1). *blue*: MHD - curves, *red*: kinetic - curves.

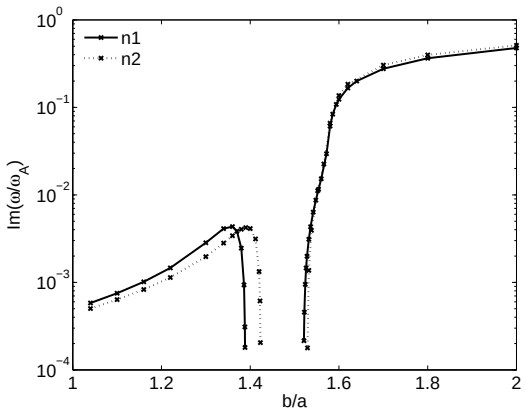

Figure 35: The stable window for $1.4 < b/a < 1.6$ of the RWM calculated by the MHD model for two different density profiles and a toroidal velocity $V_z/V_\mathrm{A} = 0.5$.

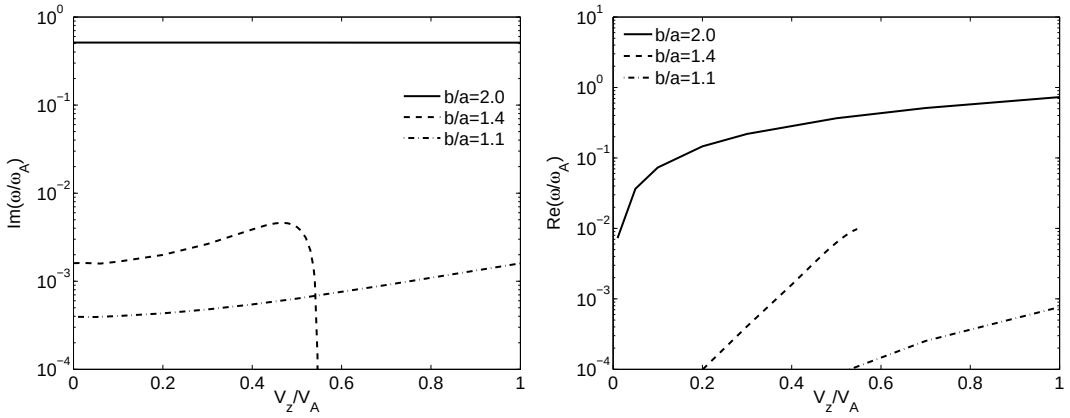

Figure 36: Normalised growth rates (real and imaginary part) for different positions of the resistive wall as a function of the toroidal plasma velocity for the MHD model and density profile n2.

7.7 Energy Dissipation

An important question is where the energy goes during RWM stabilisation. For the frequency range typical to RWM only Cerenkov resonance will contribute to the interaction between the electromagnetic field and particles that in the present cylindrical model are all passing particles. However, it is most likely that magnetic perturbation along the magnetic field lines acting via the grad B force on the particles will add up to the parallel electric perturbation field and thus to the work of the electric field on the parallel current. The relative

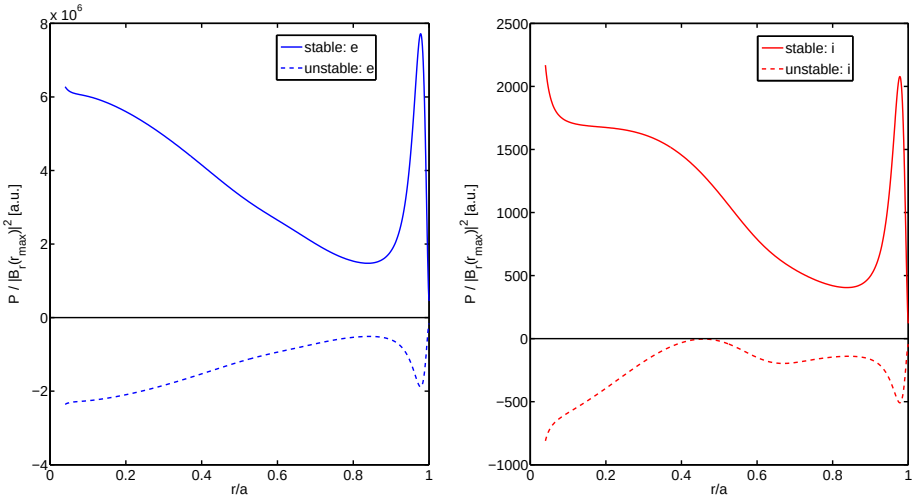

Figure 37: Power densities (normalised to the maximum value of $|B_r|^2$) dissipated to electrons (left) and to ions (right) for a stable ($V_z/V_\mathrm{A} = -0.04$) and an unstable ($V_z/V_\mathrm{A} = -0.03$) RWM and resistive wall position at $b/a = 1.4$.

impact of different sorts of particles on the mode stability can be analysed by looking at the electromagnetic power dissipated to the respective species. If total power dissipated to the electrons and ions together is positive, the mode will damp. Vice versa, if it is negative, the mode will obtain energy from the plasma particles and will grow, i.e. become unstable.

In Figure 37 shown are power densities dissipated to electrons and ions for the case of a stable (plasma rotates with $V_z = -0.04\,V_\mathrm{A}$) and an unstable ($V_z = -0.03\,V_\mathrm{A}$) RWM mode with resistive wall position at $b/a = 1.4$. While the power densities dissipated on both species have the same sign (positive for the stable and negative for the unstable mode), it is the electrons which are responsible for the RWM stability since the energy dissipated to the ions is three orders of magnitude less.

7.8 Estimate of Kinetic Code Dependence on T_e and T_i

Regarding to the temperatures from the used RFP equilibrium in Sec. 7, the remaining question concerning the influence of temperatures on the kinetic results arises. While for the MHD model only the complete temperature $T = T_\mathrm{e} + T_\mathrm{i}$ enters to the equilibrium pressure in $p = nk_BT$, the kinetic model depends on both temperature components regarding to the separately considered collisions of electrons and ions. Therefore the kinetic model is expected to be sensitive

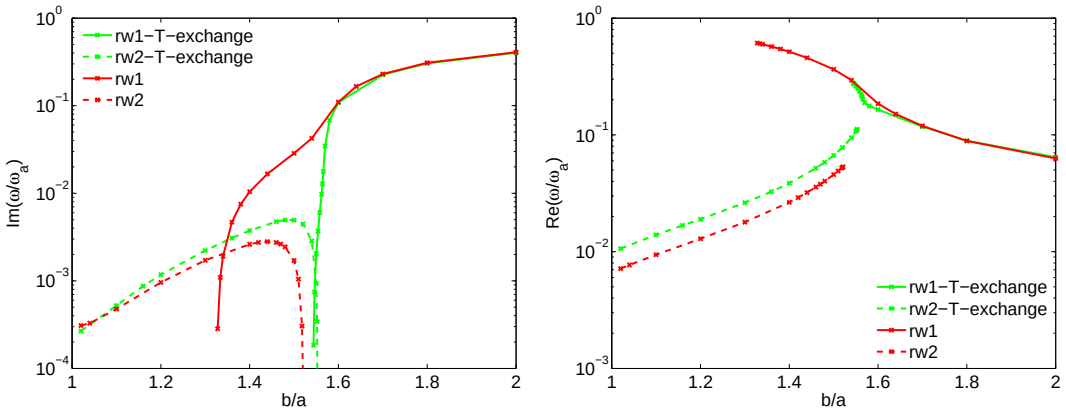

Figure 38: *left*: Normalised growth rates of the kinetic RWM from Figure 28 for two diffrent cases of T_i and T_e. Particular: $p = nk_BT = nk_B\left(T_\mathrm{e} + T_\mathrm{i}\right)$ whereas $T_\mathrm{e} = 0.6T$ and $T_\mathrm{i} = 0.4T$ and exchanged $T_\mathrm{i} <-> T_\mathrm{e}$. *right*: Normalised real parts corresponding to the left plot.

on the exchange of T_e and T_i. In the used equilibrium in Sec. 7, the ion temperature T_i is smaller than the electron temperature T_e. Both fullfill Dalton's law $p = nk_BT = nk_B\left(T_\mathrm{e} + T_\mathrm{i}\right)$ whereas $T_\mathrm{e} = 0.6T$ and $T_\mathrm{i} = 0.4T$.
Figure 38 shows the normalised growth rates and normalised real parts for the kinetic resistive wall modes *rw1* and *rw2* from Sec. 7.4 in comparison to the case with exchanged temperatures. The exchange of temperatures has a visible influence on both modes. The low frequent *rw2* has a different stabilisation position of the resistive wall, it changes from initially $b/a = 1.52$ to $b/a = 1.54$. The change in stabilisation position is much larger for the *rw1* mode, where it is shifted from initially $b/a = 1.33$ to $b/a = 1.56$. The consequence is now that there is nearly no overlapping of RWMs at resistive wall positions between $b/a = 1.33$ to $b/a = 1.52$, because both modes stabilise at approximately the same wall position.

8 Application of MHD and Kinetic Model to Tokamak Plasmas

In the following section we apply the developed kinetic and the MHD code to a set of Tokamak like profiles without reversal point.
The task of these investigations is to show that it is also possible to model and compare instabilities obtained by the kinetic and the MHD code on profiles which approximate a Tokamak configuration in cylindrical symmetry. We have developed a MATLAB program which computes profiles by analytic expressions including shape parameters to influence the gradients of the profiles. This allows to trace the frequencies of instabilities (frequency values in the complex plane), which are known for simple profile configurations, up to realistic Tokamak scales.

8.1 Calculation of Profiles

This section describes the modelling of Tokamak like profiles in cylindrical symmetry. The profiles are computed from analytic expressions based on the `tanh`-function. The equilibrium is calculated to be self-consistent, i.e. the MHD equilibrium condition from Equation (232) is satisfied.
The basic idea is that the profiles of particle density n, ion and electron temperature T_i and T_e, plasma background velocities V_z and V_Θ and current density J_z are determined by a `tanh`-function which can be varied by shape parameters aribtrarily. From these profiles it is then possible to compute all remaining profiles (e.g. magnetic and electric fields) out of the MHD equilibrium equations.
The shape parameters for the `tanh`-function represent a set of six parameters which determine the complete shape of a plasma quantity Q and are namely: the quantity value at cylinder axis Q_0, the value at cylinder wall Q_inf, plasma radius a, the degree of the curve `deg` and the shape coefficients D_min and D_max.
A `tanh`-function can then be used to compute the plasma profiles by:

$$Q = 2A\left(1 + \tanh\left(\frac{a-r}{\delta}\right)\right)^{\mathrm{deg}} + Q_\mathrm{inf}, \tag{260}$$

where Q represents one of the basic profiles mentioned above (e.g. n, T_e, etc.). Further are

$$\delta = D_\mathrm{min} + \frac{D_\mathrm{max} - D_\mathrm{min}}{r_n - r} \cdot (r - r_0), \tag{261}$$

$$A = \frac{Q_0 - Q_\mathrm{inf}}{2\tanh\left(\frac{a}{r_0} + 1\right)^{\mathrm{deg}}}. \tag{262}$$

The quantities with index zero represent the on axis values and r_n represents the cylinder wall position. In Table 3 the set of shape parameters for Profile 1 from Sec. 8.2 is shown. Table 4 shows the equilibrium parameter set for Profile 2 and Table 5 shows the shape parameter set for equilibrium Profile 3.

Profile 1	Q_0	Q_{inf}	a	deg	D_{min}	D_{max}
n	$5.0 \cdot 10^{13}\text{cm}^{-3}$	$Q_0/1e5$	50cm	5	3	20
T_i	10^4eV	$Q_0/100$	50cm	5	15	10
T_e	$7.5 \cdot 10^3\text{eV}$	$Q_0/100$	50cm	5	15	10
V_z	$10^6 \frac{\text{cm}}{\text{s}}$	$0.0 \frac{\text{cm}}{\text{s}}$	50cm	2	15	30
J_z	$1.5 \cdot 10^{11} \frac{\text{stamp}}{\text{cm}^2}$	$0.0 \frac{\text{stamp}}{\text{cm}^2}$	50cm	5	5	30

Table 3: Shape parameter set for Profile 1 from Sec. 8.2 Tokamak profiles.

Profile 2	Q_0	Q_{inf}	a	deg	D_{min}	D_{max}
n	$5.0 \cdot 10^{13}\text{cm}^{-3}$	$Q_0/1e5$	50cm	5	2	20
T_i	10^4eV	$Q_0/100$	50cm	9	2	10
T_e	$7.5 \cdot 10^3\text{eV}$	$Q_0/100$	50cm	9	2	10
V_z	$10^6 \frac{\text{cm}}{\text{s}}$	$0.0 \frac{\text{cm}}{\text{s}}$	50cm	2	15	30
J_z	$1.5 \cdot 10^{11} \frac{\text{stamp}}{\text{cm}^2}$	$0.0 \frac{\text{stamp}}{\text{cm}^2}$	50cm	5	10	30

Table 4: Shape parameter set for Profile 2 from Sec. 8.2 Tokamak profiles.

Profile 3	Q_0	Q_{inf}	a	deg	D_{min}	D_{max}
n	$5.0 \cdot 10^{13}\text{cm}^{-3}$	$Q_0/1e5$	50cm	5	2	20
T_i	10^4eV	$Q_0/100$	50cm	9	2	10
T_e	$7.5 \cdot 10^3\text{eV}$	$Q_0/100$	50cm	9	2	10
V_z	$10^6 \frac{\text{cm}}{\text{s}}$	$0.0 \frac{\text{cm}}{\text{s}}$	50cm	2	15	30
J_z	$3.0 \cdot 10^{11} \frac{\text{stamp}}{\text{cm}^2}$	$0.0 \frac{\text{stamp}}{\text{cm}^2}$	50cm	5	10	30

Table 5: Shape parameter set for Profile 3 from Sec. 8.2 Tokamak profiles.

8.2 Profile 1

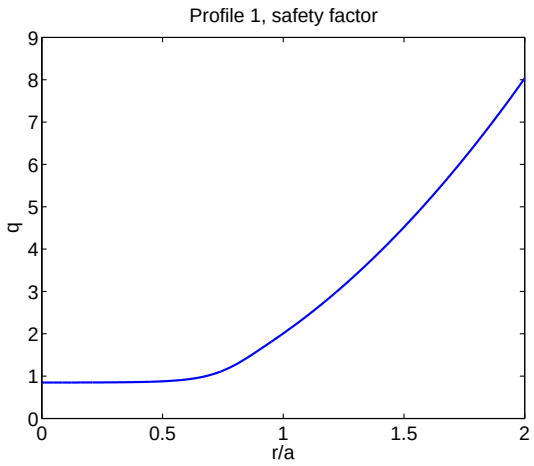

Figure 39: q-profile for Profile 1 which has $q = 1$ at $r_s/a = 0.68$ ($r_s = 34$cm) and $q_0 = 0.85$.

Profile 1 is computed analytically by MATLAB. All quantities satisfy the MHD equilibrium condition for screw pinches

$$\frac{\partial}{\partial r}\left(p + \frac{B_\theta^2 + B_z^2}{8\pi}\right) + \frac{B_\theta^2}{4\pi r} = 0 \ . \tag{263}$$

All profiles are shown in Figures 39, 40, 41, 42 and 43.

	$(r = 10^{-3}\text{cm})$	$(r = 70\text{cm})$
f_{ce} in Hz	2.2394e10	2.7585e10
f_{ci} in Hz	1.2276e7	1.5027e7
f_{pe} in Hz	6.3489e10	2.0771e8
f_{pi} in Hz	1.0457e9	3.3131e6
C_{s} in $\frac{cm}{s}$	1.0167e6	1.2157e5
V_{A} in $\frac{cm}{s}$	2.4698e8	9.6202e10

Table 6: Comparison of gyro and plasma frequencies $f_{\text{ce}} = \frac{eB}{2\pi mc}$, $f_{\text{pe}} = \frac{1}{2\pi}\sqrt{\frac{4\pi ne^2}{m_e}}$, ion sound speed $C_{\text{s}} = \sqrt{\gamma k_B \frac{T_e}{m_i}}$ and Alfven velocity $V_{\text{A}} = \frac{B}{\sqrt{4\pi n_i m_i}}$ for Profile 1.

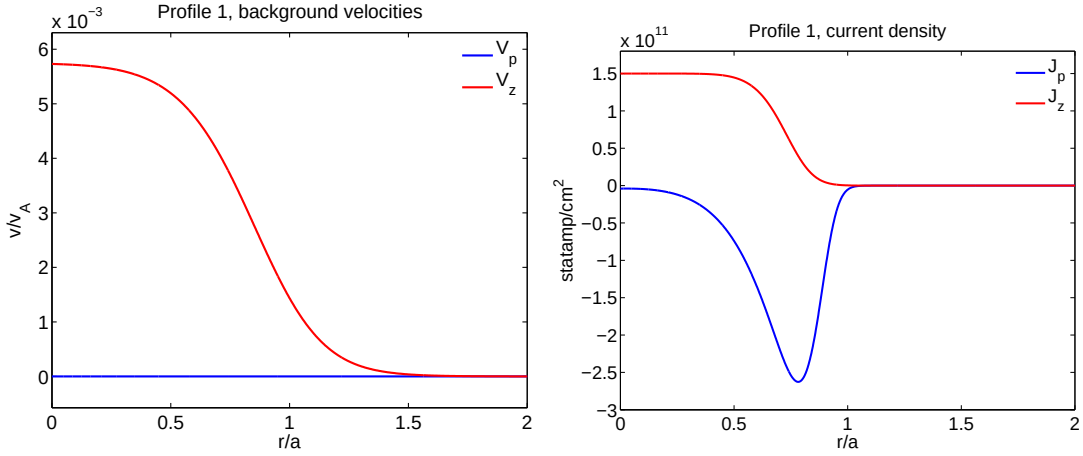

Figure 40: Profile 1 velocities v_θ and v_z normalised by the Alfven velocity as well as current components j_θ and j_z are plotted against the radius which is normalised by the plasma radius a.

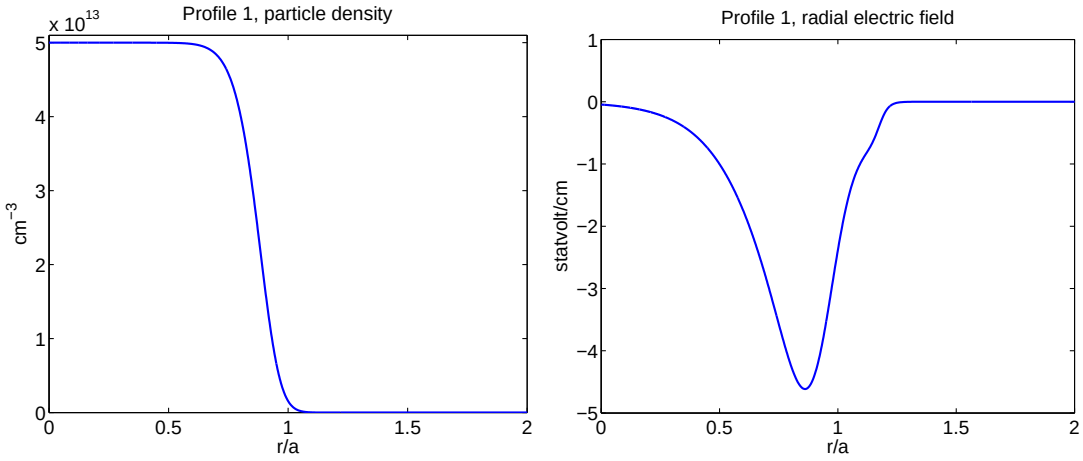

Figure 41: Profile 1 particle density and radial electric field plotted against the normalised radius.

The q-profile increases monotonically with r, the particle density at the axis is $n_0 = 5 \cdot 10^{13} \frac{1}{\mathrm{cm}^3}$, there the toroidal magnetic field is $B_{z0} = 8 \cdot 10^3$G and the poloidal magnetic field is zero, the major radius is $R = 200$cm.
The magnetic fields satisfy the *Straight Tokamak* approximation from Sec. 8.5. In Figure 44 the characteristic gyro and plasma frequencies for Profile 1 as well as Alfven and sound velocities are shown. Table 6 compares the values of the quantities from Figure 44. Therefore two radial positions ($r = 10^{-3}$cm) and

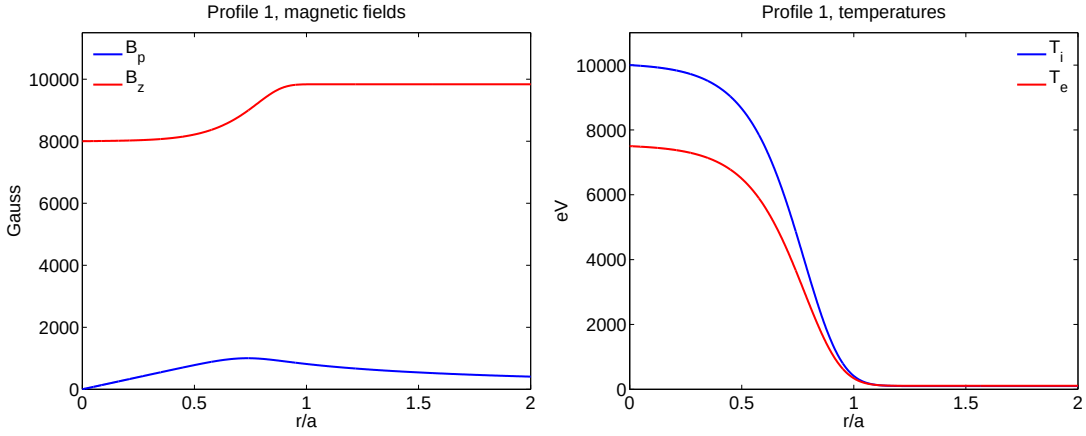

Figure 42: Profile 1 magnetic fields B_θ and B_z as well as ion and electron temperature plotted against the normalised radius.

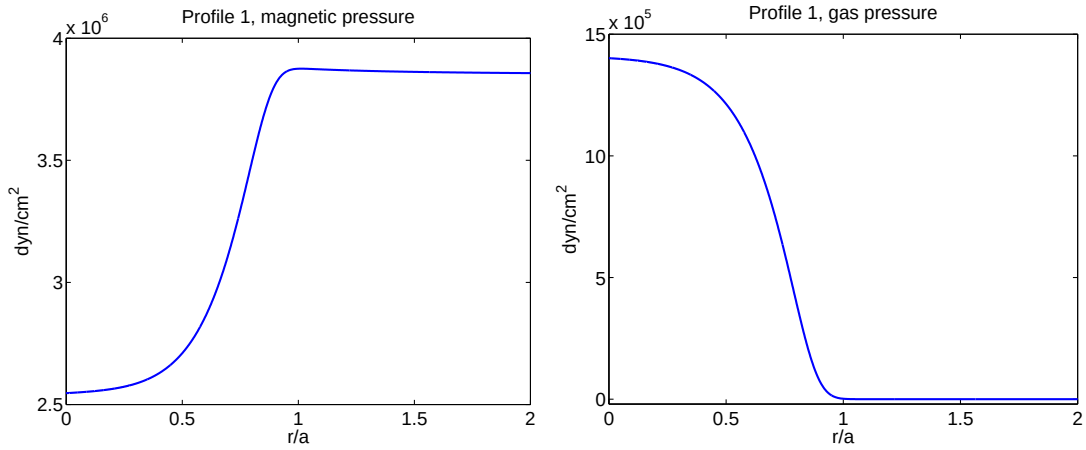

Figure 43: Profile 1 magnetic pressure $p_m = \frac{B^2}{8\pi}$ and gas pressure $p_g = nk_BT$, plotted against the normalised radius.

($r = 70$cm) are chosen. At these radial ranges all quantities from Figure 44 are nearly constant over radius r, what makes it useful to compare them there.

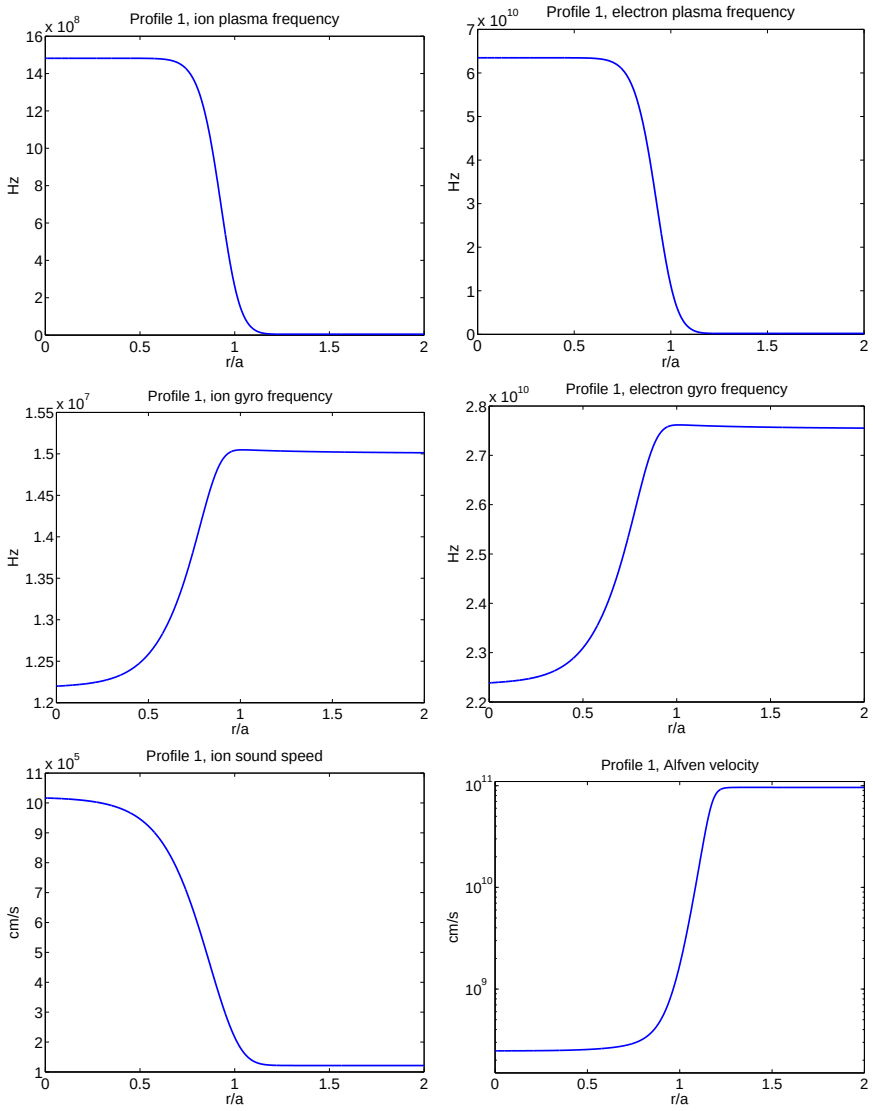

Figure 44: Profile 1 characteristic frequencies. The plots show the ion and electron plasma frequencies, the ion and electron gyro frequencies, the Alfven velocity V_{A} and the ion sound speed C_{s} plotted against the normalised radius.

8.3 Profile 2

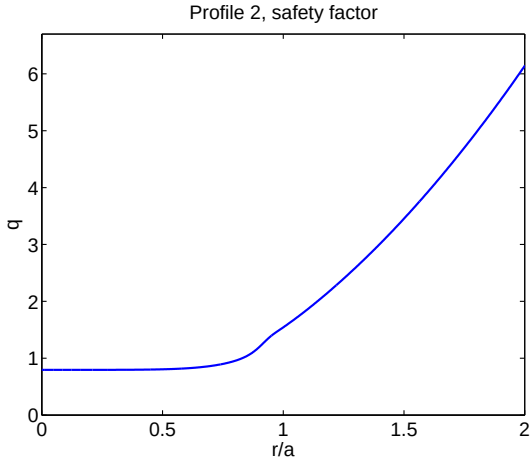

Figure 45: q-profile for Profile 2 which has $q = 1$ at $r_s/a = 0.9$ ($r_s = 45$cm) and $q = 2$ at $r_s/a = 1.16$ ($r_s = 58$cm).

Profile 2 is computed in the same way by MATLAB like Profile 1. The MHD-

	$(r = 10^{-3}\text{cm})$	$(r = 70\text{cm})$
f_{ce} in Hz	2.7993e10	3.2273e10
f_{ci} in Hz	1.5241e7	1.7581e7
f_{pe} in Hz	6.3489e10	2.0771e8
f_{pi} in Hz	1.0457e9	3.3131e6
C_{s} in $\frac{cm}{s}$	1.0167e6	1.2157e5
V_{A} in $\frac{cm}{s}$	3.0871e8	1.1251e11

Table 7: Comparison of gyro and plasma frequencies $f_{\text{ce}} = \frac{eB}{2\pi m_e c}$, $f_{\text{pe}} = \frac{1}{2\pi}\sqrt{\frac{4\pi n e^2}{m_e}}$, ion sound speed $C_{\text{s}} = \sqrt{\gamma k_B \frac{T_e}{m_i}}$ and Alfven velocity $V_{\text{A}} = \frac{B}{\sqrt{4\pi n_i m_i}}$ for Profile 2.

equilibrium from Equation (263) is satisfied as well. The particle density is $n_0 = 5 \cdot 10^{13} \frac{1}{\text{cm}^3}$, the toroidal magnetic field at the axis is $B_{z0} = 10^4$G, the poloidal field is zero there and the major radius is $R = 400$cm.
Figure 45, 46, 47, 48 and 49 show q-profile, magnetic fields, velocity and current density components, temperatures, the radial electric field, the particle density n, the magnetic pressure and the gas pressure.

Table 7 shows the characteristic frequencies and velocities at $(r = 10^{-3}\text{cm})$

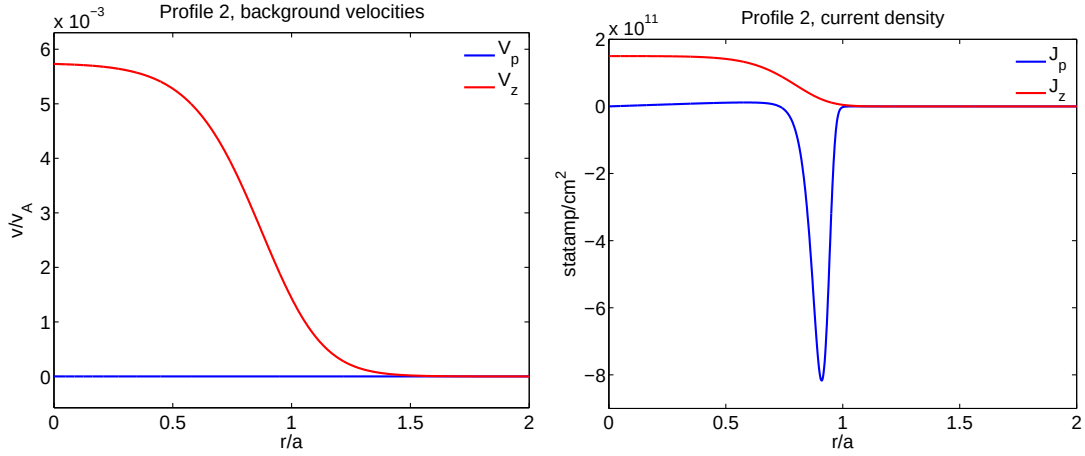

Figure 46: Profile 2 velocities v_θ and v_z normalised by the Alfven velocity as well as current density components j_θ and j_z are plotted against the normalised radius.

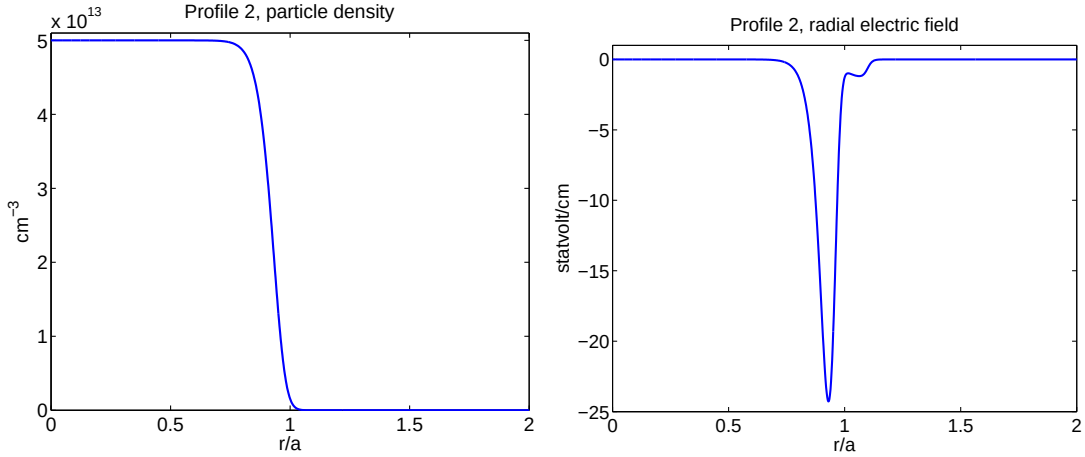

Figure 47: Profile 2 particle density and radial electric field E_r plotted against the normalised radius.

and ($r = 70$cm). It can be recognised, that ion and electron plasma frequencies (in Figure 50) differ only in steepness at plasma edge. This is a consequence of the particle density which is steeper compared to the particle density from Profile 1. In general it can be said, that the temperatures of both profile sets start from the same on axis values but Profile 1 is less steep. More differences can be estimated at the current density drops, at Profile 1 the j_θ-peak is nearly three times smaller, the E_r-component of Profile 1 is nearly five times smaller. The q-profile has an axis value $q_0 = 0.85$, crosses $q = 1$ at $r_s \approx 34$cm and

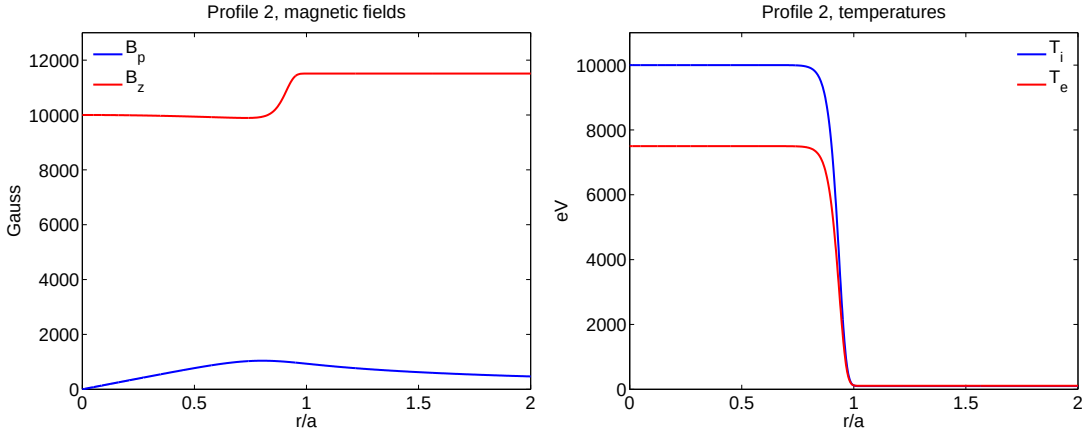

Figure 48: Profile 2 magnetic fields B_θ and B_z as well as ion and electron temperature plotted against the normalised radius.

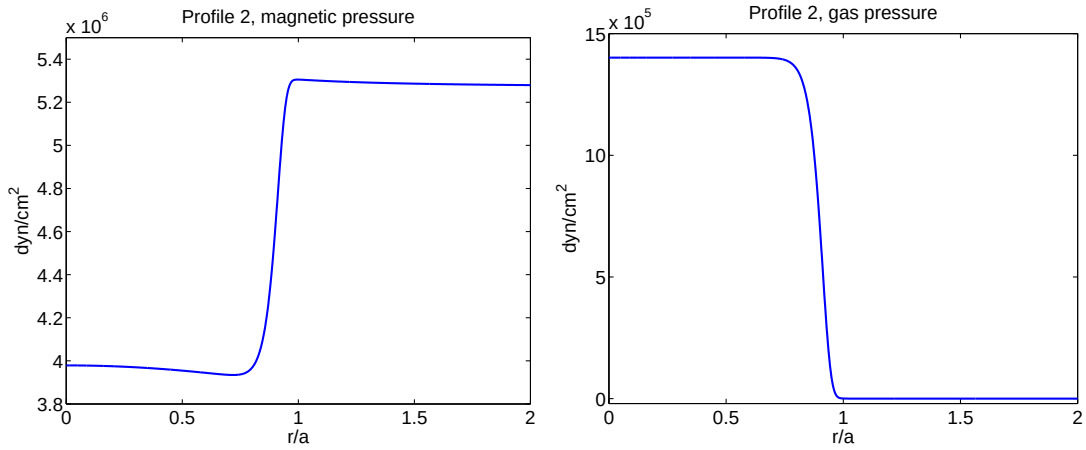

Figure 49: Profile 2 magnetic pressure $p_m = \frac{B^2}{8\pi}$ and gas pressure $p_g = nk_BT$, plotted against the normalised radius.

increases afterwards monotonically with r, see Figure 45.
The most important differences between both profile sets are the values the current peaks and E_r, the axis value of B_z and the different positions of the resonant surfaces for the q-profile.

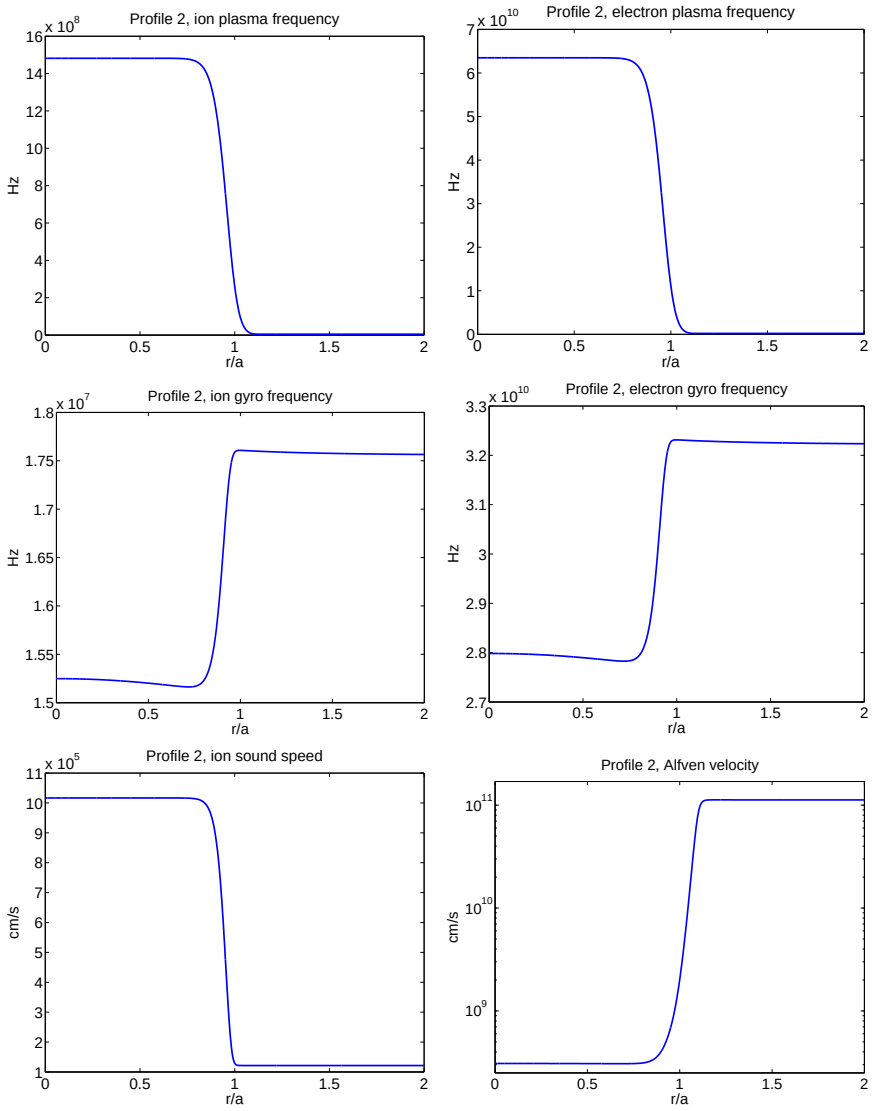

Figure 50: Profile 2 characteristic frequencies.The plots show the ion and electron plasma frequencies, the ion and electron gyro frequencies, the Alfven velocity V_{A} and the ion sound speed C_{s} plotted against the normalised radius.

8.4 Profile 3

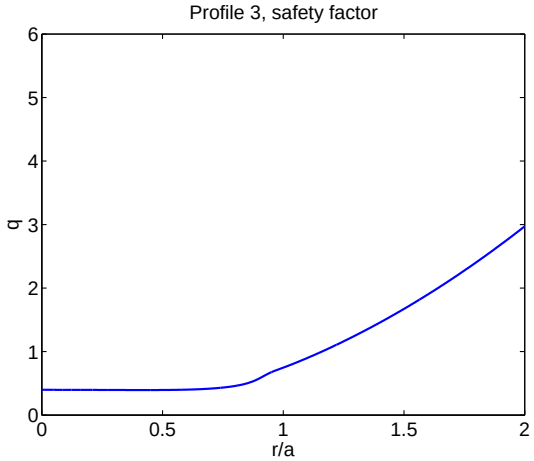

Figure 51: q-profile for Profile 3 which has $q = 1$ at $r_s/a = 1.16$ ($r_s = 58$cm).

Profile 3 is very similar to Profile 2 what means completely equal profiles of particle density n, temperatures T_e and T_i, a velocity profile V_z and a major radius of $R = 400$cm. A larger current density j_z triggers a larger gradient of the magnetic field components compared to Profile 2. This results in a safety

	$(r = 10^{-3}\mathrm{cm})$	$(r = 70\mathrm{cm})$
f_ce in Hz	2.798e10	3.1412e10
f_ci in Hz	1.5248e7	1.711e7
f_pe in Hz	6.3479e10	2.0771e8
f_ie in Hz	1.0485e9	4.685e6
C_s in $\frac{\mathrm{cm}}{\mathrm{s}}$	1.0167e6	1.2157e5
V_A in $\frac{\mathrm{cm}}{\mathrm{s}}$	3.0871e8	1.0958e11

Table 8: Comparison of gyro and plasma frequencies $f_\mathrm{ce} = \frac{eB}{2\pi m_e c}$, $f_\mathrm{pe} = \frac{1}{2\pi}\sqrt{\frac{4\pi n e^2}{m_e}}$, ion sound speed $C_\mathrm{s} = \sqrt{\gamma k_B \frac{T_e}{m_i}}$ and Alfven velocity $V_\mathrm{A} = \frac{B}{\sqrt{4\pi n_i m_i}}$ for Profile 3.

factor profile q which has a resonant surface of $q = 1$ at $b/a = 1.16$ ($r_s \approx 58$cm) what is outside the plasma, see Figure 51. Profile 3 is computed by the same equilibrium solver like Profile 2, see Table 5.
Characteristic frequencies are provided in a similar way like for Profile 1 and Profile 2, see Table 8 and Figure 56. It can be recognised, that the plots

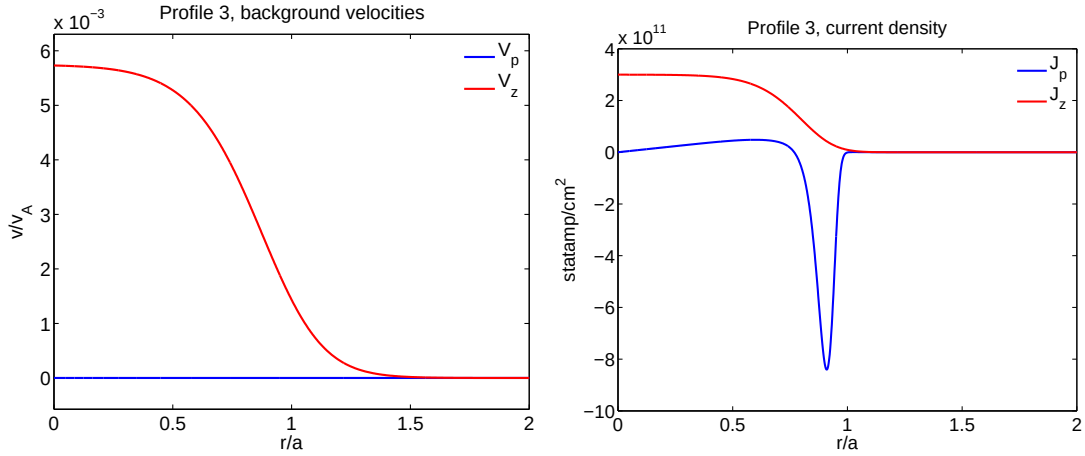

Figure 52: Profile 3 velocities v_θ and v_z normalised by the Alfven velocity as well as current density components j_θ and j_z are plotted against the normalised radius.

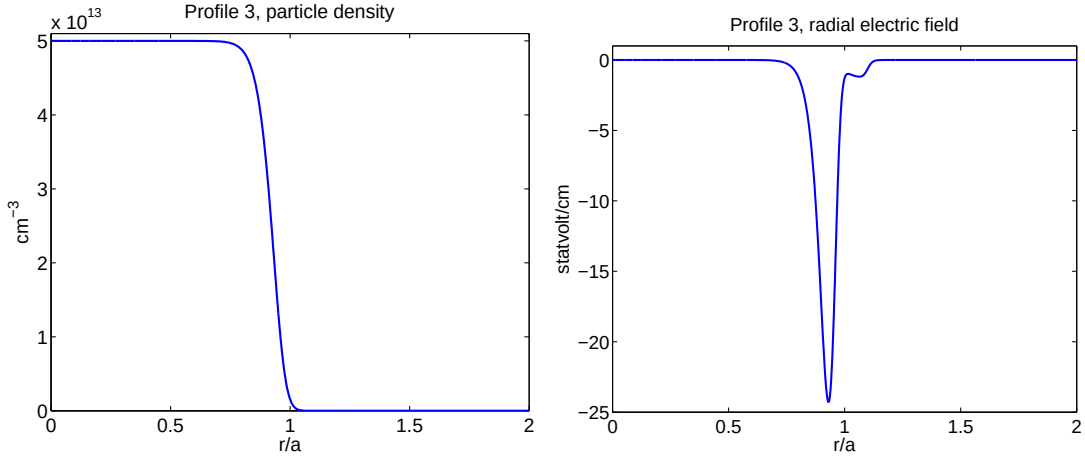

Figure 53: Profile 3 particle density and radial electric field E_r plotted against the normalised radius.

for ion sound speed C_s, electron and ion plasma frequency are equal to the corresponding quantities of Profile 2.

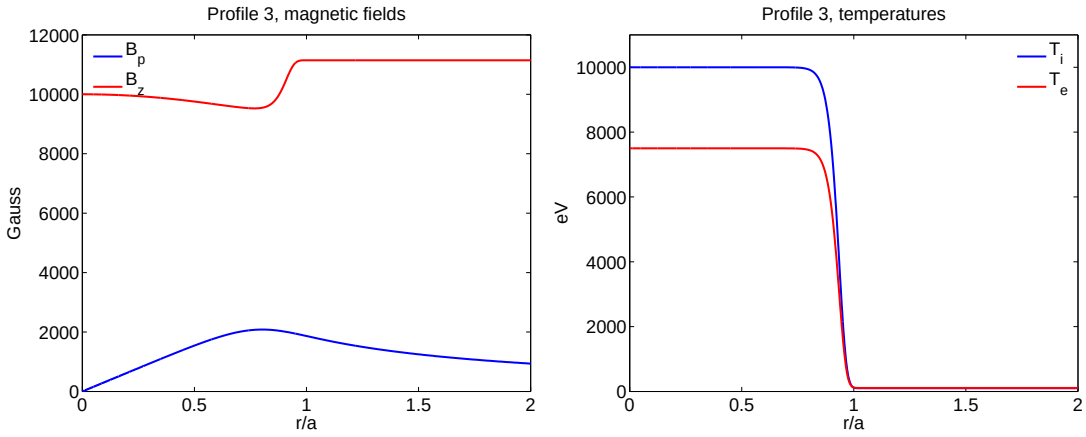

Figure 54: Profile 3 magnetic fields B_θ and B_z as well as ion and electron temperature plotted against the normalised radius.

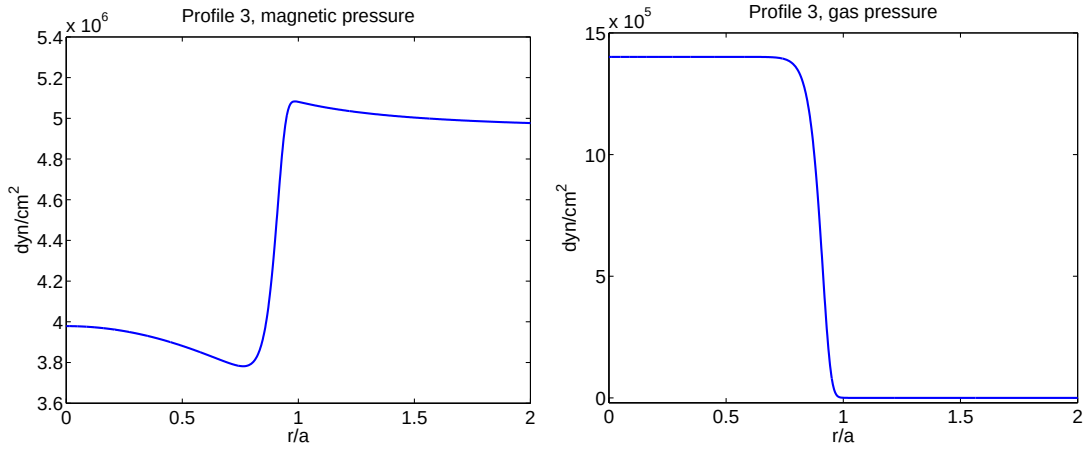

Figure 55: Profile 3 magnetic pressure $p_m = \frac{B^2}{8\pi}$ and gas pressure $p_g = nk_BT$, plotted against the normalised radius.

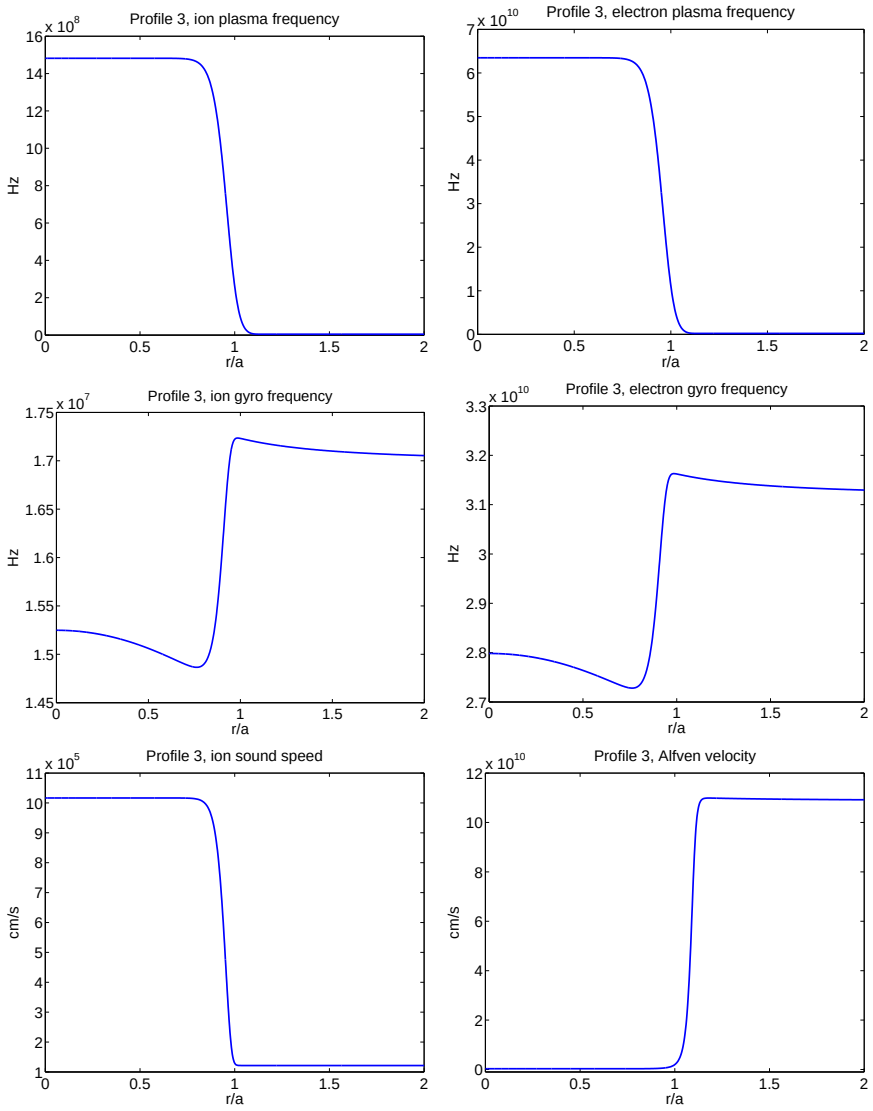

Figure 56: Profile 3 characteristic frequencies.The plots show the ion and electron plasma frequencies, the ion and electron gyro frequencies, the Alfven velocity V_{A} and the ion sound speed C_{s} plotted against the normalised radius.

8.5 Expected Behaviour of MHD Modes

For the investigation of modes with $|m| > 1$, the safety factor $q(r)$ plays an important role regarding to the question if the plasma configuration is stable due to p- and j-driven modes or not.
In a cylindrical screw-pinch configuration where the magnetic fields satisfy the *Straight Tokamak* conditions:

$$\boxed{\frac{B_\theta}{B_z} \sim \epsilon}, \tag{264}$$

with $\epsilon = \frac{r}{R}$ the Tokamak aspect ratio and

$$\frac{8\pi p}{B_z^2} \sim \epsilon^2 \quad (\textit{ohmically heated}) \;\; ; \qquad \frac{8\pi p}{B_z^2} \sim \epsilon \quad (\textit{high } \beta \textit{ tokamak}) \, .$$

External and internal current driven modes turn out to be the most dangerous instabilities, see Ref. [11]. Pressure driven modes are less dangerous, they can be investigated by the Suydam criterion and are not focused here.

Internal Current Driven Modes

Internal modes are defined by the position of the resonant surface r_s, where $\mathbf{k} \cdot \mathbf{B} = 0$ and the safety factor

$$q = \frac{|m|}{n} \; ; \; at \;\; r = r_s \; . \tag{265}$$

An analytic expansion of the energy principle $\delta W = \delta W_0 + \delta W_2 + ...$ with $\delta W_n \sim \epsilon^n$ is needed for the screw pinch case whereas an unstable contribution requires $\delta W_i < 0$, see Sec. 5.1
In Ref. [32] it was shown that the first nonvanishing contribution is

$$\frac{\delta W_2}{W_0} = \frac{1}{a^2} \int_0^a \left(\frac{n}{m} - \frac{1}{q} \right)^2 \left[r^2 \xi'^2 + \left(m^2 - 1 \right) \xi^2 \right] r \mathrm{d}r, \tag{266}$$

where $W_0 = \frac{\pi a^2 B_0^2}{2R}$ and a is the plasma radius. For arbitrary n and $\boxed{m \geq 2}$ the integrand never vanishes and is positive.
$\Rightarrow \;\; \delta W_2 > 0$ and internal modes are stable.
The remaining case is an arbitrary n with $\boxed{m = 1}$; there the second integrand vanishes and the contribution becomes stable if no resonant surface is present, what means $q \neq 1$.
The next contribution term was derived in Ref. [31] for $n = 1$,

$$\frac{\delta W_4}{W_0} = \frac{\xi_0^2}{a^2} \int_0^{r_s} \left[r\beta' + \frac{r^2}{R^2} \left(1 - \frac{1}{q} \right) \left(3 + \frac{1}{q} \right) \right] r \mathrm{d}r \; . \tag{267}$$

If a resonant surface with $q = 1$ exists inside the plasma, both pressure and current contribution terms make $\delta W_4 < 0$, what is destabilising. The p-gradient effects become important only in high *beta* regimes, see Ref. [11]. In other words, the $m = 1$ instability for internal modes is a weak instability resulting from a higher δW-expansion term and vanishes if the resonant surface is removed, either by wall stabilisation or by choosing the q-value at the axis (at $r = 0$)

$$q_0 > 1 \; . \tag{268}$$

External Current Driven Modes

External modes are even stronger in energetic release and are defined by the resonant surface being positioned in the vacuum region outside the plasma column. The analysis of unstable contributions to the energy principle in Ref. [32] returned

$$\begin{aligned} \frac{\delta W_2}{W_0} = \frac{1}{a^2} \int_0^a \left(\frac{n}{m} - \frac{1}{q} \right)^2 \left[r^2 \xi'^2 + \left(m^2 - 1 \right) \xi^2 \right]] r \mathrm{d}r + \\ + \xi_a^2 \left[\left(\frac{n}{m} - \frac{1}{q_a} \right) \left(|m| \left(\frac{n}{m} - \frac{1}{q_a} \right) + \frac{n}{m} + \frac{1}{q_a} \right) \right] . \end{aligned} \tag{269}$$

Further considerations about the minimising conditions for δW, (e.g. by choosing $\xi(r) = \xi_a \left(\frac{r}{a} \right)^{m-1}$ with a monotonically increasing $q(r)$) yield modes (m, n) unstable for

$$\boxed{\frac{m-1}{n} \leq q_a \leq \frac{m}{n}}, \tag{270}$$

what means that a resonant surface lies outside of the plasma. In Ref. [11] it was mentioned, that instabilities with mode numbers $m > 1$ make much more complicated constraints on the plasma background profiles than modes with $m = 1$. So current and pressure gradients in the vicinity of the plasma surface play an important but yet not fully understood role in triggering instabilities, an investigation of that was given in Ref. [37].
An exemplary MHD investigation of higher m modes in cylindrical geometry was performed in Ref. [9] where instabilities of $(m, n) = (2, 1)$ were found for plasma profiles, for which the pressure profile at plasma edge has a step to zero, see Figure 57. This step triggers a destabilising term in the energy principle δW and produces an external $m = 2$ instability. The goal of the following investigations is to run computations for $m \geq 1$ by kinetic and MHD approach.

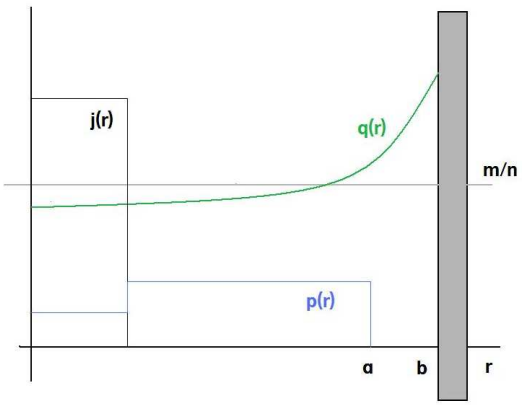

Figure 57: Profiles from Ref. [9] where p has a destabilising step at the plasma edge a. The q-profile crosses resonance $\frac{m}{n}$ inside the plasma. A perfectly conducting wall is placed at $r = b$.

8.6 Method of Computation

Regarding to instabilities with $|m| > 1$, special care has to be paid on the shape of the profiles, because the occurence of such instabilities is very sensitive on profile shapes, see Ref. [9]. For symmetry reasons, the investigations discussed in the following chapters use negative m numbers. In the KiLCA-code a definition of the q-profile like $q = \frac{-m}{n}$ is used, what differs in sign of m from the original case in Equation (265). This is just because of the toroidal direction, which is defined to be opposite in the code. To keep a positive q profile, the m values have to be negative if $n > 0$.
Computations for Profile 1 returned no instabilities for $m > 1$ modes, but only for $m = 1$, for both kinetic as well as for MHD. The drop in pressure and current mentioned in Ref. [9] and discussed in Sec. 8.5, introduce the idea to make the profiles of the background more steep at the plasma edge to trigger a destabilising plasma configuration there.
As it can be seen from the discussed density profile in Profile 1 and Profile 2, the densities have a steep drop at $r \approx 50$cm, where Profile 2 is steeper than Profile 1. According to Figure 58, always two zones are used for computation. In the used configuration the zone interface is always set to $r_{\mathrm{A}} = 55$cm, what is the estimated plasma edge and what coincides with the particle density drop (see Figure 41). The ideal wall is positioned at $r_{\mathrm{w}} = 100$cm.

Ideal MHD Approach

The inner zone $r\epsilon\,[0, r_{\mathrm{A}}]$ is treated as ideal MHD zone, and the outer region $r\epsilon\,[r_{\mathrm{A}}, r_{\mathrm{w}}]$ between plasma edge and the ideal conducting wall at r_{w} is treated as vacuum. Several other plasma profiles have been checked using different zone types (vacuum or plasma). So far the two zone *MHD-vacuum* configuration (see Figure 58) with plasma Profile 2 is the only MHD case which returns results for modes $|m| > 1$, Profile 1 gives only $m = -1$ results. Also different positions of the *plasma-vacuum* interface were checked. Once the interface is placed at a density which represents an acceptable vacuum, the resulting frequencies of the found instabilities change less than 5%, what is no significant change. So the plasma radius is placed at $r_{\mathrm{A}} = 55\mathrm{cm}$ what ensures the case of vacuum.

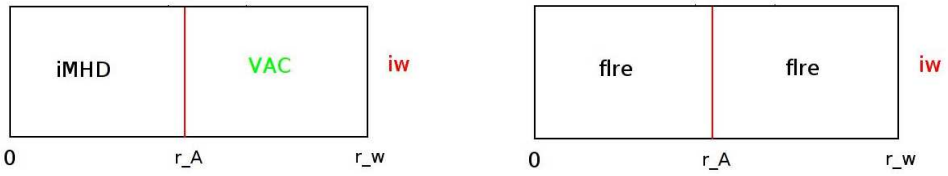

Figure 58: Schematic modell of two zones which are used to compute MHD and kinetic results for Profile 1, Profile 2 and Profile 3. Between the plasma edge at r_{A} and the ideal wall at r_{w} the MHD case uses a vacuum zone and the kinetic case uses a plasma zone.

Kinetic Approach

For the kinetic approach the splitting of the cylinder in radial zones remains the same like for the MHD case, Figure 58. The difference is now, that no vacuum zone is used and a plasma zone is applied there. This is done because the kinetic model is expected to run more stable if the whole cylinder is treated as medium.

mode	m	n	Re(f) in Hz	Im(f) in Hz	type
1	-1	1	0	2.85794779026e4	MHD
2	-1	1	0	-2.85794779026e4	MHD
3	-1	1	0	3.47100254113e3	MHD
4	-1	1	0	-3.47100254116e3	MHD
5	-1	1	-1.76400298585e4	3.74525676191e4	KiN
6	-1	1	-1.23640183093e4	-3.91414857516e3	KiN
7	-1	1	1.60796481388e6	-1.53712511445e1	KiN
8	-1	1	-2.18950066542e4	1.54056177065e5	KiN

Table 9: Frequencies of eigenmodes for modes with $m = -1$ for Profile 1 .

8.7 Results for Profile 1, $m = -1$

For both the kinetic and the MHD zones a zone-to-zone interface at $r_{\mathrm{A}} = 55$cm and an ideal wall position at $r_{\mathrm{w}} = 100$cm are used. This section shows results for kinetic and ideal MHD results of the configuration, mentioned in Sec. 8.5. A kinetic code with the collision operator from Sec. 3.2 is used to compute the eigenmodes. Table 9 lists the found kinetic and ideal MHD modes for $m = -1$, $v_z = 0$, $r_{\mathrm{w}} = 100$cm and $r_{\mathrm{A}} = 55$cm. A solution for an eigenmode is found if the value of determinant is 10 orders of magnitude less than nearby. Figure 59 shows a comparison of the MHD eigenfunctions of mode 1 and mode 3 from Table 9.
Figure 60 shows a comparison of B_r for MHD mode 1 and mode 3 with kinetic modes 5 and 8 from Table 9.
The curves for B_r are normalised by B_0, which is the complex value for B_r^0 at $r_0 = 20$cm. After normalisation, the MHD case remains pure real and the kinetic case results in a real and imaginary part of $\frac{B_r}{B_r^0}$. It can be clearly estimated that the normalised curves cross zero at the resonant surface for $m = -1$ at $r_s \approx 34$cm. The ideal MHD code found four modes, two stable and two unstable. For the kinetic root it is in principle possible to find more than four roots.

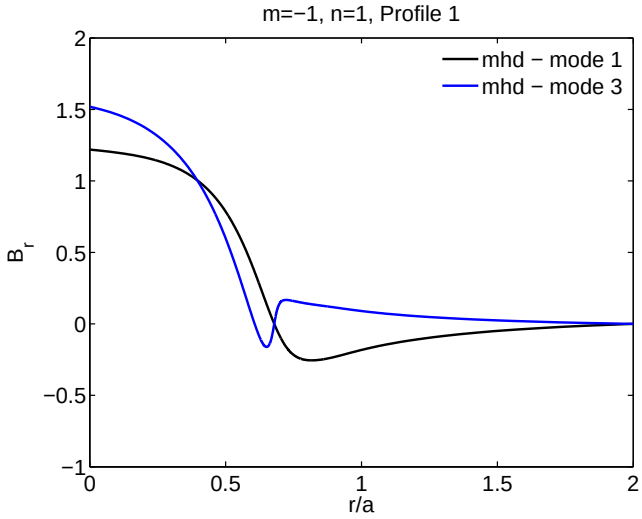

Figure 59: Radial magnetic field B_r (Fourier coefficients) for Profile 1 normalised at $r_0 = 20$cm. Shown are the normalised MHD solutions for mode 1 and mode 3 from Table 9 plotted against the normalised radius.

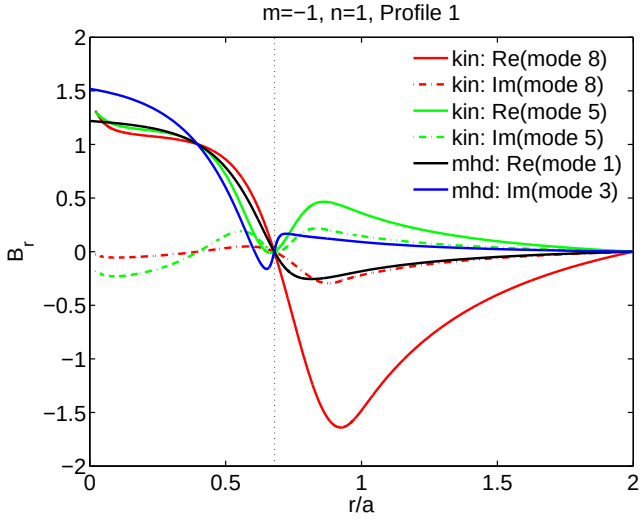

Figure 60: Radial magnetic field B_r (Fourier coefficients) for Profile 1 normalised at $r_0 = 20$cm. Resonance at $r_s \approx 34$cm (dotted). Shown are the normalised MHD solutions mode 1 and mode 3 in comparison to the kinetic modes 5 and 8.

8.8 Results for Profile 2, $m = -1$ and $m = -2$

Table 10 shows resulting frequencies for eigenmodes with $m = -1$ and $m = -2$. Using Profile 2, it is possible to find an unstable mode for $m = -1$ by both kinetic and MHD code, see mode 1 and mode 2 in Table 10. It is possible to

mode	m	n	Re(f) in Hz	Im(f) in Hz	type
1	-1	1	0	3.9101334822214e3	MHD
2	-1	1	-1.8133135503843e3	7.92362550836761e3	KiN
3	-2	1	0	1.1896940113354e4	MHD
4	-2	1	-1.0769811356593e5	2.9711995682725e4	KiN
5	-2	1	-1.3184264271102e5	2.5539645015256e4	KiN

Table 10: Frequencies of eigenmodes with $m = -1$ and $m = -2$ for Profile 2.

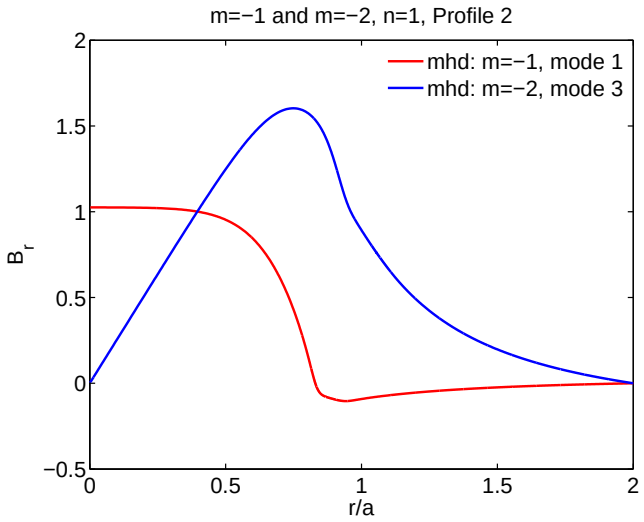

Figure 61: Radial magnetic field B_r (Fourier coefficients) normalised at $r_0 = 20$cm. Resonance at $r_s \approx 34$cm for $m = -1$ and $r_s \approx 58$cm for $m = -2$. Two MHD modes 1 and mode 3 for $m = -1$ and $m = -2$ from Table 10 are plotted against the normalised radius.

find one MHD result and two kinetic for $m = -2$ (see Table 10).
Figure 61 displays the normalised $\mathrm{Im}(B_r)$ curves for the two MHD modes $m = -1$ and $m = -2$ (from Table 10: mode 1 and mode 3). The normalised B_r curves of the kinetic mode 4 and mode 5 are compared with the MHD mode 3

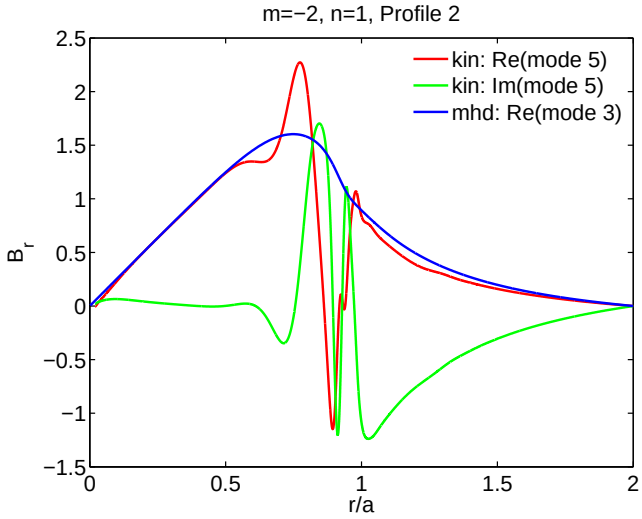

Figure 62: Radial magnetic fields B_r (Fourier coefficients) for Profile 2 from Table 10 normalised at $r_0 = 20$cm are plotted against the normalised radius. Resonance at $r_s \approx 58$cm for $m = -2$. The MHD mode 3 is compared to the kinetic mode 5 from Table 10.

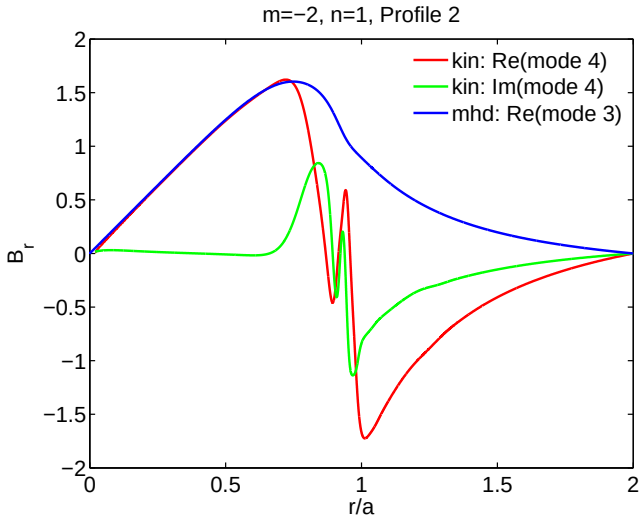

Figure 63: Radial magnetic fields B_r (Fourier coefficients) for Profile 2 from Table 10 normalised at $r_0 = 20$cm are plotted against the normalised radius. Resonance at $r_s \approx 58$cm for $m = -2$. The MHD mode 3 is compared to the kinetic mode 4 from Table 10.

for $m = -2$ in Figure 62 and Figure 63. Especially in the inner plasma region, where $r < 30$cm, the MHD curves shows a good correspondance to the kinetic

curves. In the outer regions, outside the plasma radius r_{A}, the kinetic mode 5 corresponds much better to the MHD mode 3 than the kinetic mode 4.

8.9 Results for Profile 3, $m = -1$

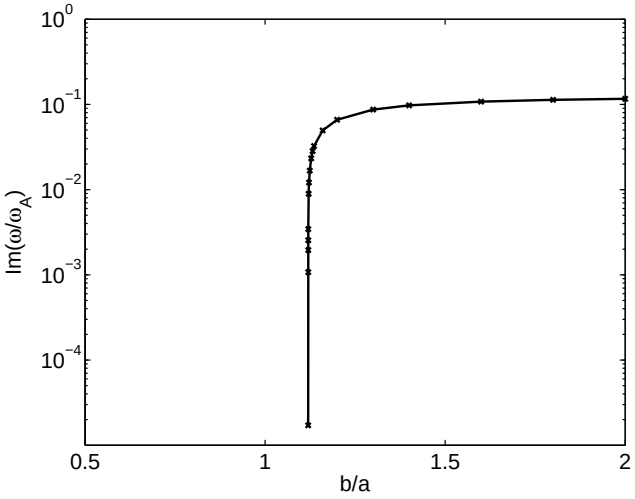

Figure 64: Normalised growth rates (normalised by $\omega_{\mathrm{A}} = 6.174 \cdot 10^9 \mathrm{s}^{-1}$) for different positions of the ideal wall modelled by the MHD-model using Profile 3 with mode numbers $(m, n) = (-1, 1)$. The mode becomes stable ($\mathrm{Im}\,(\omega) < 0$) when the wall crosses the resonance position $q = \frac{-m}{n} = 1$ at $r_s/a = 1.16$.

Profile 3 has been investigated only by the MHD model under the application of an ideal wall case.
It is interesting to investigate the influence of the wall position on this kind of profiles where the resonant surface $q = \frac{-m}{n} = 1$ lies outside the plasma. The results are normalised by

$$\omega_{\mathrm{A}} = \frac{V_{\mathrm{A}}}{a} = \frac{1.9833 \cdot 10^9 \frac{\mathrm{cm}}{\mathrm{s}}}{50\mathrm{cm}} = 6.174 \cdot 10^9 \mathrm{s}^{-1}, \tag{271}$$

where $V_{\mathrm{A}} = 1.9833 \cdot 10^9 \frac{\mathrm{cm}}{\mathrm{s}}$ is the Alfven velocity at the plasma edge and $a = 50\mathrm{cm}$ is the plasma radius.
Figure 64 shows a normalised ideal wall growth rate in dependence of the wall position. The frequency of the mode with $(m, n) = (-1, 1)$ at $b/a = 2.0$ is listed in Table 11.
The mode becomes stabilised at the moment when the ideal wall crosses the position of the resonant surface $q = \frac{-m}{n} = 1$ at $r_s/a = 1.16$.

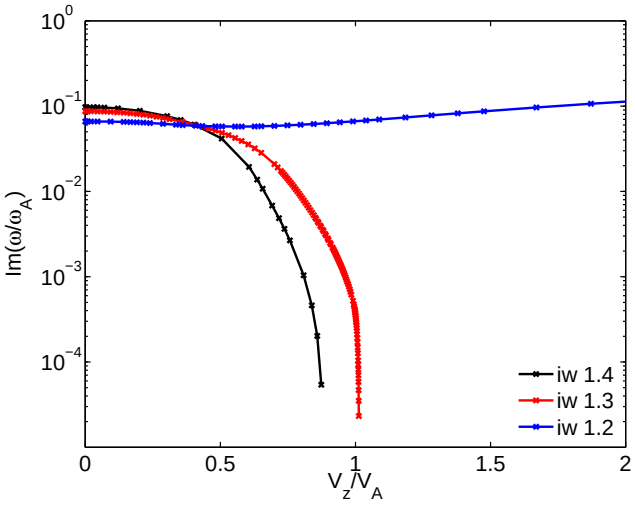

Figure 65: Normalised growth rates (normalised by $\omega_{\mathrm{A}} = 6.174 \cdot 10^9 \mathrm{s}^{-1}$) of the ideal wall mode $(m, n) = (-1, 1)$ from Figure 64 in dependence of the toroidal plasma rotation V_z. Plotted are three cases of ideal wall positions.

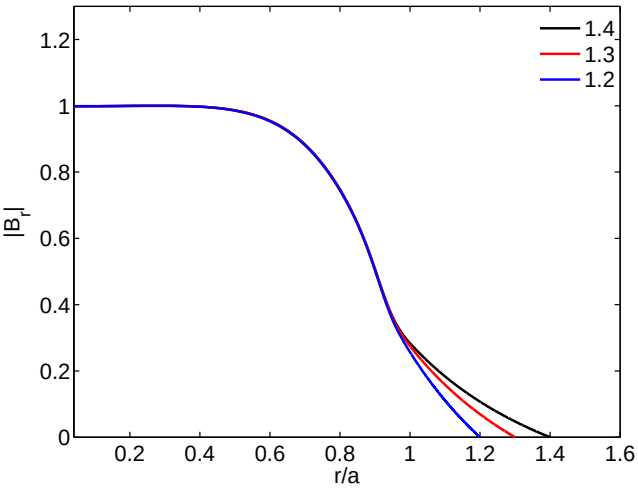

Figure 66: Absolute value of the normalised B_r for the three ideal wall configurations from Figure 65 at $V_z = 0$. The eigenfunctions reach zero at the particular ideal wall position. *red:* $b/a = 1.3$, *blue:* $b/a = 1.2$, *black:* $b/a = 1.4$,

In Figure 64 the toroidal background rotation is set to zero. For the case that a toroidal plasma velocity profile V_z (like shown in Figure 52) is considered, it has been shown that different positions of the ideal wall show a completely different growth rate evolution while the plasma rotation V_z is increased. Figure 65 shows the normalised growth rates of the mode discussed in Figure 64 at the three different positions of the ideal wall, $b/a = 1.2$, $b/a = 1.3$ and $b/a = 1.4$, for increasing toroidal rotation V_z. The rotation velocity is expressed as fraction of the Alfven velocity value at plasma edge. It can be seen that the stabilisation threshold of V_z is lower for lager values of $\frac{b}{a}$. Further there exists a limit for the ideal wall position, below which the mode cannot be stabilised by rotation any more, e.g. at $b/a = 1.2$ where no stabilisation is visible.

Absolute values of the normalised eigenfunctions $|B_r|$ are shown in Figure 66.

m	n	Re(f) in Hz	Im(f) in Hz	b/a
-1	1	0	$1.14314 \cdot 10^5$	2.0
-1	1	0	$9.56377 \cdot 10^4$	1.4
-1	1	0	$8.54002 \cdot 10^4$	1.3
-1	1	0	$6.49238 \cdot 10^4$	1.2

Table 11: Frequencies of eigenmodes with $m = -1$ and $n = 1$ and different positions of the ideal wall b/a for Profile 3 with $V_z = 0$.

The curves show growth rates of modes with $(m, n) = (-1, 1)$ at ideal wall positions $b/a = 1.4$; 1.3; 1.2, with $V_z = 0$. The corresponding frequency values are listed in Table 11.

9 Conclusions

The present thesis introduces a kinetic model to study global plasma instabilities and compares the results with MHD modelling. In particular, resistive wall mode stabilisation is investigated in cylindrical geometry for a RFP plasma configuration by both models. For this purpose, the code KiLCA, originally developed for treating the plasma response due to external magnetic field perturbation (RMPs), is adapted to deal with stable and unstable global eigenmodes that are determined by plasma, vacuum and vessel parameters. The MHD and kinetic models including equilibrium plasma flows are derived and adapted to the KiLCA code. For modelling collisions, a Coulomb collision operator of Fokker-Planck type is used which conserves the charge also with respect to Galileian transformations. Solutions of Maxwell equations for different regions like plasma region, vacuum and resistive medium are derived and implemented in the code. The code can be used to study resistive wall modes in reversed field pinch and Tokamak plasmas.

The external kink mode stabilised in ideal MHD by an ideal wall is found also in the kinetic modelling with comparable growth rates. The wall position for complete stabilisation of the ideal mode is less than predicted by MHD. A resistive wall mode with growth rate on the resistive time scale is also seen in the kinetic description. In analogy to MHD, this mode was found to be stabilised by toroidal plasma motion. However, stabilisation in the kinetic modelling is sensitive to the direction of the rotation and, in the present case, only negative V_z values have led to mode stabilisation. Stabilising rotation velocities are found somewhat smaller when compared to MHD. Finally, it was not possible to see the complete stabilising window predicted by MHD, that means that no instability for very close positions of the resistive wall has been found. It is found, that for some wall positions the ideal wall kink can be stabilised by plasma rotation as well. There seems to exist a critical position of the ideal wall, above which an increase in toroidal rotation does not lead to stabilisation of the growth rates any more.

It was possible to show that the shape of the toroidal velocity profiles at plasma edge has a visible effect on the rotational stabilisation of the resistive wall modes. Further, an exchange of the ion and the electron temperature profiles shows a shift of the growth rate values of the resistive wall modes. This confirms, that the kinetic model is sensitive on electron and ion motion (collisions).

Eigenmodes for different mode numbers resulting from MHD and kinetic modelling for Tokamak profiles turned out to be more different than for RFP profiles. The kinetic effects responsible for these differences have still to be studied in more detail.

References

[1] V. Antoni, D. Merlin, S. Ortolani, and R. Paccagnella. MHD stability analysis of force-free reversed field pinch configurations. *Nucl. Fusion*, 26(12):1711–1717, 1986.

[2] T. D. Arber and D. F. Howell. The effect of sheared axial flow on the linear stability of the Z-pinch. *Phys. Plasmas*, 3(2):554–560, 1996.

[3] A. Bondenson, R. Iacono, and A. Bhattacharjee. Local magnetohydrodynamic instabilities of cylindrical plasma with sheared equlibrium flow. *Phys. Fluids*, 30(7):2167–2180, 1987.

[4] A. Bondenson and D. J. Ward. Stabilization of external modes in Tokamaks by Resistive Walls and Plasma Rotation. *Phys. Rev. Lett.*, 72(17):2709–2712, 1994.

[5] J. D. Callen. Draft: Fundamentals of Plasma Physics. *University of Wisconsin-Madison*, 2003.

[6] M. S. Chu and M. Okabayashi. Stabilization of the external kink and the resistive wall mode. *Plasma Phys. Control. Fusion*, 52:123001, 2010.

[7] R. Dendy. Plasma Physics: An Introductory Course. *Cambridge University Press*, 1, 1993.

[8] European Fusion Development Agreement EFDA. online material. *EU Fusion Programme*, 2011.

[9] J. M. Finn. Stabilization of ideal plasma resistive wall modes in cylindrical geometry: The effect of resistive layers. *Phys. Plasmas*, 2(10):3782–3791, 1995.

[10] R. Fitzpatrick and A. Y. Aydemir. Stabilization of the resistive shell mode in Tokamaks. *Nucl. Fusion*, 36(1):11–38, 1996.

[11] J Freidberg. Ideal Magnetohydrodynamics. *Plenum Press, New York*, 1987.

[12] A. M. Garofalo, T. H. Jensen, and E. J. Strait. Semiquantitative analysis of feedback systems for resistive wall modes. *Phys. Plasmas*, 9(11):4573–4583, 2002.

[13] J. P. Goedbloed and P. H. Sakanaka. New approach to magnetohydrodynamic stability: I. A practical stability concept. *Phys. Fluids*, 17(5):908, 1974.

[14] S. C. Guo, J. P. Freidberg, and R. Nachtrieb. Stability of resistive wall modes in reversed field pinches with longitudinal flow and dissipative effects. *Phys. Plasmas*, 6(10):3868–3877, 1999.

[15] T. C. Hender. Chapter 3: MHD stability, operational limits and disruptions. *Nucl. Fusion*, 47:128–202, 2007.

[16] M. F. Heyn, I. B. Ivanov, S. V. Kasilov, and W. Kernbichler. Kinetic modeling of the interaction of rotating magnetic fields with a radially inhomogeneous plasma. *Nuclear Fusion*, 46(3):159–169, 2006.

[17] M. F. Heyn, I. B. Ivanov, S. V. Kasilov, and W. Kernbichler. Kinetic estimate of the shielding of resonant magnetic field perturbations by the plasma in DIII-D. *Nuclear Fusion*, 48:024005, 2008.

[18] G. T. A. Huysmans. ELMs: MHD instabilities at the transport barrier. *Plasma Phys. Control. Fusion*, 47:B165, 2005.

[19] I. B. Ivanov. PhD-Thesis. 2005.

[20] I. B. Ivanov, M. F. Heyn, S. V. Kasilov, and W. Kernbichler. Kinetic linear model of the interaction of helical magnetic perturbations with cylindrical plasmas. *Phys. Plasmas*, 18(2):022501, 2011.

[21] I. B. Ivanov, S. V. Kasilov, W. Kernbichler, and M. Heyn. On the relation between plasma rotation induced by low-frequency resonant magnetic perturbation and transport in ergodic magnetic fields. *JETP Letters*, 86(6):364–367, 2007.

[22] Yueqiang Liu, A. Bondenson, Y. Gribov, and A. Polevoi. Stabilisation of resistive wall modes in ITER by active feedback and toroidal rotation. *Nucl. Fusion*, 44:232–242, 2004.

[23] S. M. Mahajan and C. Y. Chen. Plasma kinetic theory in action-angle variables. *Phys. Fluids*, 28(12):3538–3545, 1985.

[24] G. Mc Cracken. Plasma Surface Interactions. *45th Culham Plasma Physics Summer School*, 2008.

[25] D. Merlin, S. Ortolani, R. Paccagnella, and M. Scapin. Linear resistive magnetohydrodynamic stability analysis of reversed field pinch configurations at finite beta. *Nucl. Fusion*, 29(7):1153–1160, 1989.

[26] M. Mulec, I. B. Ivanov, M. F. Heyn, and W. Kernbichler. Kinetic versus ideal magnetohydrodynamic modelling of the resistive wall mode in a reversed field pinch plasma. *Phys. Plasmas*, 19(3):032502, 2012.

[27] Plasma-Online-Lectures. Lecture 8.

[28] V. D. Pustovitov. Comparison of RWM feedback systems with different input signals. *Plasma. Phys. Control. Fusion*, 44(3):295–299, 2002.

[29] E. E. Reis. Structural design of the DIII-D Radiative Divertor. *SOFT-1996, Conference Paper*, pages 1–4, 1996.

[30] J. A. Robinson. High-β diffuse pinch configuration. *Plasma Phys.*, 13:439, 1971.

[31] M. N. Rosenbluth, R. Y. Dagazian, and P. H. Rutherford. Nonlinear properties of the internal $m = 1$ kink instability in the cylindrical Tokamak. *Phys. Fluids*, 16(11):1894–1902, 1973.

[32] V. D. Shafranov. Hydromagnetic stability of a current-carrying pinch in a strong longitudinal magnetic field. *Sov. Phys. -Tech.*, 15(2):175–183, 1970.

[33] E. J. Strait. Wall stabilization of high beta tokamak discharges in DIII-D. *Phys. Rev. Lett.*, 74(13):2483–2486, 1995.

[34] T. S. Taylor. Wall stabilization of high beta plasmas in DIII-D. *Phys. Plasmas*, 2(6):2390–2396, 1995.

[35] N. G van Kampen. Stochastic processes in physics and chemistry. *Elsevier Science Publishers B.V, Amsterdam*, 1992.

[36] Z. R. Wang, S. C. Guo, L. Shi, T. Bolzonella, M. Baruzzo, and X. G. Wang. Comparison between cylindrical model and experimental observation on the study of resistive wall mode in reversed field pinch plasmas. *Phys. Plasmas*, 17:052501, 2010.

[37] J. A. Wesson. Hydromagnetic stability of Tokamaks. *Nucl. Fusion*, 18(1):87, 1978.

[38] J. A. Wesson. Tokamaks. *Clarendon Press, New York*, 1997.

[39] A. Yoshioka, T. Tatsuno, and M. Wakatani. Stabilization of Resistive Wall Mode due to shear Alfven resonance in a cylindrical plasma with uniform longitudinal flow. *Phys. Soc. of Japan*, 67(11):3794–3800, 1998.